SATELLITE FORMATION FLYING

Development and Implementation of a GNC System

MSc Thesis Report

Diego Hélant Muller

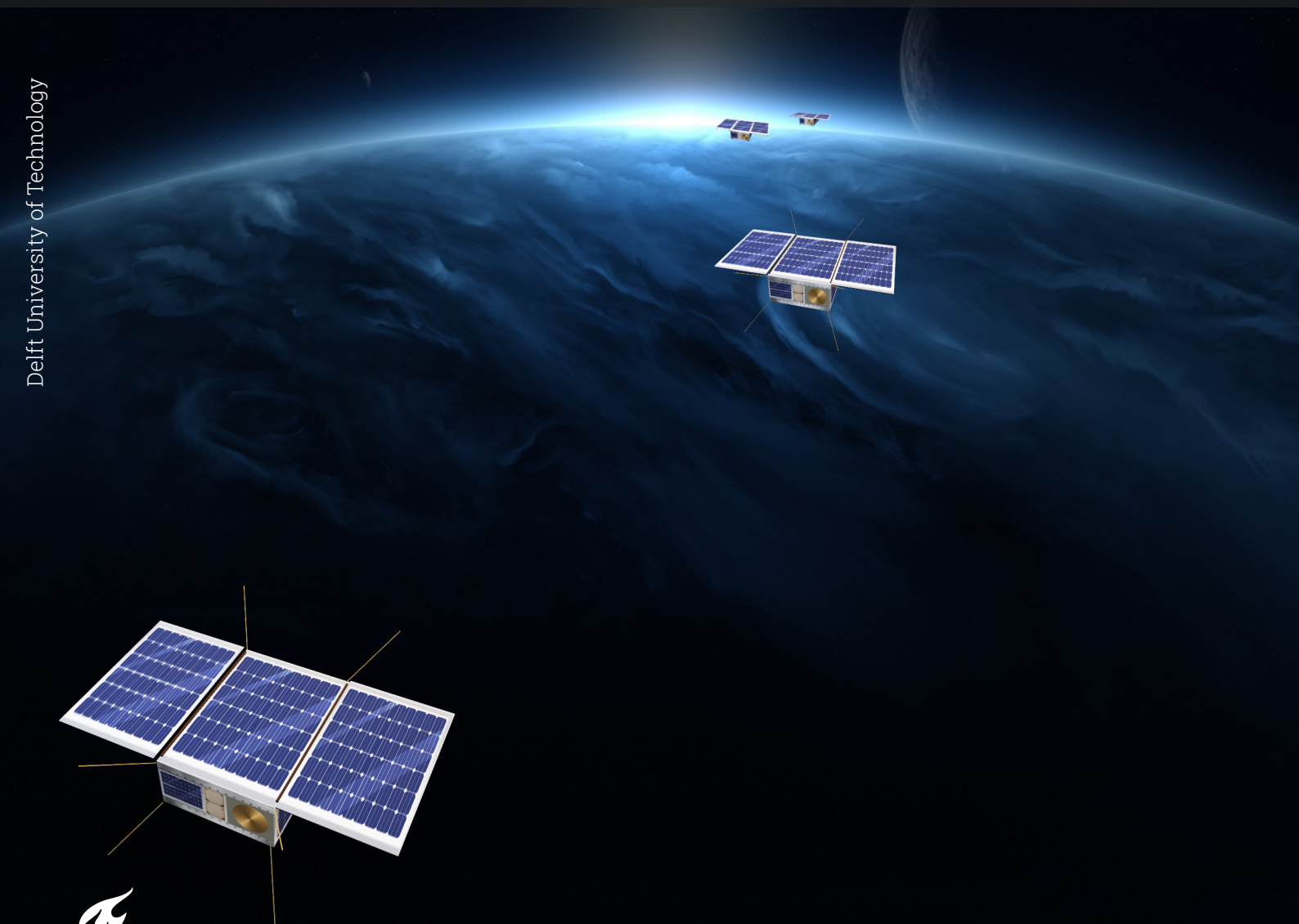

Delft University of Technology

TU Delft

SATELLITE FORMATION FLYING

Development and Implementation of a GNC System

MSc Thesis Report

by

Diego Hélant Muller

Student Name	Student Number
Diego Hélant Muller	4357019

TU Delft Supervisor:	S. Speretta
RNLAF Supervisor:	Major M. Noppen
Project Duration:	January, 2023 - October, 2023
Faculty:	Faculty of Aerospace Engineering, Delft

Cover:	A 6U SmallSat Satellite Formation Consisting of Four Satellites
Style:	TU Delft Report Style

TU Delft

Acknowledgements

This report is written as graduation thesis for the master Space Exploration at Delft University of Technology.

I would like to take this opportunity to thank my thesis supervisors, major ir. M. (Marko) Noppen and ir. S. (Stefano) Speretta for the countless conversations about formation flying. In the end, I have enjoyed the critical and punchy questions from major M. Noppen, leading to new insight in the problem. Additionally, I appreciate the level of involvement from ir. S. Speretta with every step along the thesis, but especially the discussions regarding navigation filter. If there was no time limit for the thesis, we would have been still at the navigation filter, tweaking and analyzing to fully understand every residual.

Furthermore, I want to thank colonel J.B. (Bernard) Buijs for allowing me to continue my research after the internship at the Defence Space Security Center. I am grateful for my time at the RNLAF, which brought me the basics of practical space operations.

Finally, I want to thank my parents for making it financially possible to finish both my bachelor and master at university level, which resulted in the engineering mind I now have.

Diego Hélant Muller
Delft, October 2023

Summary

This thesis report has explored the complex field of satellite formation flying, focusing on Guidance, Navigation and Control (GNC) strategies for maintaining formations of multiple satellites. The research has been guided by a series of research questions aimed at improving the understanding and implementation of GNC systems for satellite formations.

The report begins by providing an overview of the background and context of satellite formation flying, highlighting its significance in modern space missions. It emphasizes the need for precise control systems to maintain formations and addresses the challenges posed by various disturbances and constraints.

To address these challenges, the report presents a detailed methodology for developing an end-to-end GNC system. This methodology involves the use of nonlinear dynamics models, including considerations for Earth's oblateness and drag effects, to describe the motion of satellites within the formation. Additionally, the report explores the use of both absolute and relative dynamics models to enable the control of large satellite formations.

Throughout the report, the performance of the GNC system is analyzed through various simulations and experiments. Different thruster models, including variable and fixed thrusters, are evaluated, shedding light on their effectiveness in maintaining formations. The analysis also considers the impact of energy-matching conditions on reducing the frequency of maneuvers.

The results of the simulations demonstrate the challenges and limitations of the Sliding Mode Controller (SMC) based control system, particularly in the context of real-world thruster implementations. Tracking errors and drift in formations are observed, necessitating further research into mitigating these issues.

In the final chapters, the report explores potential areas for future research and improvements. These include investigating alternative thruster models, optimizing control algorithms, and developing strategies for reducing drift in formations.

In conclusion, this thesis report provides valuable insights into the complexities of satellite formation flying, and the challenges faced by GNC systems. It offers a comprehensive methodology for developing and analyzing these systems and highlights areas for future research. Ultimately, the report contributes to the ongoing advancements in satellite formation flying, paving the way for more precise and efficient space-based operations.

Contents

List of Figures

List of Tables

Acronyms

ADCS Attitude Determination and Control System
ATO Along-track Orbit
BLS Batch Least Squares
CW Clohessy-Wiltshire
ECEF Earth Centered Earth Fixed
ECI Earth Centered Interial
EKF Extended Kalman Filter
EOM Equations of Motion
GCO General Circular Orbit
GMAT General Mission Analysis Tool
GNC Guidance, Navigation and Control
GNSS Global Navigation Satellite System
GPS Global Positioning System
INC Inclination
ITO In-track Orbit
LEO Low Earth Orbit
LQR Linear Quadratic Regulator
LVLH Local Hirzontal Local Vertical Frame
PCO Projected Circular Orbit
RAAN Right Ascension of the Ascending Node
RMSE Root Mean Square Error
RNLAF Royal Netherlands Air Force
ROE Relative Orbital Elements
RSV Reference Satellite Variables
SFF Satellite Formation Flying
SMC Sliding Mode Controller
SRP Solar Radiation Pressure
STM State Transition Matrix
TA True Anomaly
TLE Two Line Element
UKF Uncended Kalman Filter

Nomenclature

Symbols

Symbol	Definition	Unit
$(\cdot)_d$	desired condition	
V	Velocity	[km/s]
v_x, v_y, v_z	Velocity vector components of deputy in LVLH frame centered at Earth	[km/s]
$\dot{x}, \dot{y}, \dot{z}$	Velocity vector components of deputy in LVLH frame centered at the chief	[km/s]
x, y, z	Position vector components of deputy in LVLH frame	[km]
ϕ	Phase angle formation	[deg]
ρ	Relative position vector	[km]
$\dot{\rho}$	Relative velocity vector	[km/s] ...

Constants

Constant	Value	Unit
C_{20}	-0.000484165390	[-]
k_{J_2}	2.633	$[km^5/s^2]$
ω_e	7.292115e-05	$[rad/s]$
R_e	6378.1363	$[km]$
μ	398600.4415	$[km^3/s^2]$
g_0	9.80665e-03	$[km/s^2]$

1

Introduction

Since the early days of the space program, the study of spacecraft formation flying and its associated challenges has been ongoing. Over time, spacecraft formation flying has emerged as a revolutionary technique for conducting space-based operations. This approach involves deploying two or more spacecraft in a predetermined configuration.

One of the key applications of spacecraft formation flying is in Earth observation. It proves particularly valuable when the goal is to observe a specific location on Earth using identical instruments placed at different positions. Global Navigation Satellite System (GNSS), for example, is a well-known application that utilizes multiple satellites to acquire a precise location of a receiver, which would be challenging to obtain with a single satellite.

A group of GNSS satellites forms what is referred to as a constellation. These satellites function collectively to serve a common purpose and are strategically positioned in various orbits to achieve specific surface coverage objectives.

Royal Netherlands Air Force (RNLAF) has expressed a growing interest in the concept of satellite formation flying. This interest has given rise to actual missions that rely on satellites flying in formation. Given the absence of suitable software within the organization, the primary goal has been to develop a tool capable of utilizing GNSS data in conjunction with a navigation system for the purposes of guidance and control. This comprehensive end-to-end system is essential for the maintenance of a formation.

1.1. Research Questions, Tasks, and Scope

In this section, The outline of the primary research hypothesis and its related research questions is presented. Moreover, a clear overview presented of the specific tasks required to address these questions and delineate the research scope.

1.1.1. Research Questions

Hypothesis: By applying nonlinear control to a system of absolute and relative dynamics including Earth's oblateness and atmospheric drag, a fast and fuel-efficient solution can be achieved, allowing for high adaptability.

1. **Problem A:** Which methodology and software are required to enable the development of a complete GNC system suitable for satellite formation flying?
2. **Problem B:** How can the optimal control problem be formulated and solved for formation flying of a reduced formation consisting of a chief and one deputy whilst including the major disturbances such as Earth's oblateness, drag effect and non-linearity?
3. **Problem C:** What is the impact on fuel cost by defining a target formation based on the orbital momentum and energy-matched conditions, instead of using well-known Clohessy-Wiltshire (CW) condition?

4. **Problem D:** How can the optimal control problem be extended to include up to four satellites, and which adaptations are necessary to guarantee safe operations?

1.1.2. Research Tasks

In order to address the research question related to the hypothesis, the following task will be undertaken:

1. Use a navigation filter to achieve precise orbit determination which can be propagated in time. Write the necessary software to enable the conversion from a batch of GNSS data to achieve an accurate orbit estimation.
2. Select and implement the dynamical equations of the simulation environment that fits with the accuracy of the satellite formation flying problem at hand.
3. Use a SMC to formulate and solve the optimal control problem.
4. Construct and assess GNC performances and compare them with mission needs.

1.1.3. Research Scope

In the field of satellite formation flying, numerous efforts have been made to enhance the widely recognized CW equations. These equations are linearized equations of motion and do not account for external disturbances. In an endeavor to refine these equations, some have expanded the force model to incorporate the effects of an oblate Earth. A comparative study, conducted by Wang et al. 2017, highlighted the inaccuracies of linearized equations of motion. It can be deducted from their findings that linear models may not adequately represent the mission scenarios under consideration.

Furthermore, in the extensive domain of formation flying, this discussion will primarily center on the maintenance of nano-satellite formations. The analysis assumes that these satellites do not possess inter-satellite communication capabilities and that the targeted formation size falls within the range of 5 to 30 kilometers. Additionally, it should be noted that the satellites under examination are equipped with thrusters, which introduce specific constraints and considerations.

Regarding propagation schemes, one straightforward method for propagating a multi-satellite formation involves individually propagating each satellite using an absolute nonlinear force model. This approach offers the advantage of simplifying the implementation of a high-fidelity model. However, in most literature, the motion of a deputy (also referred to as a follower) is described using relative dynamics. Expressing the deputy's motion in terms of relative dynamics significantly reduces their force model complexity, as it primarily accounts for differential effects. This approach is especially beneficial in anticipation of future satellites equipped with inter-satellite communication capabilities, as it substantially lowers the computational burden on the deputy. Additionally, employing relative dynamics simplifies the formation flying problem expression, making it more convenient for a controller to generate maneuvers to achieve complex formations. Given these considerations, it was decided to adopt a suitable relative model to describe the deputy's motion.

Given the considerable size of the intended formation (5-30 km), several relative models are not applicable. The most appropriate dynamical model has been introduced by Xu and Wang 2008. Furthermore, an analysis conducted by Wang et al. 2017 demonstrated that this model remains valid even for larger formation sizes exceeding 10 kilometers and for chief orbit eccentricity. While faster models do exist, for the specified formation size, the model by Xu and Wang 2008 proves to be the most suitable option.

The above-mentioned model relies on nonlinear dynamics, necessitating the implementation of a nonlinear controller. The reference mission used in several simulations is a real formation mission, which employs a low-thrust engine. Consequently, the controller must possess the capability to generate low-thrust maneuvers for formation maintenance. This results in an optimal control problem, which can be resolved through extensive optimization, consuming significant computational resources and time. From a mission perspective, the maneuver ideally needs to be computed and scheduled within a single orbit. Additionally, it is imperative that the controller demonstrates robustness, ensuring its ability to consistently generate maneuvers for maintaining the formation. Optimization theory proves to be a valuable tool for analyzing intricate targeting sequences or exploring the controller's design space. Ultimately, the controller should deliver a swift and dependable solution, facilitating a transition towards

autonomous GNC, therefore the SMC is selected.

In summary, a combination of absolute and relative dynamics is employed to characterize the motion of the chief and deputies, respectively. Utilizing nonlinear control with nonlinear dynamics facilitates the maintenance of large formations. The forthcoming section will delve into the methodology used to develop these GNC systems.

1.2. Research Methodology

The aim of this section is to provide a comprehensive overview of the methodology employed throughout the thesis. Building upon the previously mentioned hypothesis, software is developed to facilitate the analysis of the selected SMC with nonlinear dynamics. However, before the controller's performance can be assessed, various tools must be developed to reach this stage. This section outlines the methodology used to bridge the gap from the real-world problem to the execution of an actual satellite maneuver.

To enhance comprehension of the workflow, a graphical representation of the software methodology has been created and is presented in Figure 1.1. This illustration delineates the process, beginning with data acquisition and culminating in the calculation and transmission of maneuvers.

The software initiates by utilizing Global Positioning System (GPS) data and employing a Extended Kalman Filter (EKF) for measurement fitting. Following the filtering of measurements, the resulting state estimate is used to propagate the satellites for 1-3 orbits, accounting for the time required to generate a maneuver while considering contact times of a single ground station. This propagation employs a high-fidelity model to ensure optimal controller input accuracy. Furthermore, the propagation outcome serves as input for the dynamical model, guidance system, and SMC.

In Figure 1.1, these processes are color-coded to denote their dependencies and relationships. The guidance solution is configured to generate guidance trajectories based on the desired formation type. For formations derived using linear models, the guidance solution employs linear dynamics, while nonlinear dynamics are utilized for energy-matched formations. Further details regarding the setup of the guidance solution can be found in section 3.3.

Ultimately, the software yields suggested maneuvers that can be simulated to assess their validity. This architecture enables maneuver analysis before uploading to the ground station. Once accepted, the final maneuvering sequence is transmitted to the designated satellite.

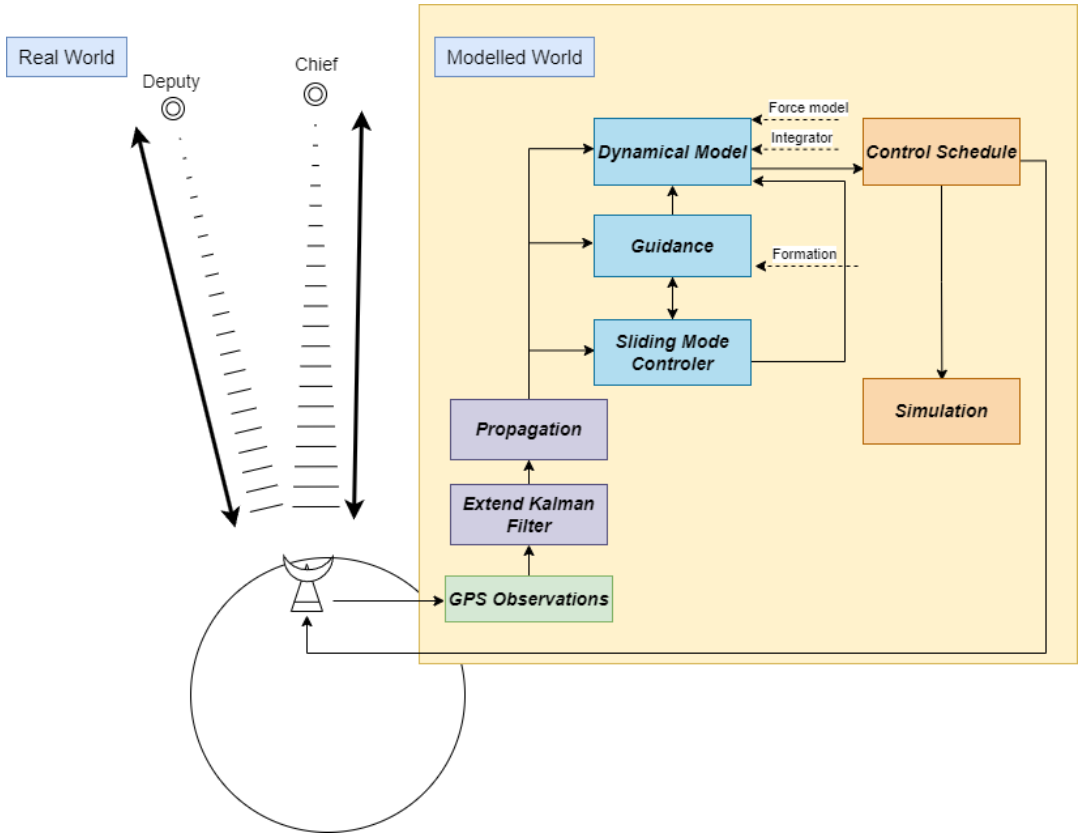

Figure 1.1: This figure shows the overall set-up of the SFF software, illustrating the transition between the real world to the SFF software.

1.3. Expected Contribution

The research discussed in this thesis contains four main contributions.

Development of a Navigation Solution Utilizing an EKF with Authentic GPS Data. As part of the endeavor to complete the operational sequence, raw GPS measurements are processed using custom filter settings within General Mission Analysis Tool (GMAT) platform. This implementation provides essential insights into the attainable accuracy of the initial state for formation flying. It is worth noting that such a navigation system was absent from the toolkit available to the RNLAF and has therefore been developed as a crucial component within this thesis.

Modification of the SMC Incorporating a Realistic Low-Thrust Engine. The SMC implementation examined in the research conducted by Liu and Hexi 2006 employed simulated controlled disturbances to accommodate disturbances. The principal aim of this research was to demonstrate the validity and applicability of utilizing low-thrust propulsion for formation flying. This was accomplished through the utilization of an engine capable of thrusting in three dimensions and adjusting its thrust within the range of 0 to 1 m/s^2. In the scope of this research, the performance and constraints of a real thruster were incorporated. Constraining the engine's freedom poses challenges to the convergence behavior of the controller.

Modification of the SMC Incorporating a Nonlinear Dynamics Model Accounting for J_2 and Drag. The research conducted by Liu and Hexi 2006 showcased the controller's capabilities in a nonlinear environment. To enhance the real-world accuracy of the numerical model, significant disturbances such as J_2 and drag needed to be considered. Consequently, the SMC was equipped with an alternative dynamical model to enhance its fidelity.

Implementation of Diverse Multi-Satellite Guidance Strategies to Demonstrate Software Adaptability for Various Formations. The software incorporates a formation design toolbox, enabling cus-

tomized multi-satellite formation design. The impact of different guidance strategies on fuel consumption is thoroughly examined.

1.4. Document Preview

In Chapter 2, the intricacies of formation flying are explored, commencing with an examination of various formation types. Subsequently, existing knowledge in the field is reviewed to assess its relevance to the selected reference mission. The insights gleaned from the literature are integrated to develop the Satellite Formation Flying (SFF) software, with the methodology detailed in Chapter 3.

Shifting focus to address the research questions derived from the inquiry, the outcomes of the navigation system are presented in Chapter 4. Chapter 5 conducts multiple simulations to evaluate the controller's performance within real mission scenarios. Additionally, an optimal guidance solution is implemented and scrutinized in Chapter 6.

Advancing further, Chapter 7 expands the simulations to contain a constellation of four satellites. The code is validated, and the verification results are presented in Chapter 8.

Finally, Chapter 9 marks the conclusion of the research journey. Here, answers to the research questions are provided, along with insights and directions for future work.

2

Background

In this chapter, we delve into the intricacies of formation flying dynamics and control strategies. To lay the foundation for our exploration of formation flying dynamics and associated models, the chapter begins by providing a comprehensive understanding of what formation flying entails. This involves defining formation flying, introducing the coordinate system used to define relative dynamics, and highlighting the most common formation types while shedding light on their key characteristics. Next, the control laws employed for formation flying are introduced, featuring a selection of promising controllers. Finally, the primary dynamical model and associated controller utilized throughout the majority of the thesis are presented.

2.1. Satellite Formations

Before delving into the dynamics of formation flying and associated models, this section begins by providing a definition of formation flying. It then introduces the coordinate system used to define relative dynamics. Finally, it highlights the most common formation types and presents their key characteristics.

2.1.1. Definition

Satellite formation flying encompasses the synchronized and regulated coordination of multiple spacecraft, ensuring they uphold distinct relative positions and orientations in space while jointly executing shared missions or tasks. This cooperative setup entails the meticulous preservation of accurate spatial relationships between individual satellites, often with the goal of attaining amplified observational capabilities, expanded coverage area, refined data collection, and other mission objectives that pose challenges when pursued by a single satellite. Formation flying can manifest as the organized alignment of satellites in diverse configurations, including constellations, clusters, or alternate arrangements. Achieving the intended formation mandates the implementation of sophisticated control strategies, effectively managing the intricacies of orbital dynamics and external disturbances.

2.1.2. Local Frame

Starting from the ECI J2000 reference frame, a conversion of the coordinate system can be executed to facilitate the advancement of relative dynamics. This transformation yields what is known as Hill's frame, illustrated in Figure 2.1. Hill's frame, also referred to as Local Hirzontal Local Vertical Frame (LVLH), originates at the center of mass of the chief satellite. In this frame, the x-axis aligns with the chief's radial direction, while the z-axis aligns with the orbital angular momentum vector. Completing the right-hand reference frame, the y-axis is established. Hill's frame finds primary application within the domain of relative dynamical models.

The state elements used to describe the chief's orbit can also be obtained in Figure 2.1. The chief's orbit uses Reference Satellite Variables (RSV) containing a set of six state elements from which the chief's orbit can be fully defined. The RSV representation has been derived by Xu and Wang 2008 and consist of $r, \dot{r}, h, \Omega, i, \theta$. These elements are used to describe the chief's orbit and can be depicted

in Figure 2.1. The radial position and velocity are represented by r and $\dot{r}$, and h is the magnitude of the orbital momentum vector. Next, Ω is the Right Ascension of the Ascending Node (RAAN), i the inclination, and θ is the true latitude. The benefit of using the true latitude (θ) is that it can be used for circular orbit, in contrast with the true anomaly (ν). Moreover, for very low eccentricity, the true anomaly is ill-defined, Vallado 2013. The true latitude is defined by:

$$\theta = \omega + \nu \tag{2.1}$$

where ω and ν represent the argument of periapsis and true anomaly, respectively.

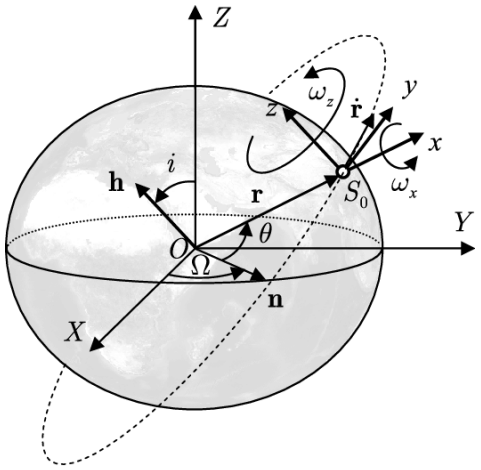

Figure 2.1: LVLH (Hill's) frame expressed in ECI reference system, Wu et al. 2016.

2.1.3. Formation Configurations

The objective of this section is to provide a foundation and visual representation of relative motion within formation flying. This involves discerning various formation types and their attributes. Due to the constraints of orbital mechanics, practically only four types of formation orbits can be considered. A pivotal aspect of formation flying is synchronizing the orbital period with that of the chief satellite. Additionally, the initial conditions of both the deputy and chief satellite significantly impact the relative motion of the formation. The four formation types are differentiated by Relative Orbital Elements (ROE). For enhanced visualization of the various formation flying types, Figure 2.2 illustrates the corresponding differential orbital elements and crucial characteristics. In this representation, the x, y, and z coordinates denote the position coordinates within Hill's orbital frame. It is important to note that the depicted trajectories in Figure 2.2 are generated under the assumption of an unperturbed spherical Earth.

Each of the formation types will now be elaborated upon, commencing with the Along-track Orbit (ATO) formation. This approach is generally regarded as a straightforward method for achieving substantial (200 km) to moderate (5 km) satellite separation. In the ATO formation, the orbital plane is aligned, and only a discrepancy in the true latitude (θ) is introduced. This is why ATO formations are sometimes referred to as in-plane formations within the literature. Figure 2.2 provides insight into the key characteristics of this formation type. A notable advantage of the ATO formation lies in its suitability for large formations, with a design that facilitates uncomplicated maneuvering for formation maintenance.

The In-track Orbit (ITO) formation allows satellites to traverse the same ground track. However, due to Earth's rotation, the satellites' orbital planes exhibit slight disparities. Achieving the necessary offset for an ITO formation entails adjustments to both the argument of latitude (θ) and the right ascension of the ascending node (Ω). Although ITO formations enable interval point observations, their practical application in real space missions remains limited.

The remaining two formation types, the General Circular Orbit (GCO) and Projected Circular Orbit (PCO), share a common advantage. Both ATO and ITO formations are susceptible to substantial satellite drift over time. While the satellite state and required control efforts closely align with the real solution, the inherent model simplifications preclude achieving a zero-error solution. A substantial

portion of this drift, stemming from these inaccuracies, can be understood by examining the linearized model developed by Clohessy and Wiltshire 1960, which will be detailed in Chapter 3. By manipulating the solutions derived from this model, a condition can be identified that mitigates the aforementioned linear drift. This condition is tied to an optimal formation geometry, which effectively minimizes that drift. Here, the term ”minimization” is used because while linear models cancels drift, nonlinear effects and perturbations can still induce minor satellite drift. Implementing this geometry constraint gives rise to the GCO and PCO formations. A GCO formation can be visualized as a formation constrained by a fixed radius. Next, the PCO formation is constructed in a similar way to the GCO, but here the plane is rotated so that the projected relative trajectory represents a circle with a constant radius. Although these formations offer improved stability over the long term, their implementation demands a more precise attitude and thruster control. These formations are typically chosen for small (100 m) to moderate (5 km) satellite separation. In specific Earth observation missions, a circular projected ground track proves to be advantageous. Achieving this requires meticulous geometry condition selection, resulting in the PCO formation. Crucial characteristics of the GCO and PCO formations are outlined in Figure 2.2.

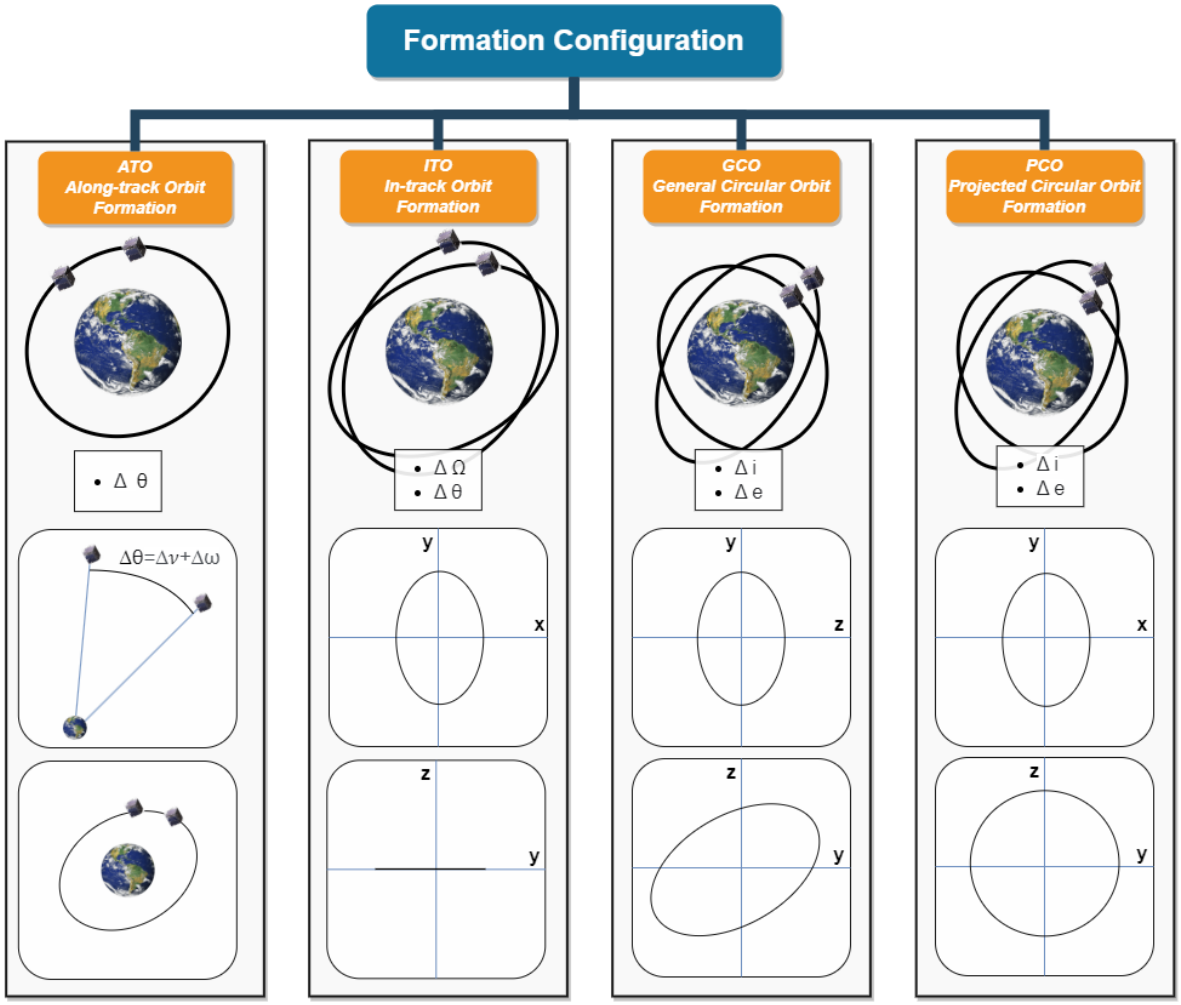

Figure 2.2: Formation flying configuration types.

2.2. Relative Dynamics

This assessment provides a comprehensive exploration of diverse implementations documented in literature, highlighting the unique advantages inherent in each model. Nonlinear models offer a distinct advantage in their increased accuracy when applied to expansive formations and extended-duration simulations. Nevertheless, using nonlinear equations into controllers poses challenges compared to the more straightforward integration of linear models.

Kechichian 1998 formulated a nonlinear model encompassing both the J_2 effect and atmospheric drag, rendering it applicable to circular and elliptical orbits, . Nonetheless, a notable drawback of this implementation lies in the intricate nature of its equations, which omit certain components of the J_2 effect. Identifying this limitation, Xu and Wang 2008 embarked on crafting their own nonlinear model. Leveraging the principles of Newtonian mechanics, they streamlined Kechichian's equations without sacrificing accuracy, yet chose to exclude the influence of differential drag.

While the Xu and Wang model proved accurate and versatile for a multitude of formations, there was room for refinement through the incorporation of differential drag. Building upon this foundation, Morgan and Chung 2012 expanded the Xu and Wang model, enhancing its precision for Low Earth Orbit (LEO) formations due to increased atmospheric disturbances. Wu et al. 2016 further delved into the nonlinear solution techniques for the described in Morgan and Chung 2012. Their study introduced the practical implementation of nonlinear optimization for both low and high thrust propulsion systems. The resultant control strategy and optimization approach demonstrated success, establishing a viable nonlinear method for general use cases. However, the computationally intensive nature of obtaining solutions relegated this model from being considered for autonomous on-board navigation.

In the absence of comprehensive insights into the implementation details, making an optimal choice among dynamical models can prove to be a challenging endeavor. The precision of the model is fundamentally intertwined with factors such as formation size, eccentricity, and orbital altitude. Given the specific focus of this review on LEO formations, the examination narrows down to the influence of formation size and eccentricity. Through simulations conducted by Wang et al. 2017, discernible disparities in model accuracy emerge, contingent on diverse formation characteristics.

Illustrating this, the impact of formation size on model accuracy is visually represented in Figure 2.3. Within the framework presented by Wang et al. 2017, the model error index (σ) serves as an indicator of the model's deviation from the true solution. This index, which is directly proportional to the model error, is appropriately referred to as the model error for simplicity. A noteworthy observation is that augmenting formation size proportionately affects the accuracy of linear models as opposed to nonlinear counterparts. This particular simulation assumes a nearly negligible eccentricity, elucidating the proximity of error between the CW and TH models.

Figure 2.3 further reveals another facet, which is the role of Earth's oblateness. Notably, the model introduced by Xu and Wang 2008 exhibits a reduction in error compared to the unperturbed nonlinear model, attributed to the incorporation of the J_2 effect. This incorporation stands as the underlying reason for the error reduction. Lastly, it becomes evident from the data presented in Figure 2.3 that the influence of J_2 looms larger than the impact of nonlinearity.

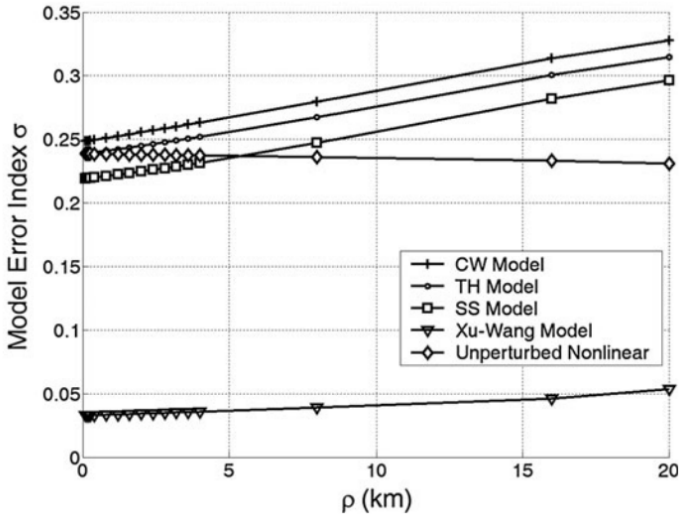

Figure 2.3: Model error versus formation size for linear and nonlinear models, Wang et al. 2017.

Another factor wielding influence over the model's precision is eccentricity. The majority of linear models are formulated under the premise of a circular reference orbit, making it foreseeable that errors would escalate with increased eccentricity. In Figure 2.4 a simulation performed by Wang et al. 2017, the impacts of eccentricity across various dynamical models is depicted. Certainly, the consequences of omitting eccentricity (as evident in the CW and SS models) within their framework are readily apparent.

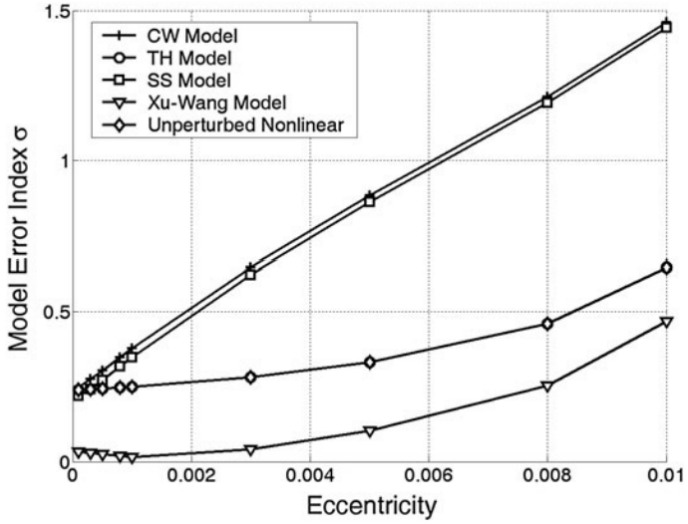

Figure 2.4: Model error versus chief eccentricity for linear and nonlinear models, Wang et al. 2017.

Given that these simulations are conducted within a narrow radius (0.1 km), the solutions of the TH model and the unperturbed nonlinear model align closely. For both nonlinear models, the influence of heightened eccentricity becomes apparent, emphasizing why eccentricity holds paramount significance in satellite formation design. The investigation performed by Wang et al. 2017 has delineated that eccentricity, J_2 perturbation, nonlinearity, and atmospheric drag each imprint distinct trajectories upon model error.

For satellite formations orbiting below 300 km, the prevailing forces are primarily attributed to atmospheric drag. However, beyond the threshold of 400 km, eccentricity takes the reins in governing model error, followed by the consequential J_2 effect and subsequently, nonlinear effects.

Presently, formation control predominantly relies on linear dynamical models, prized for their tractability, often yielding solutions in closed-form. Nonetheless, the trade-off lies in their inherent precision limitations. The usefulness of linearization diminishes in long-term forecasts (covering several days) and significant spacecraft separations (exceeding 10 km). When dealing with proximity formations (ranging from 1 m to 1 km), real-time, frequent (daily to weekly) control becomes indispensable for safety and formation upkeep. Linear models hold the advantage of providing robust and real-time control. Yet, the flip side is their inability to provide optimal solutions or accurate long-term predictions—a trade-off inherent in deploying linear dynamics. In cases where ground-based maneuver generation drives the mission, nonlinear dynamics come to the fore.

The preceding sections have outlined a collection of relative linear dynamical models, subject to scrutiny and analysis. This segment will briefly underscore challenges and assumptions underpinning these promising models. The fidelity of the control system hinges on the dynamics employed, leading to instances where certain linear models might facilitate easy control implementation but produce less accurate outcomes.

Beginning with the CW equations, their user-friendliness fostered their application in early rendezvous and docking scenarios. This model efficiently accommodates autonomous short-term control, particularly when referencing a satellite in a circular orbit, exhibiting robustness. However, without adaptations accounting for the J_2 effect, the CW equations lack the precision necessary for formation flying. Subsequent efforts to enhance these equations through J_2 and differential drag integrations, while

commendable, limited their applicability solely to circular orbits. By finally adapting these equations to encompass eccentric orbits, a marked improvement over the original CW formulation was achieved. However, linearization poses limitations on all these models, making them inappropriate for large satellite separations. This challenge is also applicable to linearized State Transition Matrix (STM) models.

A distinctive approach, as demonstrated by Koenig et al. 2017, addresses the pitfalls of linearization while incorporating J_2 and atmospheric drag effects. To sidestep any confusion, the Koenig model employs ROE, mitigating linearization inaccuracies in the deputy state. Among the array of linearized models, the Koenig model stands out in terms of accuracy, albeit at the expense of increased implementation complexity.

2.3. Optimal Control and Solution Finding

This section will focus on implementing the majority of the controllers used in orbital mechanics. However, the scope is now slightly constrained, with a shift in focus towards control strategies in the realm of formation management. It is important to note that innovative research endeavors aimed at refining techniques for libration point formation flying are not encompassed within this discussion. Furthermore, a pronounced emphasis will be placed on exploring novel control methodologies.

Before delving into novel control approaches, it is prudent to contemplate and assess both the potential benefits and drawbacks associated with Linear Quadratic Regulator (LQR) controllers. From the researching the LQR control, it becomes evident that this particular control method is exclusively suited for integration with linear dynamical systems. Numerous instances have emphasized the effectiveness of LQR controllers in managing formation flying and enabling rendezvous and docking maneuvers.

Jin and Lifu 2011 devoted an entire study to the implementation of LQR control for formation flying, a testament to the enduring relevance of this methodology. It is undeniable that LQR-based control ensures precision and robustness in outcomes. Further exploration has extended into the realm of formation flying without recourse to radial thrust maneuvers to conserve propellant. The applicability of LQR in scenarios avoiding of radial thrust has been dissected in subsequent articles: Starin et al. 2001b Starin et al. 2001a Chao and Bernstein 1994. Nonetheless, it is important to note that this method is constrained to handling linear systems exclusively. While this limitation poses minimal hindrance for close-range operations and compact formations necessitating frequent maneuvers, applying linear dynamics over greater separation distances incurs significant additional fuel consumption due to model inaccuracies. This rationale underscores the subsequent direction of control algorithms, which will pivot towards the optimization of nonlinear systems.

The SMC has undergone thorough analysis across various contexts, particularly within Earth-based applications. Liu and Hexi 2006 undertook a comprehensive investigation into the potential of SMC for formation flying, revealing substantial promise. Their methodology is centered around controlling the output to steer a deputy satellite onto a reference trajectory. This reference trajectory is established in relation to the chief satellite and can be arbitrarily chosen. While SMC controllers have not yet been realized for formation control, a review of existing literature lends support to the notion that the process of solution identification is both robust and accurate.

Another avenue for formation control has been pioneered by Wu et al. 2016, focusing on real-time optimal control applicable to both linear and nonlinear models. The incorporation of J_2 perturbations within the linearized models offers a valid strategy for short-term control of small formations. To enhance model accuracy, the use of nonlinear equations of motion developed by Morgan and Chung 2012 is advisable. This approach pivots towards minimizing fuel consumption through the utilization of Legendre Pseudospectral Methods (LPM). Beyond fuel optimization, this method is characterized by efficiency and swiftness, attributed to the integration of Legendre Gauss Lobatto (LGL) points. The accuracy of the algorithm is significantly influenced by the density of LGL points, with an increase in points leading to enhanced precision. However, augmenting the number of points escalates computational demands. While the use of the Legendre Pseudospectral Method stands as a viable candidate for addressing the optimal control problem within formation contexts, it's important to acknowledge that solving LPMs entails complexity and may necessitate supplementary software.

Huang et al. 2012 delved into the application of a Particle Swarm Optimization (PSO)-based controller

for deep space formation flying with low-thrust maneuvers. Their research outcomes showcased the potential for generating energy-optimal trajectories. PSO's strength lies in its rapid solution generation capabilities and its ability to employ numerical integration to tackle nonlinear systems. It's noteworthy, however, that Huang et al.'s methodology did not incorporate collision avoidance strategies. An enhanced iteration of their model emerged by Huang and Zhuang 2015, wherein inter-swarm communication was utilized to introduce collision avoidance measures. While Huang and Zhuang 2015. centered their efforts on deep space formations, the work done by M. Pontani 2010 explored PSO's utility for LEO formation flying. Reid et al. 2013 applied PSO for rendezvous and close operations, employing a Hamiltonian approach. While the original methodology may be intricate, incorporation of the initial and final states into the model can streamline implementation.

From the literature study, it is concluded that in order to build an adaptable and accuracy dynamical model, the equations presented by Xu and Wang 2008 are the best candidate. As a result of using relative dynamics, the control logic for more complex formation become easier. Moreover, to enhance the model's capability to represent the real world, the added drag implementation by Morgan and Chung 2012 is used. The research presented by Liu and Hexi 2006 demonstrated that the real-time implementation of using a sliding mode controller was deemed successful. The control was able to guidance a satellite using low-thrust in a controlled disturbed environment. The focus of the next chapter is the methodology and implementation of this model and controller.

Based on the literature study, it is concluded that the equations proposed in Xu and Wang 2008 are the most suitable for constructing an adaptable and accurate dynamical model. Utilizing relative dynamics, this choice simplifies the control logic for more complex formations. Additionally, to improve the model's representation of real-world conditions, the drag implementation by Morgan and Chung 2012 is incorporated. The research by Liu and Hexi 2006 demonstrated the successful real-time implementation of a sliding mode controller for guiding a satellite using low-thrust in a controlled disturbed environment.

3

Methodology

In this chapter, we delve into the methodology used to set up the SFF software. The objective of this chapter is to present the chosen models and dynamics to translate the real world problem to the numerical problem, offering a comprehensive understanding of its relevance within the broader scope of the thesis. The developed software consist of two separate modules, the first module is the navigation system which is responsible for generating the state estimate of the satellites. This state estimate is then used in the guidance and control module to observe the satellite formation and come up with the required maneuvers. After presenting the methodology for the navigation system, the second module is extensively described, including the set-up of the guidance system and associate dynamical models. By the end of this chapter, the methodology of the navigation, guidance, and control systems should be clear.

3.1. Software Architecture

The construction of the SFF software involves various processes and subsystems, as illustrated in Figure 3.1. This overview will provide insights into the upcoming methodology.

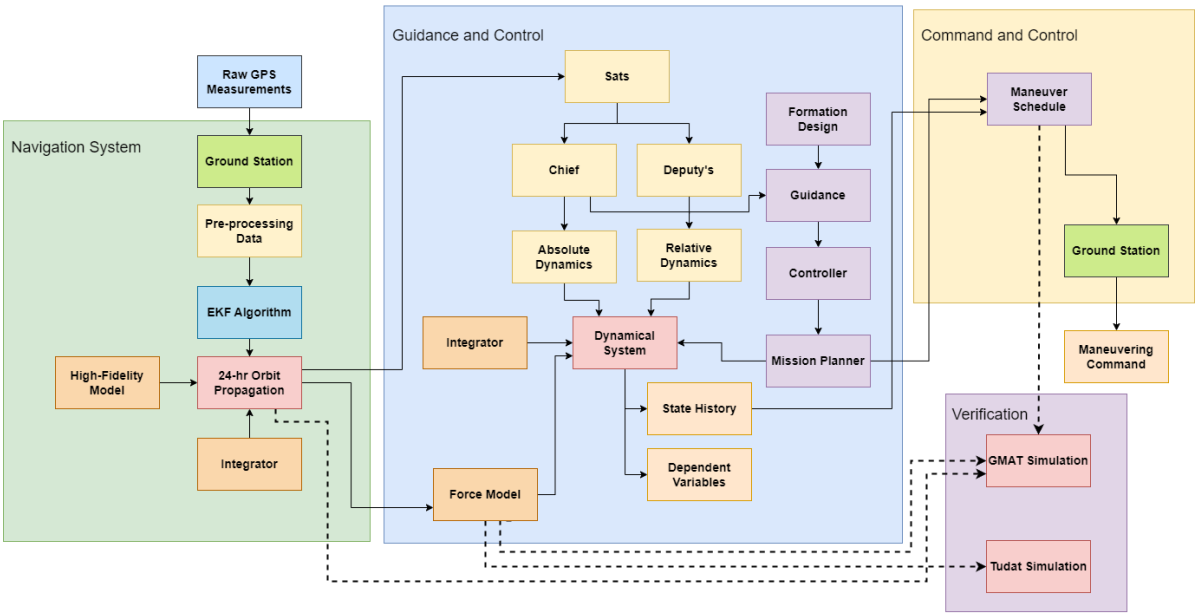

Figure 3.1: Overview of the general code architecture, including the interaction between the GNC system, and command and control.

The navigation system operates as a distinct entity, utilizing GPS measurements for precise orbit determination. The current navigation system implementation encompasses satellite propagation until the point of maneuver uploading. While it may be optimized to reduce turnaround time, it is expected to remain within the range of 1-3 orbits. The resultant position estimate is then transmitted to the guidance and control system, responsible for determining the need for maneuvers and generating them accordingly. Finally, the command and control system is tasked with the conversion of prescribed maneuvers into actual commands that can be received by the satellites.

A dedicated chapter is allocated for software verification, as indicated in Figure 3.1. The verification phase necessitates data from all three subsystems. For further details on individual test cases and verification processes, please refer to Chapter 8.

3.2. Navigation

In this section, the methodology of the navigation solutions will be explained. To carry out precise orbit estimation, an EKF is employed, enabling the estimation of position and velocity at each measurement epoch. Emphasizing the utmost significance is the accuracy of the final state estimate, as it serves as the primary input for the high-fidelity orbit propagator. The task of the navigation filter is disjoint from the guidance and control and uses a different propagator.

Reaching the final state estimate involves a sequence of actions, including several coordinate transformations. An outline of these steps is illustrated in Figure 3.2 for reference. Initially, a Python tool is employed to convert raw GPS data into the necessary GMAT Measurement Data format. Subsequently, the GMD file is linked to a GMAT tracking file set. Once the estimator is executed, both residuals and the final state estimate are extracted. Lastly, the final state is propagated to attain a precise state estimate upon activation of guidance and control.

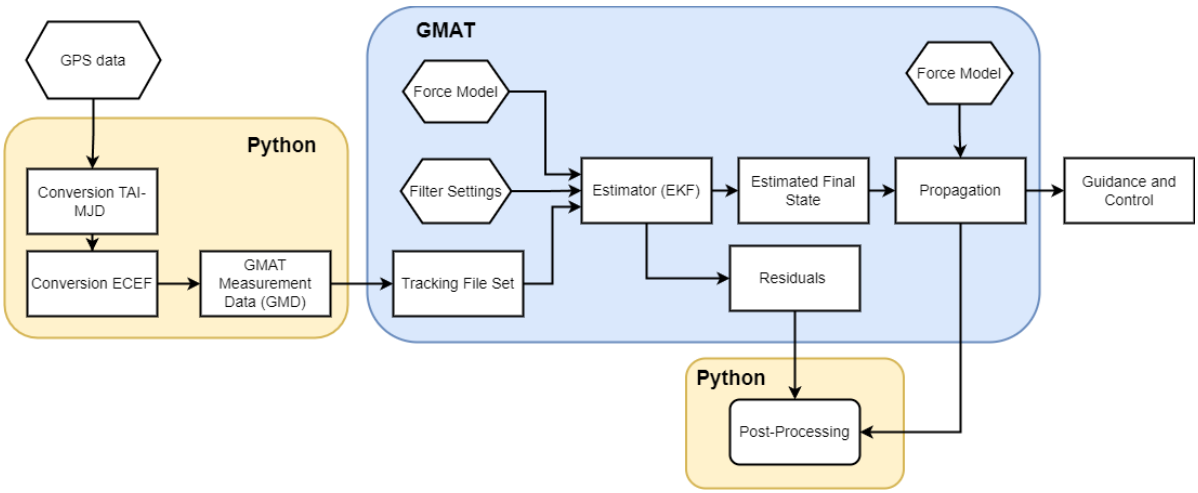

Figure 3.2: Overview set up of navigation system, including the pre- and post-processing steps.

GMAT Navigation Solution The standard implementation of the EKF in GMAT is used for orbit determination (OD). The choice for using GMAT is based on the proven accuracy and possibility to use a high-fidelity model, The GMAT Development Team 2022. Furthermore, the filter's configuration enables the simulation of a satellite GPS receiver, facilitating in-depth analysis of the algorithm's performance. Finally, real GPS data is used to perform orbit determination and analyze the accuracy of the filter. Moreover, adopting a UKF (Unscented Kalman Filter) enhances the solution's accuracy, a finding supported by Alfriend et al. 2010. In their simulation, the position error was assessed using both an EKF and Uncended Kalman Filter (UKF) for a 10 km baseline formation. The results revealed a position accuracy improvement of 0.005 meters after just 1 minute of integration. This enhanced accuracy continues to improve over time, making the UKF a promising choice for the navigation system. However, it is important to note that the development of such a filter, when coupled with a high-fidelity model, was considered an extensive undertaking and was not pursued further.

In order to use the estimator algorithm from GMAT, several tasks must be completed. First, the GPS data should be converted to the right format. GMAT uses a set of tracking file as an input to the filter. Tracking file consist of a timestamp in TAI-MJD (International Atomic Time-Modified Julian Data) and the position expressing in Earth Centered Earth Fixed (ECEF). It is important to know that the conversion from JD (Julian Data) to MJD in GMAT is different from the standard conversion, The GMAT Development Team 2022. Before sampling the data in the filter, the GPS data is pre-processed to fit the standards used by GMAT. This included time and coordinates transformations.

Force Model The EKF's performance hinges on various parameters, and in this section, the most critical ones will be discussed. Whilst the EKF filter provides an update of the solution, the nominal trajectory is propagated. The force model used for the propagation plays a major role on the outcome of the orbit determination. The nominal model implemented for the navigation filter is:

- Integrator: PD78 with fixed step size of 10 seconds.
- Earth: Spherical harmonics up to degree and order 64, from the JGM-2 gravity model.
- Drag: MSISE90 for a general spherical object.
- Space Weather: SRP (Solar Radiation Pressure), using latest space weather data.
- Third body: Sun, Moon
- Solid and Ocean Tides

The estimation and subsequent propagation of the navigation solution will be executed employing the aforementioned force model. A significant portion of computational resources is devoted to evaluating the gravity model. This selection is underpinned by empirical data from the International Space Station (ISS) and Japan Earth Resources Satellite (JERS-1) taken from Vallado 2010. In the analysis performed by Vallado 2010, the objective was to provide a clear depiction of the implications associated with the utilization of different force models. It is important to note that although both the ISS and JERS-1 are larger and heavier than the SmallSat under investigation, this comparative analysis yields valuable insights and guides several decision-making processes. The data acquired from the JERS-1 spacecraft indisputably demonstrates the imperative need for a high-fidelity model to achieve a precise navigation solution and subsequent propagation. The primary aim of this propagation endeavor is to provide a solution with an accuracy margin of merely 10 meters after approximately 3 to 4 orbits. In pursuit of this level of precision, the insights gleaned from Vallado's data make it abundantly clear that the force model described earlier is an essential prerequisite. With this model in place, it is anticipated that the limiting factors will likely revolve around drag modeling and the accuracy of GPS measurements, Reid et al. 2013.

In addition to the previous analysis, a custom simulation was conducted to assess the selection of the force model. This simulation aimed to provide insights into how the chosen model influences the propagated position of the nanosatellite. The simulation was configured using the satellite and orbit data detailed in Chapter 5. For this analysis, only the primary disturbances were considered, encompassing various third-body influences, Solar Radiation Pressure (SRP), drag, and gravity. The results of the 24-hour propagation are presented in Figure 3.3 and Figure 3.4. To gauge the effect of excluding a disturbance, a benchmark was employed for comparison. The benchmark solution comprised the complete model, encompassing all third-body accelerations, drag, SRP, and a gravity model with a degree and order of 100. From Figure 3.3, it can be seen that the accelerations from Jupiter and Venus are of such a low scale, which leads to their exclusion. Next, no SRP acceleration was activated for the nanosatellite and its effect on the final position with respect to the benchmark was zero. However, GMAT simulation showed that the SRP can influence the position in the order of the meter level after a day. Therefore, it is included in the model. In Figure 3.3, the influence of the Sun and Moon result to a meter-level difference and are thus taken into the model. As expected, for a 24-hour long propagated, the effect of the atmosphere can not be neglected. From Figure 3.3, it is evident that the accelerations from Jupiter and Venus are negligible, justifying their exclusion from the model. Additionally, the activation of SRP acceleration had no discernible effect on the final position compared to the benchmark. However, GMAT simulations demonstrated that SRP can influence the position at the meter level after a day, hence it is included in the model. In Figure 3.3, the influence of the Sun and Moon is seen to result in a meter-level difference and is thus retained in the model. As anticipated, for a 24-hour

propagation, the influence of the atmosphere cannot be neglected. Finally, the results presented in Figure 3.4 illustrate that the degree and order of the gravity field significantly impact model fidelity. The incremental accuracy gained by transitioning from J64 to J100 is less than a meter. Given that GPS measurements are accurate at scales above the meter, pursuing a higher order than J64 is deemed unnecessary. For more details regarding the integrator settings, please read section 8.1.

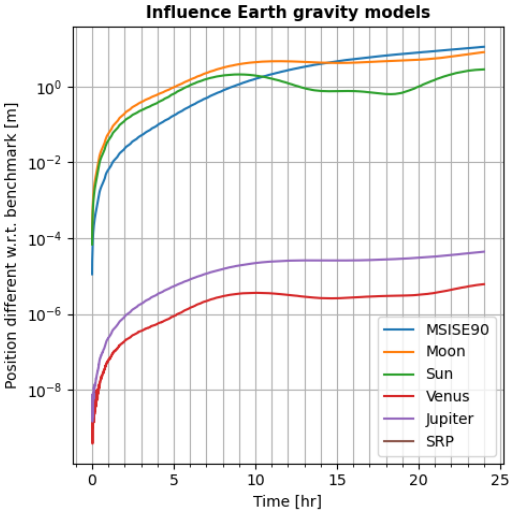

Figure 3.3: The position difference as consequence of selecting different models, namely drag, third body acceleration, SRP.

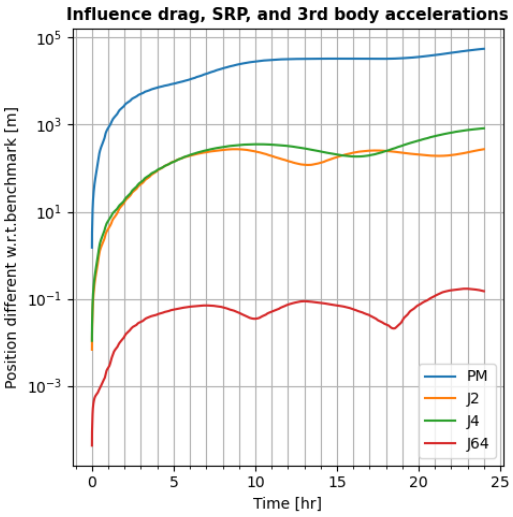

Figure 3.4: The position difference as consequence of selecting different models, namely gravity model.

GPS standard deviation In addition, the EKF uses Kalman noise to avoid filter saturation. The standard value for the filter noise used for the simulation is 10^{-9}. The accuracy and sensitivity of number will be investigated in Chapter 4. Next, the expected standard deviation of GPS (σ_{gps}) has been used to discard invalid or unrealistic measurement. To closely matched the possible accuracy of the sensor, a nominal value of 10 meter is used. Since raw GPS data will be used in Chapter 4, the σ_{gps} avoids use of bad GPS measurement in the filter.

Measurement Noise The initial orbit error covariance is set to be $[4.0 \cdot 10^{-5}, 1.7 \cdot 10^{-5}, 1.9 \cdot 10^{-5}, 5.7 \cdot 10^{-7}, 2.4 \cdot 10^{-7}, 2.6 \cdot 10^{-7}]$, which is calculated using data from the BRIK2 satellite. After the measurement update, the estimation error covariance consistently diminishes compared to its pre-update state. Regardless of the quality of the observation, the inclusion of any measurement consistently decreases the orbit error covariance. Conversely, introducing process noise perpetually elevates the state uncertainty. Hence, achieving a balance is crucial: integrating a measurement reduces state uncertainty, while process noise amplifies it. The convergence of the filter and its long-term performance are inherently tied to maintaining this equilibrium. It is important to note that if measurement or process noise values are excessively low, the orbit error covariance could become overly minimized, leading to the potential rejection of valuable measurements by the filter.

3.3. Guidance Formulation

In the context of formation flying, guidance serves as a crucial element in ensuring the stability and effectiveness of maneuvers. This chapter delves deep into the diverse range of guidance strategies employed within formation flying. The primary objective of this section is to elucidate the distinctions between these guidance solutions and emphasize the pivotal assumptions that underlie their functionality. By the conclusion of this chapter, readers will have a clear understanding of the appropriate scenarios for each guidance solution and the advantages they offer in achieving mission objectives.

3.3.1. Clohessy Wiltshire Condition

In this section, the historical CW equations are presented and discussed, since they will be the foundation of several guidance strategies. The main goal of this section is to demonstrate the application of the CW equations as a form of guidance. The CW equations are given by:

$$\ddot{x} = 3n^2 x + 2n\dot{y} \tag{3.1}$$

$$\ddot{y} = -2n\dot{x} \tag{3.2}$$

$$\ddot{z} = -n^2 z \tag{3.3}$$

In this coordinate system, the x-axis aligns with the radius vector of the target spacecraft, the z-axis aligns with the angular momentum vector of the target spacecraft, and the y-axis completes the right-handed framework. In this setup, the central body is situated in the negative x-direction, and the y-axis aligns with the velocity vector of the target spacecraft. Movement along the y-axis is referred to as 'along-track,' while motion along the positive and negative z-axes is termed 'out-of-plane' motion. The closed form solutions are given by:

$$x(t) = (4 - 3\cos nt)x_0 + \frac{\sin nt}{n}\dot{x}_0 + \frac{2}{n}(1 - \cos nt)\dot{y}_0 \tag{3.4}$$

$$y(t) = 6(\sin nt - nt)x_0 + y_0 - \frac{2}{n}(1 - \cos nt)\dot{x}_0 + \frac{4\sin nt - 3nt}{n}\dot{y}_0 \tag{3.5}$$

$$z(t) = z_0 \cos nt + \frac{\dot{z}_0}{n}\sin nt \tag{3.6}$$

with the mean motion being:

$$n = \sqrt{\frac{\mu}{a^3}} \approx \sqrt{\frac{\mu}{r^3}} \tag{3.7}$$

The relative CW dynamics have been developed under the assumption that the chief's orbit is near circular. This is the reason the above equation is valid, but it will constrain the use of the CW guidance to limited eccentricity. For higher eccentricity values (>0.05), targeting the guidance solution leads to discrepancies between the model and reality, Wang et al. 2017. Wang et al. have performed numerical simulations using the most promising relative models.

To achieve the guidance solution, the position along the trajectory is not important. In other words, the phase angle of the deputy in the formation (represented by nt) is not important because the set of equation is only used to describe the guidance relative orbit. By further developing the CW equation, the following state and state derivative were obtained:

$$x(0) = x_0 \tag{3.8}$$

$$y(0) = y_0 \tag{3.9}$$

$$z(0) = z_0 \tag{3.10}$$

A closed-form solution can be obtained that is solely depending on the initial condition and the chief's mean motion. This equation do not require integration assuming the chief's mean motion remain constant. The closed-form solution is given by:

$$\dot{x}(t) = 3nx_0 \sin nt + \dot{x}_0 \cos nt + 2\dot{y}_0 \sin nt \tag{3.11}$$

$$\dot{y}(t) = -6nx_0(1 - \cos nt) - 2\dot{x}_0 \sin nt + \dot{y}_0(4\cos nt - 3) \tag{3.12}$$

$$\dot{z}(t) = -nz_0 \sin nt + \dot{z}_0 \cos nt \tag{3.13}$$

The acceleration for the linearized CW equation are straightforward and are presented below:

$$\ddot{x}(t) = 3n^2 + 2ny \tag{3.14}$$

$$\ddot{y}(t) = -2nx \tag{3.15}$$

$$\ddot{z}(t) = -n^2 \tag{3.16}$$

Note, the mean motion "n" is often denoted as the ω. To avoid confusion with the rotation rate of coordinates, frames "n" is used here.

General Circular Orbit The GCO formation is a relative trajectory where a deputy follows a circle with respect to the chief. This can be achieved by settings the following constraint on the orbit. The relative orbit must be bounded by a constant radius, as seen below.

$$x^2 + y^2 + z^2 = r^2 \tag{3.17}$$

The implementation of the aforementioned constraint in the CW equation results in a set of initial conditions that satisfy the requirements for a GCO formation. The initial conditions are as follows:

$$y_0 = 2\dot{x}_0/n \tag{3.18}$$
$$z_0 = \pm\sqrt{3}x_0 \tag{3.19}$$
$$\dot{y}_0 = -2nx_0 \tag{3.20}$$
$$\dot{z}_0 = \pm\sqrt{3}\dot{x}_0 \tag{3.21}$$

By settings the along-track drift and formation offset to zero, the first two initial conditions were derived. There are two possible planes that intersect the cross-track/along-track plane along the along-track direction at an angle of $\pm$30 deg, respectively. In this case, x_0 and $\dot{x}_0$ are free variables and used to design the formation. These parameters have been expressed in terms of the design radius and phase of the formation.

$$x_0 = (r_d/2)\cos\phi \tag{3.22}$$
$$\dot{x}_0 = -(r_d n/2) * \sin\phi \tag{3.23}$$

Where ϕ is the initial phase angle and r_d is the desired radius of the GCO formation. The GCO formation can be achieved by differences in the right ascension of the ascending node, argument of perigee and true anomaly. The circular formation possesses two compelling attributes: (1) spacecraft within it maintain a consistent spacing, and (2) unlike in-plane and in-track formations, the circular formation evolves in both the along-track and cross-track planes.

Projected Circular Formation The projected circular formation closely resembles the circular formation, with the key distinction being that the circular relative motion occurs in the along-track/cross-track (y-z) plane rather than the ±30-degree inclined plane. In simpler terms, with the projected circular formation, the ellipse of relative motion, when projected onto the along-track/cross-track plane, takes on a circular shape. To adhere to this configuration, the following constraint must be met:

$$x^2 + y^2 + z^2 = r^2 \tag{3.24}$$

Just like with the circular formation, the initial conditions need to be configured to

$$y_0 = 2\dot{x}_0/n \tag{3.25}$$
$$z_0 = \pm 2x_0 \tag{3.26}$$
$$\dot{y}_0 = -2nx_0 \tag{3.27}$$
$$\dot{z}_0 = \pm 2\dot{x}_0 \tag{3.28}$$

The first two conditions are applied to eliminate along-track drift and offset, while the last two conditions define the plane in which the elliptical formation evolves. This plane of relative motion intersects the cross-track/along-track plane along the along-track axis at an angle of ±26.565 degrees, ensuring that its projection forms a circle in the along-track/cross-track (y - z) plane. The two parameters, x_0 and $\dot{x}_0$, which remain free, determine the radius and phasing of the projected circular motion, as outlined below:

$$x_0 = (r_d/2)\cos\phi \tag{3.29}$$
$$\dot{x}_0 = -(r_d n/2) * \sin\phi \tag{3.30}$$

Similar to the circular formation, the differences in orbital elements are observed in inclination, right ascension of the ascending node, argument of perigee, and true anomaly. The notable advantage of the PCO, when compared to the GCO, is that the spacecraft maintain a fixed separation distance when projected onto the along-track/cross-track (y - z) plane. This particular feature has various valuable applications in Earth observation.

3.3.2. Energy Matching Condition

The influence of the J_2 potential introduces the risk of spacecraft either drifting apart or colliding. To maintain a desired separation, Morgan and Chung 2012 introduced an energy matching condition that accounts for both the J_2 potential's impact on cross-track motion and the gravity gradient's effect on relative motion. In an unperturbed orbit, cross-track motion remains decoupled from in-plane motion. However, the J_2 potential induces coupling of spacecraft motion in all three directions. This leads to a gradual drift of spacecraft in the along-track direction, Morgan and Chung 2012. Similarly, when considering a spherical Earth, the gravity gradient vector solely acts in the radial direction. However, the gravity gradient, which incorporates the J_2 potential, influences motion in all three directions, Xu and Wang 2008. This divergence in gravity gradient behavior results in significant relative drift among the spacecraft. To mitigate these sources of drift, Morgan and Chung 2012 employed energy matching, ensuring that the deputy spacecraft possesses the same energy as the chief spacecraft. This matching process minimizes the drift and helps maintain the desired formation.

The energy matching condition is formulated by equating the energy difference between the chief and deputy spacecraft to zero, as depicted by

- $\delta \bar{E}_j = 0$

The first of the energy matching condition can be derived by using $\delta H_j = H_j = H = 0$, which results to:

$$v_{jx}\Big(z_j c_\theta s_i - y_j c_i\Big) + v_{jy}\Big((x_j + r)c_i - z_j s_\theta s_i\Big) + v_{jz}\Big(y_j s_\theta - (x_j + r)c_\theta\Big)s_i = h c_i \tag{3.31}$$

With θ, i, h being the orbital oscillation orbital elements of the chief. Here, x_j, y_j, z_j indicate the position of the i^{th} deputy in the LVLH frame. Here c_i and s_i denote $\cos i$ and $\sin i$ for ease of reading Equation 3.31. Next, the secondary condition can be developed by setting the total energy of the system equal to each other, $K + U = K_j + U_j$, as seen below

$$U = -\frac{\mu}{r} - \frac{k_{J_2}}{3r^3} + \frac{k_{J_2}\sin^2\theta \sin^2 i}{r^3} \tag{3.32}$$

$$U_j = -\frac{\mu}{r_j} - \frac{k_{J_2}}{3r_j^3} + \frac{k_{J_2} r_{jZ}^2}{r_j^3} \tag{3.33}$$

with:

$$r = \sqrt{(r + x_j)^2 + y_j^2 + z_j^2} \tag{3.34}$$

$$r_j = (r + x_j)\sin i \sin\theta + y_j \sin i \cos\theta + z_j \cos i \tag{3.35}$$

Continuing from the derivation outlined in Xu et al. 2009, the second condition can be established.

$$v_{jx}^2 + v_{jy}^2 + v_{jz}^2 = v_x^2 + \frac{h^2}{r^2} + 2\mu(\frac{1}{r_j} - \frac{1}{r}) + 2k_{J_2}(\frac{1}{3r_j^3} - \frac{1}{3r^3} - \frac{r_{jZ}^2}{r_j^5} + \frac{\sin^2\theta \sin^2 i}{r^3}) \tag{3.36}$$

Finally, several clarifications are made for correct implementation of the equations. First, it is important to note that v_x is the time derivative of the radial vector and not the time derivative of the 3D velocity vector. Secondly, the velocity referred to in Equation 3.36 pertains to the velocity within the LVLH reference frame. However, it is important to note that this velocity is measured at the center of the Earth, rather than at the location of the chief satellite. To transition from velocity to the appropriate frame, the following transformation is employed:

$$\dot{x} = v_{jx} - v_x + y_j \omega_z \tag{3.37}$$

$$\dot{y} = v_{jy} - (r + x_j)\omega_z + z_j \omega_x \tag{3.38}$$

$$\dot{z} = v_{jz} - y_j \omega_z \tag{3.39}$$

with

$$\omega_x = -\frac{k_{J_2} \sin 2i \sin\theta}{hr^3}, \qquad \omega_z = \frac{h}{r^2} \tag{3.40}$$

Much like Xu et al. 2009, Morgan and Chung 2012 also devised a quasi-periodic energy matching condition through nonlinear dynamics. This energy matching condition, uses a less straight forwards implementation than the condition proposed by Xu et al. 2009. What sets this energy matching condition apart is its versatility, it can be applied to various formation types, including the notably stable in-plane formation, Xu et al. 2009. The outcome of this energy matching condition is the synchronization of the orbital periods between the chief and deputy spacecraft, effectively minimizing relative drift. To attain the energy matching condition, Equation 3.31 and Equation 3.36 are solved using a Scipy's 'Solve' module. Due to the inherent dynamics of the problem, one of the velocities must be held constant in order to calculate the remaining two. The default value chosen for v_x in this context is 0.02 m/s, which allow the movement in the x-axis. Selected a non-zero value, aids the convergence of the controller due to coupling of the radial and along-track dynamics.

3.3.3. Guidance Dynamics

This section will focus on the construction of the guidance solution. So far, the initial conditions have been developed based on the desired geometry of the formation. Moreover, here the initial condition for a GCO, PCO and energy-matched formation are presented. The goal of this subsection is to connect these initial conditions to the desired formation type. Additionally, the methodology of the guidance solution is further explained. This includes propagation of the guidance dynamics to obtain a guide solution describing a circle or ellipse.

The formations that have been addressed in Chapter 2 are the ATO, ITO, GCO and PCO formation. For the ATO and ITO formation, the guidance solution is obtained by the initial condition only as no perpetual motion is present. However, both the GCO and PCO describe a sphere or ellipse, which can be achieved by propagating the earlier presented initial condition with a dynamical model. Lastly, the energy-matched condition describes an ellipse with a varying radius which is also propagated. An overview of the guidance aspects for each of the formation can be found below:

Formation Type	Propagation	EOM
ATO/ITO	None	None
GCO	Active	CW dynamics
PCO	Active	CW dynamics
Energy-Matched	Active	Perturbed dynamics

Table 3.1: An overview of the dynamics used for the guidance solution per formation type.

3.4. Equation of Motion

The objective of this section is to outline the fundamental equations governing the motion. These dynamics can be segregated into two distinct components: the chief dynamics, often referred to as absolute dynamics, and the deputy dynamics, denoted as relative dynamics. First, the absolute dynamics are presented, which use a set of RSV to describe the chief's orbit. Next, by utilizing a combination of state and state derivatives of the chief, the relative dynamics are described.

3.4.1. Absolute Dynamics

The basis of the chief dynamics have been developed by Xu and Wang 2008 in the form of RSV. This formulation excels in the ease at which the state derivative can be calculated. The RSV can be constructed for a reference (chief) satellite in an arbitrary orbit in the presence of spherical and oblate gravitational potential. The concerning equation is

$$\ddot{\boldsymbol{r}} = -\nabla U \tag{3.41}$$

where

$$U = -\frac{\mu}{r} - \frac{3J_2\mu R_e^2}{2r^3}\left(\frac{1}{3} - \sin^2\phi\right) \tag{3.42}$$

The RSV defined by Xu and Wang (2008) is presented below Xu and Wang 2008:

$$r = v_x \tag{3.43}$$

$$\dot{v_x} = -\frac{\mu}{r^2} + \frac{h^2}{r^3} - \frac{k_{J2}}{r^4}(1 - 3\sin^2 i \sin^2\theta) \tag{3.44}$$

$$\dot{h} = -\frac{k_{J2}\sin^2 i \sin 2\theta}{r^3} \tag{3.45}$$

$$\dot{\Omega} = -\frac{2k_{J2}\cos i \sin^2\theta}{hr^3} \tag{3.46}$$

$$\dot{i} = -\frac{k_{J2}\sin 2i \sin 2\theta}{2hr^3} \tag{3.47}$$

$$\dot{\theta} = \frac{h}{r^2} + \frac{2k_{J2}\cos^2 i \sin^2\theta}{hr^3} \tag{3.48}$$

This model was extended by Morgan and Chung 2012 to include atmospheric drag.

$$r = v_x \tag{3.49}$$

$$\dot{v_x} = -\frac{\mu}{r^2} + \frac{h^2}{r^3} - \frac{k_{J2}}{r^4}(1 - 3\sin^2 i \sin^2\theta) - C||\boldsymbol{V}_a||v_x \tag{3.50}$$

$$\dot{h} = -\frac{k_{J2}\sin^2 i \sin 2\theta}{r^3} - C||\boldsymbol{V}_a||(h - \omega_e r^2 \cos i) \tag{3.51}$$

$$\dot{\Omega} = -\frac{2k_{J2}\cos i \sin^2\theta}{hr^3} - \frac{C||\boldsymbol{V}_a||\omega_e r^2 \sin 2\theta}{2h} \tag{3.52}$$

$$\dot{i} = -\frac{k_{J2}\sin 2i \sin 2\theta}{2hr^3} - \frac{C||\mathbf{V}_a||\omega_e r^2 \sin i \cos^2\theta}{h} \tag{3.53}$$

$$\dot{\theta} = \frac{h}{r^2} + \frac{2k_{J2}\cos^2 i \sin^2\theta}{hr^3} + \frac{C||\mathbf{V}_a||\omega_e r^2 \cos i \sin 2\theta}{2h} \tag{3.54}$$

These equations can be extended further to include maneuvering of the chief. The state derivatives will be used in the expression for relative dynamics, thus, the thrust acceleration of the chief should be included in the derivation of the absolute model. Since all thrust acceleration are expressed in the LVLH frame, a conversion is made to obtain the acceleration in the perifocal coordinate frame. This results in the following equation of motion:

$$r = v_x \tag{3.55}$$

$$\dot{v_x} = -\frac{\mu}{r^2} + \frac{h^2}{r^3} - \frac{k_{J2}}{r^4}(1 - 3\sin^2 i \sin^2\theta) - C||\boldsymbol{V}_a||v_x + u_{l,x} \tag{3.56}$$

$$\dot{h} = -\frac{k_{J2}\sin^2 i \sin 2\theta}{r^3} - C||\boldsymbol{V}_a||(h - \omega_e r^2 \cos i) + u_{l,y} r \tag{3.57}$$

$$\dot{\Omega} = -\frac{2k_{J2}\cos i \sin^2\theta}{hr^3} - \frac{C||\boldsymbol{V}_a||\omega_e r^2 \sin 2\theta}{2h} + u_{l,z}\frac{r\sin\theta}{h\sin(i)} \tag{3.58}$$

$$\dot{i} = -\frac{k_{J2}\sin 2i \sin 2\theta}{2hr^3} - \frac{C||\mathbf{V}_a||\omega_e r^2 \sin i \cos^2\theta}{h} + u_{l,z}\frac{r}{h}\cos\theta \tag{3.59}$$

$$\dot{\theta} = \frac{h}{r^2} + \frac{2k_{J2}\cos^2 i \sin^2\theta}{hr^3} + \frac{C||\mathbf{V}_a||\omega_e r^2 \cos i \sin 2\theta}{2h} - u_{l,z}\frac{r}{h}\sin\theta\cot i \tag{3.60}$$

In order to simulate the atmosphere from Earth on the satellite, Earth's rotation is used, and the atmosphere is fixed with respect to Earth's surface, Morgan and Chung 2012. The rotation rate of the Earth is expressed in the LVLH frame by:

$$\boldsymbol{\omega}_e = \omega_e \hat{Z} = \omega_e(\sin\theta \sin i\hat{x} + \cos\theta \sin i\hat{y} + cos\ i\hat{z}) \tag{3.61}$$

To simplify reading of the above equations, the following drag constant is used:

$$C = \frac{1}{2}C_d\frac{A}{m}\rho \tag{3.62}$$

In Equation 3.62, C_d is the drag coefficient, A is the drag area, m is the mass and ρ is the density of the atmosphere. During simulation, both the drag area and drag coefficient will remain constant. It is important to note that this assumption leads to underestimation of drag, since the simulation is performed using the low-drag orientation whereas as a consequence of the maneuvering, the attitude will vary over time. Nevertheless, this conservative approach will be used for this version of the software and the associate unaccounted error is accepted for now.

Another constant used in the state derivative of the RSV is the k_{J2} which is defined by:

$$k_{J_2} = \frac{3J_2\mu R_e^2}{2} \tag{3.63}$$

where J_2 is the spherical harmonic term, μ is the gravitational parameter of Earth, and R_e is the equatorial radius of Earth.

3.4.2. Relative Dynamics

Following from the derivation of the RSV chief dynamics, Xu and Wang 2008 derived a set of nonlinear equations that describe the motion of an arbitrary deputy j with respect to the chief. The equations were derived using the Lagrangian expression of kinetic and potential energy. The Lagrangian formation for a satellite with respect to another satellite can be constructed by

$$\frac{d}{dt}\Big(\frac{\delta K_j}{\delta \dot{\boldsymbol{q}}_j}\Big) - \frac{\delta K_j}{\delta \boldsymbol{q}_j} + \frac{\delta U_j}{\delta \boldsymbol{q}_j} = \boldsymbol{a}_j \tag{3.64}$$

where q_j and $\dot{q}_j$ represent the position and velocity of the satellite, respectively. By using the expressing for relative kinetic energy and differential potential due to J_2, Xu and Wang 2008 developed a set of exact nonlinear equations for relative dynamics. The model was extended to include drag by Morgan and Chung 2012. This final implementation is used here to describe a deputy satellite with respect to a chief. The exact nonlinear equations of relative motion are

$$\begin{aligned}\ddot{x}_j = {} & 2\dot{y}_j\omega_z - x_j(\eta_j^2 - \omega_2^2) + y_j\alpha_z - z_j\omega_x\omega_z \\ & - (\zeta_j - \zeta)\sin i\sin\theta - r(\eta_j^2 - \eta^2) \\ & - C_j||\boldsymbol{V}_{aj}||(\dot{x}_j - y_j\omega_z) \\ & - (C_j||\boldsymbol{V}_{aj}|| - C||\boldsymbol{V}_a||)v_x + a_{j,x}\end{aligned} \tag{3.65}$$

$$\begin{aligned}\ddot{y}_j = {} & -2\dot{x}_j\omega_z + 2\dot{z}_j\omega_x - x_j\alpha_z - y_j(\eta_j^2 - \omega_z^2 - \omega_x^2) \\ & + z_j\alpha_x - (\zeta_j - \zeta)\sin i\cos\theta \\ & - C_j||\boldsymbol{V}_{aj}||(\dot{y}_j + x_j\omega_z - z_j\omega_x) \\ & - (C_j||\boldsymbol{V}_{aj}|| - C||\boldsymbol{V}_a||)\Big(\frac{h}{r} - \omega_e r\cos i\Big) + a_{j,y}\end{aligned} \tag{3.66}$$

$$\begin{aligned}\ddot{z}_j = {} & -2\dot{y}_j\omega_x - x_j\omega_x\omega_z - y_j\alpha_x \\ & - z_j(\eta_j^2 - \omega_x^2) - \zeta_j - \zeta)\cos i \\ & C_j||\boldsymbol{V}_{aj}||(\dot{z}_j + y_j\omega) \\ & - (C_j||\boldsymbol{V}_{aj}|| - C||\boldsymbol{V}_a||)\omega_e r\cos\theta\sin i + a_{j,z}\end{aligned} \tag{3.67}$$

In order to simplify the notation of the equations, several variables were defined. These include the nonlinear terms $\zeta, \zeta_j, \eta, \eta_j$ and their definition can be seen below:

$$\zeta = \frac{2k_{J2}\sin i\cos\theta}{r^4} \tag{3.68}$$

$$\zeta_j = \frac{2k_{J2}r_{jZ}}{r_j^5} \tag{3.69}$$

$$\eta^2 = \frac{\mu}{r^3} + \frac{k_{J2}}{r^5} - \frac{5k_{J2}}{\sin^2 i\sin^2\theta} \tag{3.70}$$

$$\eta_j^2 = \frac{\mu}{r_j^3} + \frac{k_{J2}}{r_j^5} - \frac{5k_{J2}r_{jZ}^2}{r_j^7} \tag{3.71}$$

Note, a discrepancy was found in the definition of η^2. The model presented by Morgan and Chung 2012 has been inspired by the work done by Xu and Wang 2008, however, regarding Morgan the denominator of the last term states r^5 instead of r^7. By performing detailed analysis, the mistake was found in the model presented by Morgan, so r^7 is used throughout the construction of the algorithms. This analysis included the implementation of both model and visualizing their stability, which clearly showed the incorrectness using r^5. Next, r_j represents the position vector of the deputy, the r_{jZ} term is used to denote the projection of r_j on the Z-axis of the Earth Centered Interial (ECI) coordinate system. These variable can be easily obtained by using the following equations:

$$r_j = \sqrt{(r+x_j)^2 + y_j^2 + z_j^2} \tag{3.72}$$

$$r_{jZ} = (r+x_j)\sin i\sin\theta + y_j\sin i\cos\theta + z_j\cos i \tag{3.73}$$

The value of C_j pertains to the j-th deputy spacecraft, with distinct values assigned to each deputy (C_j). Generally, the drag coefficient ($C_{d,j}$), cross-sectional area (A_j), and mass (m_j) may vary among individual spacecraft. However, for the sake of simplification in simulations, all spacecraft are considered to possess the same shape and mass. The function describing the deputy drag constant can be seen below:

$$C_j = \frac{1}{2}C_{d,j}\frac{A_j}{m_j}\rho_j \tag{3.74}$$

The rotation rate of the LVLH frame in the radial, along-track and cross-track are defined by:

$$\omega_x = -\frac{k_{J2}\sin 2i\sin\theta}{hr^3} - \frac{C||\boldsymbol{V}_a||\omega_e r^2\cos\theta\sin i}{h} \tag{3.75}$$

$$\omega_y = -\dot{i}\sin\theta + \dot{\Omega}\cos\theta\sin i = 0 \tag{3.76}$$

$$\omega_z = \dot{\theta} + \dot{\Omega}\cos i = \frac{h}{r^2} \tag{3.77}$$

Resulting from the definition of the LVLH frame, the rotation rate in the y (along-track) direction is zero. Using the RSV elements to describe the rotation rates, the influence of J_2, drag and maneuver is included. Next, the steering acceleration (α_x) and orbital acceleration (α_z) can be obtained by performing the time derivative of the rotation rates and can be seen below:

$$\alpha_x = \dot{\omega}_x = -k_{J2}\Big(\frac{2\cos 2i\sin\theta}{hr^3}\dot{i} + \frac{\sin 2i\cos\theta}{hr^3}\dot{\theta} - \frac{\sin 2i\sin\theta}{h^2r^3}\dot{h} + \frac{3\sin 2i\sin\theta}{hr^4}\dot{r}\Big) \tag{3.78}$$

$$- C||\boldsymbol{V}_a||\omega_e\Big(\frac{r^2\cos\theta\cos i}{h}\dot{i} - \frac{r^2\sin\theta\sin i}{h}\dot{\theta} - \frac{r^2\cos\theta\sin i}{h^2}\dot{h} + \frac{2r\cos\theta\sin i}{h^2}\dot{h} + \frac{2r\cos\theta\sin i}{h}\dot{r} \tag{3.79}$$

$$+ \frac{u_{l,z}}{h} - \frac{u_{l,z}r}{h^2}\dot{h} \tag{3.80}$$

$$\alpha_y = \dot{\omega}_y = 0 \tag{3.81}$$

$$\alpha_z = \dot{\omega}_z = \frac{\dot{h}}{r^2} - \frac{2h}{r^3}\dot{r} \tag{3.82}$$

As a consequence of the rotation rate in the y-direction, it is evident that the angular acceleration in the y-direction is likewise zero. Equation 3.78 has been derived with the assumption that the thruster acceleration provided by the chief is constant and does not vary over time, which is a valid assumption since the chief will occasionally perform orbit raising maneuvers with constant thrust.

The implementation of differences in the ballistic properties between satellite has been included by the equations presented by Morgan and Chung 2012. The velocity vector perceived by the deputy with respect to the atmosphere is represented by:

$$\boldsymbol{V}_{aj} = \boldsymbol{V}_a + \dot{\boldsymbol{l}}_j + \boldsymbol{\omega} \times \boldsymbol{l_j} \tag{3.83}$$

Where $\boldsymbol{l_j}$ and $\dot{\boldsymbol{l}}_j$ are the relative position and velocity vectors from the deputy to the chief, respectively. $\boldsymbol{\omega}$ represents the rotation rate vector in x,y,z direction.

3.5. Controller

The SMC represents a nonlinear control approach that calculates the optimal control input for guiding the deputy satellite to its intended orbit, denoted by the subscript ”d”. Employing a Lyapunov-based controller along with the Lyapunov stability analysis technique, this approach establishes a closed-loop system characterized by global asymptotic stability, Liu and Hexi 2006. Thier study focussed on the implementation of a sliding mode controller for low thrust control of a formation flying. Following a coordinated control schemed based on a leader-follower approach, formation keeping was achieved using nonlinear equations of relative motion. A SMC with nonlinear dynamics was used to achieve formation keeping. The original implementation of the SMC presented by Liu and Hexi 2006 is as follows:

$$\boldsymbol{u}_f = \boldsymbol{C}(\cdot)\dot{\boldsymbol{\rho}} + \boldsymbol{N}(\cdot) + \ddot{\boldsymbol{\rho}}_d - \boldsymbol{\lambda}(\dot{\boldsymbol{\rho}} - \dot{\boldsymbol{\rho}}_{\boldsymbol{d}}) - ksat(\boldsymbol{S}, \epsilon) \tag{3.84}$$

The SMC as originally presented by Liu and Hexi 2006 is followed with several adaptations to better simulate a real mission scenario. To begin with, we focus on how disturbances are formulated within the controller. Instead of using a simulated bounded function with noise, the adaptation incorporates the effect of J_2 and is a consequence of using the dynamics model presented by Xu and Wang 2008. While calculating unforced acceleration and desired acceleration, drag effects are deliberately omitted to enhance control convergence. In this phase of the analysis, excluding drag was considered appropriate. Incorporating atmospheric drag is feasible, but necessitates incorporating drag into both actual and desired dynamics. Nevertheless, developing a sophisticated formation that considers both J_2 and drag has not been extensively explored, as the primary focus of the software lies in analyzing complex formations. Introducing drag would amplify the complexity of the guidance solution for such formations. Secondly, whereas the original implementation returned a thrust magnitude and direction, several adaptations are made to incorporate various thrusters and will be explained in the thruster implementation paragraph.

After including the above describe adaptation, the main controller law of the nonlinear sliding mode controller is defined by

$$\boldsymbol{u}_f = \ddot{\boldsymbol{\rho}}_{\boldsymbol{d}} - \ddot{\boldsymbol{\rho}}_{nf} - \boldsymbol{\lambda}(\dot{\boldsymbol{\rho}} - \dot{\boldsymbol{\rho}}_{\boldsymbol{d}}) - ksat(\boldsymbol{S}, \epsilon) \tag{3.85}$$

The desired trajectory is often partly fixed by the mission or maneuvering capability. The initial desired state is a result of the formation design and is propagated using unperturbed or perturbed motion, which depends on the type of formation. For example, an ordinary GCO formation is derived using the CW equation and are thus propagated using unperturbed dynamics. In contrary, EM matched formation are propagated using J_2 perturbation. To clarify, unperturbed dynamics include nonlinear equations for a spherical Earth, whereas perturbed dynamics include nonlinear equations with an oblate Earth.

The objective of the sliding mode is to reduce the tracking error to zero. In order to achieve this, the controller requires a combination of the relative position, velocity, and acceleration. Tracking error are defined by

$$\boldsymbol{e} = \boldsymbol{\rho} - \boldsymbol{\rho}_d \tag{3.86}$$

$$\dot{\boldsymbol{e}} = \dot{\boldsymbol{\rho}} - \dot{\boldsymbol{\rho}}_d \tag{3.87}$$

The function $sat(\boldsymbol{S}, \epsilon)$ represents a continuous saturation function, designed to mitigate chattering, as introduced by, Liu and Hexi 2006. Here, the design parameter ϵ signifies the width of the boundary layer.

$$sat(\boldsymbol{S}, \epsilon) = \begin{cases} \boldsymbol{S}/\epsilon & \text{if } |\boldsymbol{S}| < \epsilon \\ sgn(\boldsymbol{S}) & \text{if } |\boldsymbol{S}| \geq \epsilon \end{cases} \tag{3.88}$$

In Equation 3.85 the signum function is defined by:

$$sgn(\boldsymbol{S}) := \begin{cases} -1 & \text{if } \boldsymbol{S} < 0 \\ 0 & \text{if } \boldsymbol{S} = 0 \\ 1 & \text{if } \boldsymbol{S} > 0 \end{cases} \tag{3.89}$$

The parameters k,λ and ϵ are design parameter for used for the optimization are :

$$k = 0.96 \tag{3.90}$$
$$\lambda = [10^{-3}, 10^{-3}, 10^{-3}] \tag{3.91}$$
$$\epsilon = 10 \tag{3.92}$$

The utilization of these specific values for k,λ and ϵ serve two crucial purposes: firstly, it streamlines the optimization process by reducing the number of parameters that require fine-tuning. Secondly, these values have already undergone optimization to address chatter in the controller Yeh et al. 2002.

Chatter, in this context, refers to the unwanted vibrations within the system. These vibrations result in fluctuations and oscillations occurring at higher frequencies within the controller's operation. For instance, if the controller commands a thrust level of zero, the presence of chatter can cause the output to exhibit slight oscillations around the zero point instead of remaining steady. This behavior is undesirable, which is why the pre-optimized parameters are implemented to mitigate it effectively.

For the original implementation of the SMC by Liu and Hexi 2006, it has been demonstrated that an accuracy of 12 meter was reached after 1 orbit. This simulation analyzed a reconfiguration maneuver going from a 1.49 km GCO to a 1 km GCO. In the end, this controller was able to converge to a tracking error 0 to 1 meter. This is deemed sufficient, following from the expected accuracy of the navigation solution. Following the control scheme presented in Chapter 1, the navigation solution is propagated and then used as the initial condition for the guidance and control system. At this stage, the position error with respect to the real position is expected to have reached a value of 10 meters. The ability of the controller convergence and final position error will be discussed in Chapter 5 as this is dependent on the initial condition, formation design and thruster implementation.

Thrust Implementation As has been previously mentioned, the output of the SMC returns the thrust magnitude and direction. In Chapter 5, different types of thruster will be analyzed. First, the control acceleration and direction given by the SMC are used directly. As can be seen in the simulation performed by Liu et al., the thruster acceleration magnitude is able to reach up to 1 m/s^2. Nowadays, thruster have improved significantly to allow throttling, but a thrust acceleration between 0 and 1 m/s^2 is not realistic. Therefor, the constraints and performance of a thruster currently used in the RNLAF is implemented. The thruster is used for the reference mission is able to produce a thrust of up to 330μN. Two additional thruster implementation are thus considered. First, the thruster is allowed to continuously vary its thrust between 50μN and 330μN.

$$\boldsymbol{a}_j = \begin{cases} \frac{\boldsymbol{u_f}}{||\boldsymbol{u_f}||} \cdot \frac{T_{max}}{m} & \text{if } ||\boldsymbol{T}|| < T_{max} \\ \boldsymbol{u}_f & \text{if } |\boldsymbol{T}| > T_{min} \text{ and } ||\boldsymbol{T}|| > T_{max} \\ 0 & \text{if } ||\boldsymbol{T}|| < T_{min} \end{cases} \tag{3.93}$$

where m is the instantaneous mass of the satellite, T_{min} is the minimum thrust and T_{max} is the maximum thrust, fixed by the thruster selection. In the final scenario, the assumption is made that the thruster is configured with a fixed thruster setting. Consequently, the output generated by the SMC provides

us solely with information about the thruster's direction and an activation signal, aimed at preventing excessive satellite rotation. To translate the control acceleration derived from the SMC into a useful directive, a normalization process is necessary. This leads to the subsequent correction:

$$\boldsymbol{a}_j = \frac{\boldsymbol{u_f}}{||\boldsymbol{u_f}||} \cdot \frac{T_{max}}{m_j} \tag{3.94}$$

ΔV Implementation An effective metric for comparing the efficiency of maneuvers is to compute the delta-V (change in velocity), which is derived at each step of the integration process using the Tsiolkovsky rocket equation Vallado 2013. Given that the impact of drag is minimal, it is reasonable to employ this equation to determine the delta-V accurately. The definition of the rocket equation is presented below:

$$\Delta V = I_{sp} \cdot g_0 \cdot \ln \frac{m_0}{m_f} \tag{3.95}$$

where I_{sp} is the specific impulse, g_0 the gravity acceleration at sea-level, and $\frac{m_0}{m_f}$ the mass ratio. The mass ratio can be easily computed by dividing the initial mass by the final mass. The instantaneous mass is calculated at each step of the integration and depends on the thrust acceleration and activation. The mass for a new time step is determined as follows:

$$m_{t+1,j} = \begin{cases} m_{t,j} + \dot{m}_{t,j} \cdot \Delta t & \text{if } ||\boldsymbol{a_j}|| > 0 \\ m_{t,j} & \text{if } ||\boldsymbol{a_j}|| = 0 \end{cases} \tag{3.96}$$

with

$$\dot{m}_{t,j} = -\frac{T_j}{g_0 I_{sp}} \tag{3.97}$$

Constraints The critical aspect of constraints within the context of satellite formation optimization will now be discussed. Constraints play a pivotal role in shaping the trajectory and final configuration of satellite formations. By understanding the role of constraints, valuable insights into the intricacies of achieving precise and efficient satellite formations in space can be gained.

Following from the normalization, a trivial constraint had already been presented. The thruster direction for the ranging and fixed thruster are constraint such that the norm does is away one, as presented by

$$u_{j,x}^2(t) + u_{j,y}^2(t) + u_{j,z}^2(t) = 1, \ \forall \ t \in [t_0, t_f] \tag{3.98}$$

Although the simulation will not address the full mission duration, a final mass constraint is imposed to prevent fuel expenditure beyond the fuel capacity.

$$m_j(t) \geq m_{j,dry}, \ \forall \ t \in [t_0, t_f] \tag{3.99}$$

A limited number of published works have delved into the domain of optimizing the final conditions for satellite formation trajectories. However, it is worth noting that many of these works typically establish the final states of satellites as predefined fixed points. For instance, Richards et al. 2002 took an approach where they defined various subsets of final states and meticulously evaluated each subset during the trajectory optimization process. Eventually, the subset that incurred the least fuel cost overall was chosen.

Huntington and Rao 2005 formulated the final configuration constraints specifically for tetrahedral formations. Different convergence conditions are presented depending on the design of the formation.

In the first method, the condition presumes fixed final relative states, which are determined in advance using an analytic formation design method, as proposed by Sabol et al. 2001. For upcoming simulations the final condition constraint is defined by

$$\left| \sqrt{x_j^2 + y_j^2 + z_j^2} - r_d \right| \leq \epsilon_1 \tag{3.100}$$

which describes the difference between the actual radius and the desired radius. This condition only applies for circular formations such as the GCO and PCO.

In the second method, the final relative states are treated as variables within the optimization process. These states are then subjected to constraints related to the final geometric configuration and an energy-matching condition. This approach allows for the derivation of a desired final formation that is bounded within these constraints, as seen below.

$$\left|\frac{1}{2}\left[(\dot{x}_j - \omega_z y_j + \dot{r})^2 + [\dot{y}_j + \omega_z(x_j + r)]^2 + \dot{z}_j^2\right] - \mu/\sqrt{(r + x_j)^2 + y_j^2 + z_j^2} + \mu/2a\right| \leq \epsilon_2 \tag{3.101}$$

The constants ϵ_1 and ϵ_2 are used to select an acceptance level for the final formation.

4

Problem A: Navigation

In the pursuit of developing a comprehensive end-to-end guidance solution, it became evident that a navigation system was a requisite component for calculating the state vector essential for guidance and control. The data used for construction and verification of the navigation filter has been taken from a real satellite, named BRIK2 [1]. Utilizing real GPS data offers the advantage of incorporating all real environmental effects, facilitating the verification and validation of the navigation filter. The available GPS data from BRIK2 solely offered position estimates, necessitating the construction of a navigation system. This section aims to reinforce the mission's requirement for a navigation filter and assess its performance quantitatively. Through an analysis of the filter's capacity to provide a state estimate and enable sequential propagation, valuable insights will be gleaned for the guidance and control processes. Ultimately, this chapter will provide an overview of the simulation and the associate accuracy analysis.

4.1. Problem A: Mission Needs

Following from the scope presented in Chapter 1, an end-to-end GNC system is required with the capability to be used for various missions. The goal of this section is to lay out the needs for the navigation filter, reviewing the primary objectives, and present a general mission case. In the end, various practical constraints will be address. Recent advancements within the RNLAF have sparked an increased interest in formation flying missions. Depending on the mission's objectives, there may arise a demand for diverse formation configurations. Therefore, a strong need to develop software that is able to generate maneuvering for multiple satellites while staying in formation. The software shall be able to determine an accurate position estimate of the satellites such that a sufficiently accurate solution is fetched into the guidance and control. In the absence of an existing navigation filter, determining the needed accuracy for the guidance and control system becomes a challenging task. Consequently, the software has been enhanced with the incorporation of a navigation filter, which utilizes several hours of GPS data to formulate an accurate state estimate.

4.2. Navigation Filter

This section will touch upon the navigation system, explaining the need for a filter together with the reasoning for the selected algorithm and force model. The primary purpose of the navigation system is to determine the precise geographic position and velocity of a satellite. Generally, the geodetic coordinates are used to express the position a GNSS receiver. Here, the GNSS data is taken from the first satellite of the RNLAF, called BRIK2. The satellite is able to store and return the position and standard deviation of the navigation solution. BRIK2 is equipped with a GPS receiver able to generate a position estimate of around 8 m 3D RMS. The dataset used for the fitting and simulation had been retrieved in the months February, March, and April of the year 2023.

In the majority of the formation flying literature, the main focus is formation guidance and control and

[1] https://www.defensie.nl/actueel/nieuws/2021/01/25/nederland-lanceert-1e-militaire-nanosatelliet

the guidance solution often left out. The reviewed analyses often start by setting up the chief state by a target orbit and the deputy at an initial offset with respect to the desired guidance solution. The benefit of this implementation is that the sensitivity of the deputy controller can be analyzed without adapting the absolute state of the deputy. But, in order to use the formation flying control software, the navigation system is required to generate an estimation of the position and velocity. Other than providing a position and velocity, the navigation filter smooths out measurements, taking out outliers and increase overall accuracy. In the end, the final estimate of the state will be propagated over 1 to 3 orbit, during which the guidance and control software calculates the maneuver. Thus, the accuracy of final state estimate is important as error will be propagated over time.

A navigation solution is generated by fitting a batch of GPS measurements with the goal of increasing reliability and accuracy. Several methods for fitting exist, but only the Batch Least Squares (BLS) and EKF algorithm have been implemented in the GMAT 2022 build. As mentioned in section 3.2, the open source NASA software GMAT is used to generate an estimate of the orbit and to propagate the solution after orbit determination, which limit the choices to the BLS and EKF algorithm. Both algorithms have been widely used for orbit determination of spacecraft and generally show similar ability to perform orbit determination, Biswas and Dempster 2023. From preliminary tests, it was observed that the residuals of the final time for a BLS and EKF were within 1 meter. This simulation used the high-fidelity model described in section 3.2. Based on accuracy alone, the EKF algorithm was the best candidate in providing an estimation of the final state vector. Additionally, the current BLS implementation from GMAT does not allow for fixed time step integration, which was preferred for data analysis and post-processing. In the end, the choice was made to use an EKF over the BLS, but it must be said that the BLS is also a valid choice.

Atmosphere Model The atmospheric density is estimated using the MSISE90 model. This choice is primarily based on its pre-existing implementation in GMAT, which uses the most recent space weather data, including determined and predicted coefficients, is sourced from 'Celestrak' [2]. While the NRLMSISE00 model offers improved accuracy, incorporating it into GMAT as a custom implementation is not within the scope of this thesis. According to Picone et al. 2002, the NRLMSISE00 model incorporates various enhancements, such as total mass density from satellite accelerometers, temperature from incoherent scatter radar, and molecular oxygen number density, resulting in improved accuracy. However, research conducted by Park et al. 2008 has shown that the differences between these atmosphere models lead to only marginal improvements in model accuracy when using the NRLMSISE00 model. Therefore, the MSISE90 model is currently utilized, acknowledging the existence of a superior model, but due to time constraints, a transition to the NRLMSISE00 model is not feasible at this point.

4.3. Reference Case

This section will briefly describe the reference case used for the presented navigation solution. Several preliminary tests were performed using variants of the reference case, but those results will not be presented here. The main simulation was set up using the GMAT with the settings described in section 3.2. The GPS data used in the reference case was acquired by BRIK2 at the end of February, to be specific the 24th and 25th of February. At the that time, the solar activity was elevated to a 10% level of a minor solar storm, according to the data provided by 'SpaceWeatherLive'[3].

The simulation is set up using the following settings:

[2] https://celestrak.org/spacedata/
[3] https://www.spaceweatherlive.com/

Filter Parameters	Value
GPS data fitting duration [hrs]	12
GPS sampling time [s]	5
Propagation time [hrs]	24
Dry mass [hrs]	8
Cd [-]	2.2
Cr [-]	1.8
Drag area [m^2]	0.02
SRP area [m^2]	0.02

Table 4.1: Simulation settings used for the EKF.

During the acquisition of the GPS data, the satellite remained in a fixed orientation with respect to Earth, leading to a constant drag area. The least atmospheric drag attitude was chosen, which for a 6U SmallSat is 0.02 m^2. Additionally, both the drag and SRP coefficient had been set to the default a value of 2.2 and 1.8, respectively. The primary source of error in a navigation solution are related to atmospheric modelling, however, no extensive analysis has been performed to atmospheric modelling to improve the accuracy of the whole estimation arc since the accuracy of the final state is important. The primary focus of the analysis performed here is to attain an accurate final state such that the later propagation errors are reduced, and fuel expenditure due to modelling is minimized.

4.4. Implementation

The main core of the navigation filter has been constructed around GMAT, which is an excellent tool for fast and high-fidelity orbit propagation by using an intuitive combination of a GUI and custom scripts. The GMAT 2022 release enables the use of an EKF with a fixed time step integration. The benefit of using a fixed step size is that data analysis and verification does not require interpolation. Next to the GMAT code, a pre- and post-processing python tool have been developed. The pre-pocessing tool select the right data range and convert the selected data to the right format. On the other hand, the post-processing tool is primarily used for determination the performance of the algorithm. For a real mission, the post-processing tool is not needed, since the output of the GMAT filter will be fed directly into the formation guidance and control system. The goal of this section is to briefly describe the developed tools and discuss the choice made for the filter. Finally, the practical use of the navigation system for a real mission is discussed.

Propagation The propagation settings are a combination of the force model and integrator settings. The integrator used for the navigation filter and subsequent propagation of the solution is the PD78 (Prince Dormand 78). The current implementation of the PD78 integrator uses a fixed step size of 10 seconds to integrate the solution of time. The choice for the PD78 integrator was based on the combination of efficiency and accuracy. Figure 4.1 is retrieved from the GMAT manual and displays the accuracy and runtime of several mission scenarios for different integrators. It can be seen that for a LEO without propulsion the RKN68 is fastest and the PD45 is the most accuracy. However, the navigation solution must be generated for multiple satellites and must be attained within less than half of the orbit time. Therefore, an integrator was chosen that which is accurate whilst keeping the run time low. Following this reasoning, the best candidate for the integration was the PD78. The associate integration error is 0.006 meter, which is four orders lower than the physical input data of around 10 meter. So, this is integration error is excepted and will not lead to significant problem for the guidance and control system.

		RKV89	RKN68	RK56	PD45	PD78	ABM	PD853
ISS	Run Time	1.53	**1.00**	2.14	2.78	1.46	3.41	1.80
	Error (m)	0.003	64.060	0.022	0.002	0.006	0.012	0.013
Molniya	Run Time	1.32	1.47	1.99	3.08	**1.00**	3.35	1.92
	Error (m)	0.007	0.601	0.059	0.032	0.043	380.125	0.031
Lunar Flyby	Run Time	**1.00**	1.01	2.26	2.98	2.21	3.30	1.39
	Error (m)	0.063	0.017	0.002	0.023	0.000	0.236	0.080
Mars Transfer	Run Time	1.02	1.04	1.14	1.40	**1.00**	3.07	1.11
	Error (m)	0.030	0.001	0.043	0.194	0.009	25.231	0.030
Finite burn 1	Run Time	1.27	**N/A**	1.24	1.26	**1.00**	1.45	1.07
	Error (m)	0.002	N/A	0.006	0.002	0.002	0.000	0.002
Finite burn 2	Run Time	1.03	**N/A**	1.18	1.31	**1.00**	1.54	1.12
	Error (m)	0.002	N/A	0.000	0.000	0.001	0.003	0.002

Figure 4.1: Table taken from the GMAT User Guide which shows the accuracy and best use-case for each of the available integrators, The GMAT Development Team 2022. The results have been obtained by propagating a high-fidelity model for one day.

4.5. Results

In the following section, the navigation system will be discussed, highlighting the potential and constrains. By calculated the residuals between the propagated final state and raw GPS measurement, a recommendation will be made on the data input size and filter settings. Moreover, three datasets have been used to check the solution's robustness. Prior to the robustness analysis, the filter parameters, presented in section 3.2, were adjusted with the goal of optimizing the solution. This section will mostly cover the output and resulting accuracy as function of time. It is important to note that the residuals can give an indication of the error, but do not equal the error. The standard deviation of the raw GPS is still significant, including several outliers. Nevertheless, this analysis will give a critical indication of the achievable accuracy, which is an important parameter for subsequent guidance and control.

The initial simulation utilized 12 hours of GPS fitting data and 24 hours of propagation. As GPS data is typically presented in a ECEF coordinate frame, the residuals were computed using Earth-fixed coordinates. Looking ahead, there are plans to employ Satellite Laser Ranging (SLR) for validation of the navigation system. To enable a satellite to be tracked by laser, it necessitates providing a solution with an accuracy of 40 meters, Degnan 2019. This position estimate should be provided in the form of an ephemeris file. Additionally, the ephemeris must be generated and sent to the tracking service, a process that consumes time. Consequently, the 40-meter requirement must remain valid for at least 12 hours, which justifies the SLR requirement in the subsequent figures.

When discussing the upcoming results, the primary emphasis will be placed on the residuals when the filter is active and the trends and scale of the residuals after fitting. Smaller residuals are known to directly improve propagation accuracy, as they should consistently represent the GPS noise. The results obtained from 12 hours of GPS fitting and 24 hours of propagation are presented in Figure 4.2. It can be concluded from the data that the average residuals closely align with the uncertainty inherent in the GPS measurements. The stability and accuracy of the force model and final state estimate can be assessed by examining the propagated solution. In general, a stable solution was achieved, with the Root Mean Square Error (RMSE) staying below the 40-meter requirement for at least 9 hours. To delve into the cause of the oscillations depicted in Figure 4.2, it becomes clear that in all three axes, oscillations are gaining momentum. To gain a better understanding of the reasons behind these oscillations, the following figures are presented in the local VNB frame.

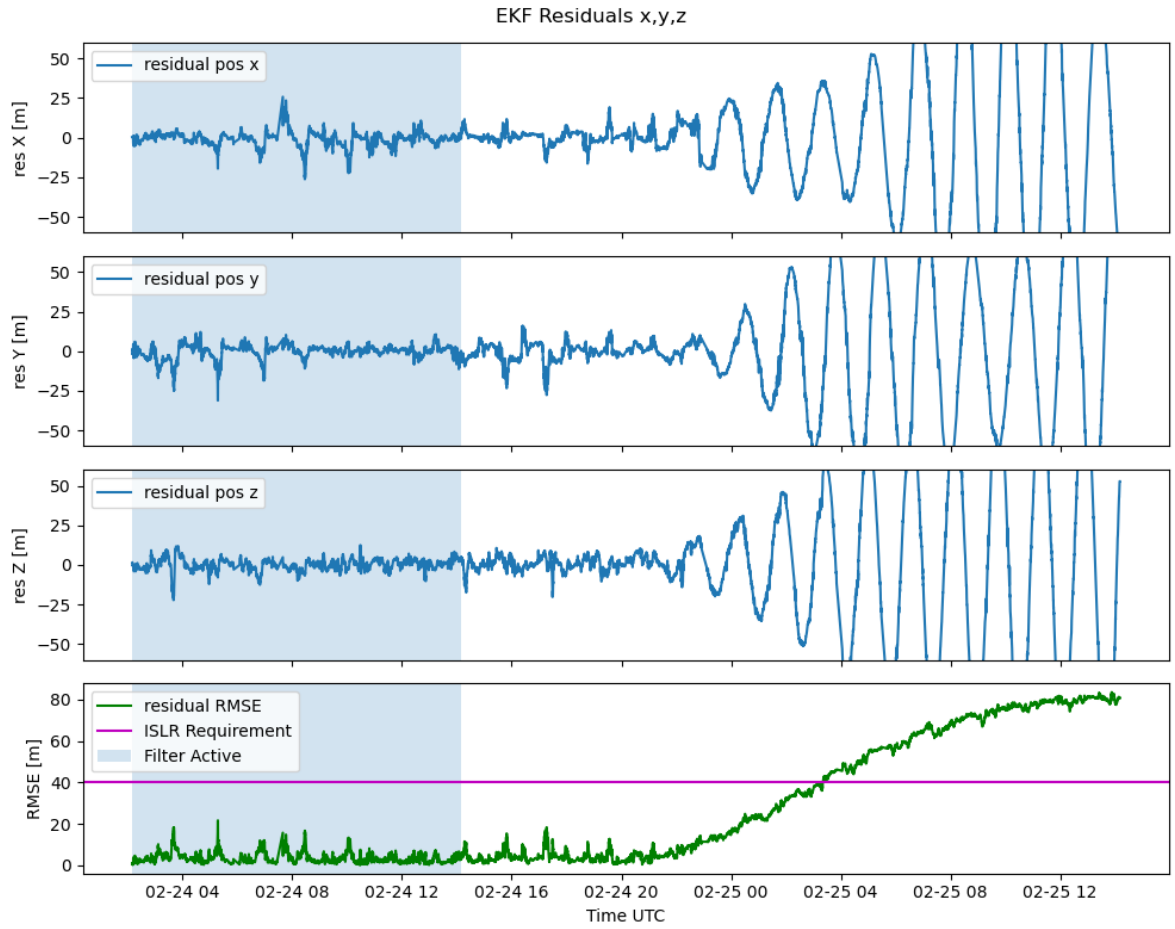

Figure 4.2: Residuals of 12 hrs EKF fitting and 24 hrs propagation in ECEF coordinates.

Upon converting the coordinate frame from ECEF to VNB, a significant observation comes to light. In Figure 4.3, it becomes evident that the propagated solution exhibits drift in the along-track direction. This drift is primarily attributed to the errors in drag modeling. While the radial and cross-track errors exhibit relatively constant oscillations, typically in the range of 10-20 meters, the along-track drift leads to a substantial deviation of approximately 150 meters when compared to the raw GPS measurements.

Numerous tests, including model adjustments and filter parameter variations, have been conducted to pinpoint the source of this drift. The findings consistently indicate a strong correlation between the drift and the estimation of atmospheric density. The challenge of accurately estimating atmospheric conditions is a well-known hurdle in precise orbit propagation. Tests involving different density scaling and filter configurations have demonstrated that the accuracy of the EKF filter and subsequent propagation is predominantly contingent on drag estimation. This adaptability allows the filter to provide a robust solution for the given dataset, closely matching the provided GPS points. However, it comes at the expense of reduced long-term accuracy.

The navigation solution strives to strike a balance between robustness and error control within specified limits. For the mission scenario outlined in Chapter 1, the system is capable of delivering accurate orbit determination for 1-3 hours, as evident from the data analysis.

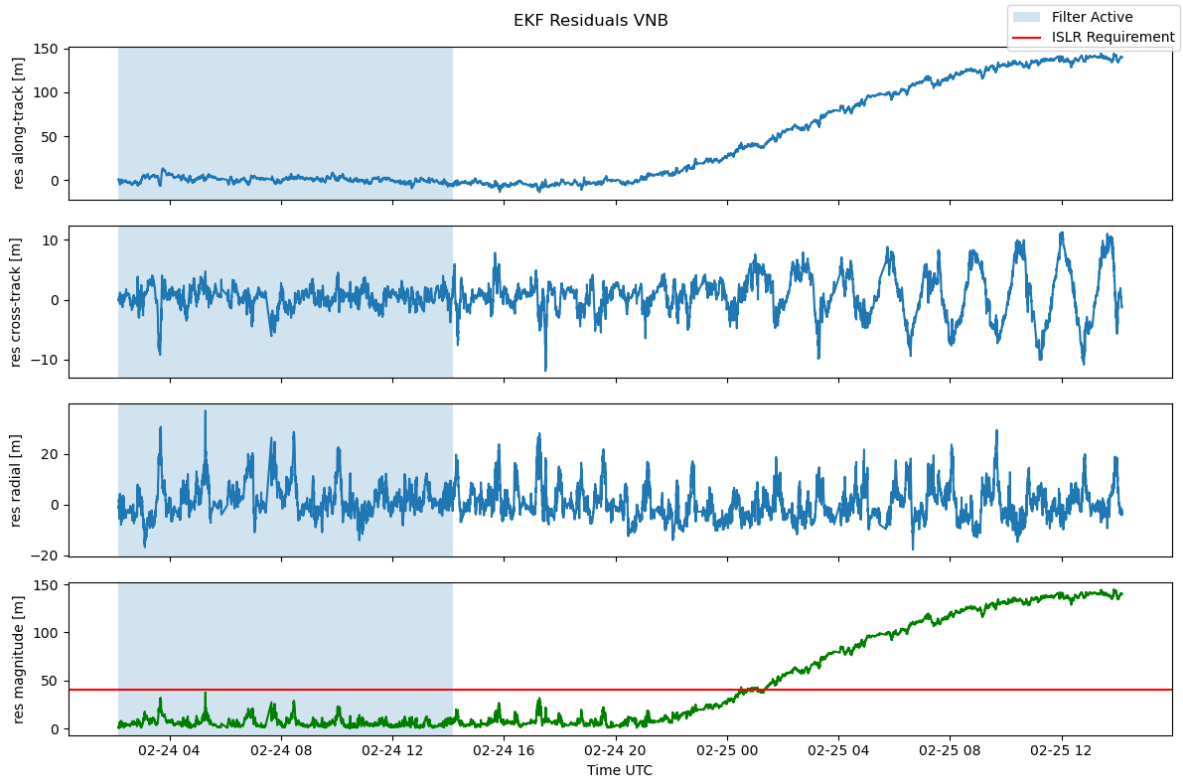

Figure 4.3: Residuals of 12 hrs EKF fitting and 24 hrs propagation in VNB coordinates.

Efforts to enhance computational efficiency and reduce the demand for GPS data prompted an investigation into decreasing the filter duration. This analysis involved fitting periods ranging from 3 to 12 hours. The primary goal of reducing the estimation duration was to enhance the overall efficiency of the navigation filter. A shorter orbit determination duration results in a reduced requirement for GPS data, facilitating faster data retrieval from the satellite. Furthermore, the EKF is fitted with a smaller volume of data during this reduced timeframe, leading to a decrease in computation time. This reduction in computation time was examined alongside considerations of accuracy and stability.

The impact of reducing the GPS fitting duration was immediately evident when analyzing the reference dataset, as depicted in Figure 4.4. A 3-hour fitted solution demonstrated a long-term stable trajectory while achieving the required accuracy. This result was unexpected, as the dataset with only 3 hours of GPS fitting exhibited remarkable long-term accuracy.

Furthermore, reducing the fitting duration from 12 to 3 hours, reduced the navigation computation time, from 96.637 seconds to 75.210 seconds. These findings suggest that reducing the duration of GPS fittings can lead to a more efficient solution that is accurate enough for certain scenarios.

However, it is crucial to note that the solution generated using 3 hours of fitting is not robust for the other two datasets. In these cases, the residuals at the end of the 24-hour propagation exceeded 1 km, and in the worst-case scenario, the required accuracy was exceeded after only 1 hour of propagation. In conclusion, while reducing the GPS fitting duration can enhance efficiency, it results in a less robust navigation solution, offering a maximum reduction of 22%. Given that the entire GNC process should ideally fit within one orbit, a reduction of 21.43 seconds in computation time does not justify the decreased solution robustness.

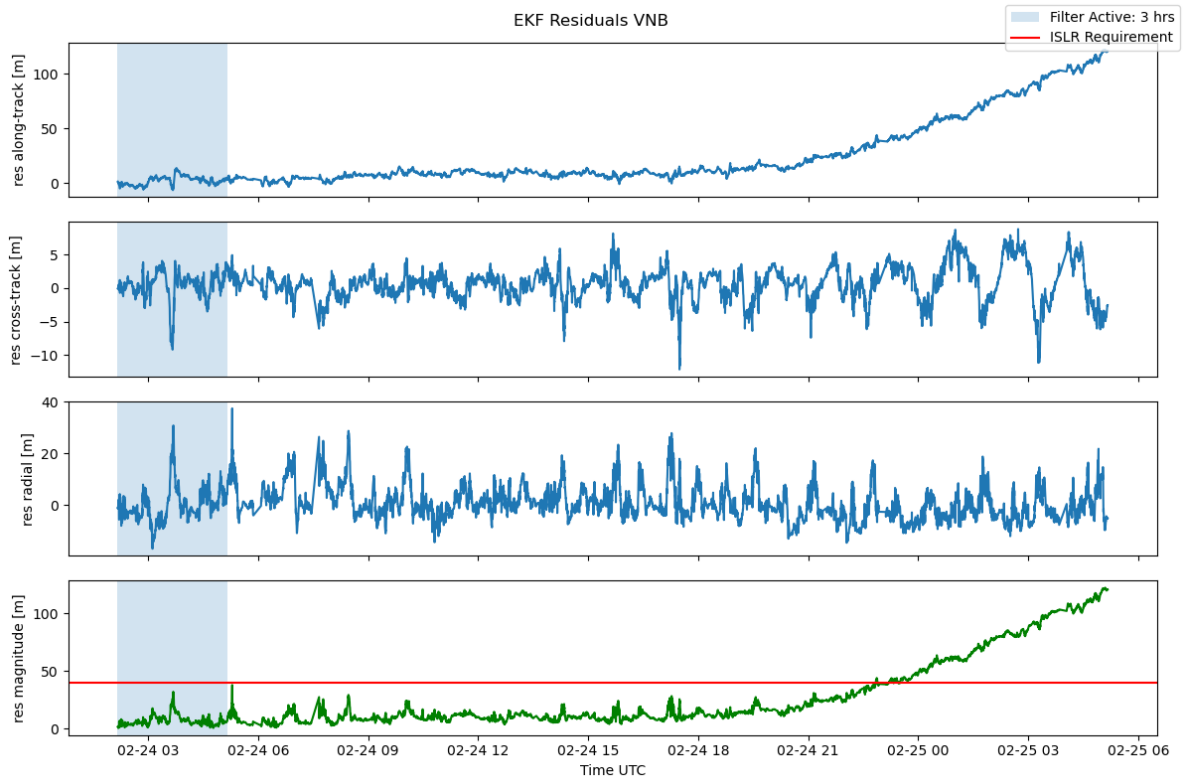

Figure 4.4: Residuals of 3 hrs EKF fitting and 24 hrs propagation in VNB coordinates.

5

Problem B: Formation with Two Satellites

In the coming simulations, the dynamics of a chief and deputy are propagated using non-linear dynamics described in Chapter 3. RSV are used to propagate the solution of the chief and the position and velocity of the deputy are propagated in the LVLH frame. These simulations account for J_2 and atmospheric drag and focussed on formation maintenance of the deputy in a GCO using a nonlinear SMC. The stability and efficiency of the controller will be analyzed within this chapter.

5.1. Large GCO Maneuver

In the following section, the ability of different thruster implementations for reconfiguring a formation are analyzed. Three different thruster implementation will be discussed; a variable thruster, a bounded variable thruster and a thruster with constant thrust. The reconfiguration of the formation requires the deputy to change from a 1.49 km GCO to a 1 km GCO formation and is matched with the research done on the SMC by Liu and Hexi 2006. In their paper, it was demonstrated that a SMC was able to reconfigure a formation using nonlinear dynamics and a nonlinear SMC. The initial conditions for this simulation have been matched with the condition mentioned in the paper. However, the actual thruster characteristics have not been mentioned, therefore, an estimation was made using the plotted thrust acceleration. The goal of this simulation is to check the performance of the SMC for large maneuvers using different thruster implementations.

To ensure sufficient data points for the controller, a propagation step size of 1 second is used. For a 1-second step size, a 1-meter model error after 24hr of propagation is introduced with respect to GMAT simulations. This error is obtained in the relative coordinate system. The error for the chief dynamics are one order of magnitude lower. Since the primary focus of the current simulation is the investigation of formation stability of different thruster implementation, the 1-meter model error is accepted. Additionally, this simulation did not include atmospheric drag for the reason that excluding drag reduced the computational effort and its effect to final controller input is changed by only a few μm. All large maneuver simulation were termination by a time constraint. Matching the simulation presented by Liu and Hexi 2006, a termination time of 6000 seconds was implemented.

5.1.1. GCO with Variable Thrust

The first simulation was performed using a variable thruster with a maximum thrust acceleration of 0.06859 m/s^2. This number was attained by using the controller input presented by Liu and Hexi 2006. Since the simulation closely represents the simulation from Liu and Hexi 2006, it is expected that the SMC is able to generate a control profile resulting in a stable formation with a tracking error in the meter level. The benefits of performing this simulation are that it will show both the validity of the controller implementation, and it can be used to explore the limitations of the controller.

The results from the maneuver can be obtained in Figure 5.3, Figure 5.2, and Figure 5.1. Firstly, the

control acceleration seen in Figure 5.1 shows a peak acceleration at the start, after which the control damps the motion, matching the position and velocity of the guided formation. From analysis of the control input, it had become clear this peak acceleration was initiated to match the acceleration of the guided formation. The guidance solution used is a GCO formation that spans three axes, therefore the controller output seen in Figure 5.1 is active for three axis in the LVLH frame. From the tracking error seen in Figure 5.2 it can be seen that the stable convergence of the error is possible and that the reconfiguration reaches a tracking error of around 1-2 meters. As the errors decrease, the control acceleration reduces which allows for fine correction leading to an ideally zero tracking error. In the next section, the satellite is equipped with a real thruster.

From the tracking error depicted in Figure 5.2, it becomes evident that stable convergence of the error is reached. The reconfiguration process leads to a tracking error of approximately 1-2 meters. As the errors decrease, the control acceleration decreases, enabling fine corrections that ideally result in a tracking error of zero. In the subsequent section, the satellite is equipped with an actual thruster and the ability of the SMC to converge to zero is discussed.

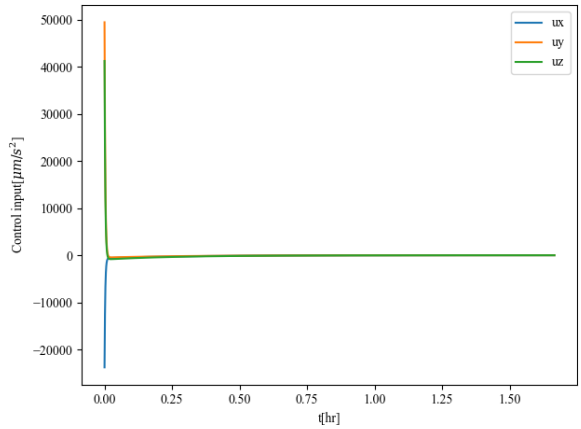

Figure 5.1: Controller input acceleration for a large reconfiguration maneuver with variable thruster.

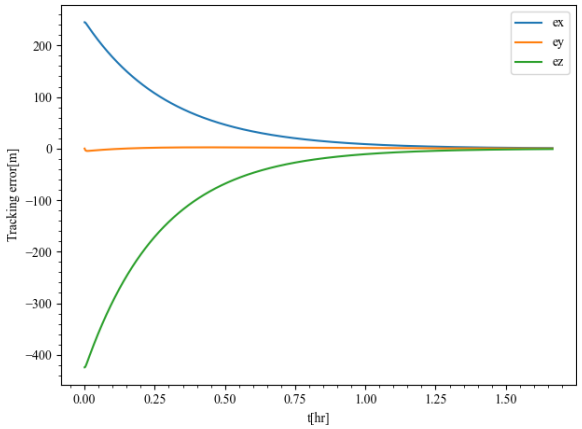

Figure 5.2: Tracking error for a large reconfiguration maneuver with variable thruster.

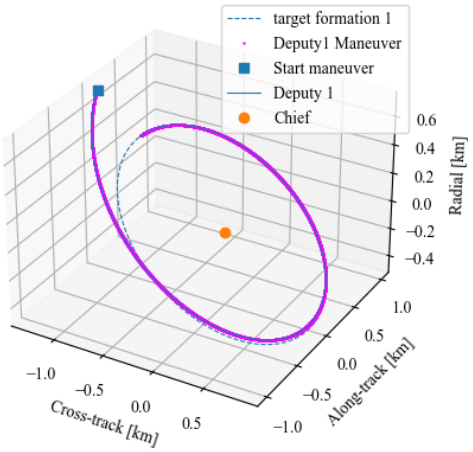

Figure 5.3: Deputy Trajectory for a large reconfiguration maneuver with variable thruster.

5.1.2. GCO with Thrust Range Settings

In an attempt to simulate a more realistic thruster behavior, this section assesses the controller's capability to execute a substantial reconfiguration maneuver. As mentioned earlier, the chosen engine allows for continuous thrust variation within a defined range. Specifically, the low-thrust engine can con-

tinuously adjust its thruster within the range of $50\mu N$ to $330\mu N$. Following the thruster implementation methodology outlined for a variable thruster in Chapter 3, the subsequent results were obtained.

For comprehensive analysis, this section includes the control input, tracking errors, and trajectory. As depicted in Figure 5.5, it is evident that the controller struggled to reduce the tracking errors. Surprisingly, the controller input, as shown in Figure 5.4, does not exhibit any anomalies, yet convergence remains elusive. This lack of convergence may be attributed to the reduction in control effort, potentially leading to instability in the controller. The drift observed in the along-track direction could be caused by the coupling between radial and along-track motion. Throughout the simulation, various settings were adjusted to assess the controller's convergence capabilities. Unfortunately, these adjustments failed to yield a stable solution.

Following the analysis of the ranging thruster, it is evident that the SMC coupled with the chosen relative dynamics was ineffective for large reconfiguration maneuvers. The optimization of the algorithm and the maximum allowable controller error for convergence are discussed in section 5.3. Additionally, the trajectory, illustrated in Figure 5.3, indicates that the deputy remains within a stable relative orbit, but the controller's contribution falls short of achieving the desired formation.

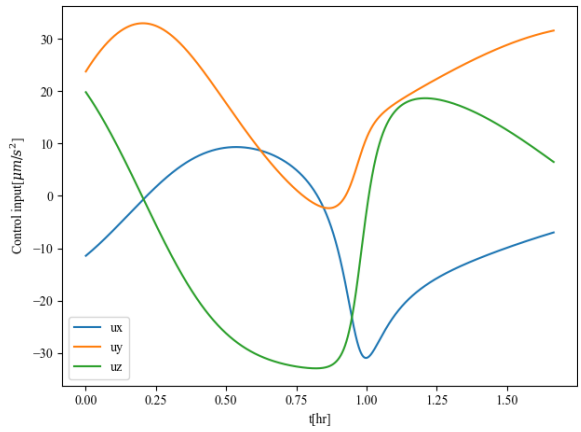

Figure 5.4: Control input acceleration for a large reconfiguration maneuver with ranging thrust.

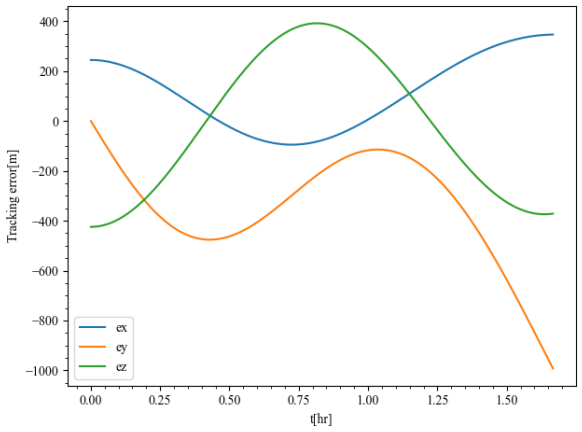

Figure 5.5: Tracking error for a large reconfiguration maneuver with ranging thrust.

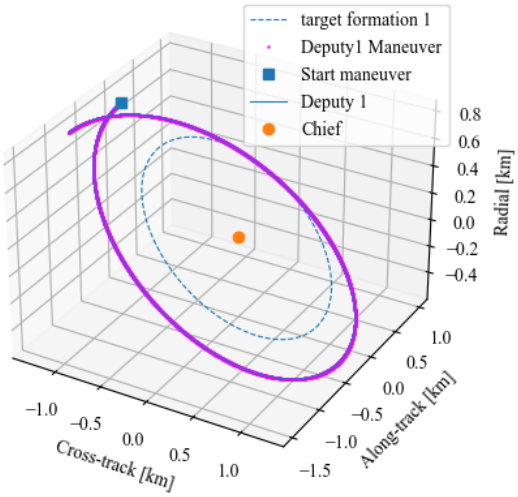

Figure 5.6: Deputy Trajectory for a large reconfiguration maneuver with ranging thrust.

5.1.3. GCO with Constant Thrust

In this section, an analysis of the SMC's performance with a constant thruster setting will be conducted. From a mission perspective, the ability to adjust the thrust levels during an ongoing maneuver may not always be feasible. Therefore, the evaluation focuses on the current controller implementation using a fixed low-thrust of $330\ \mu N$. Employing a similar strategy as discussed in the previous section, the limitations of the controller are explored. It is anticipated that using a fixed thruster will yield less favorable results compared to a ranging thruster. Considering the methodology used to integrate the thruster into the SMC, the controller follows a direct approach to minimize tracking errors. As the deputy approaches the target condition, the fixed thruster may lead to an unstable maneuver or initiate oscillations around the desired state.

Commencing the analysis with the controller acceleration, as depicted in Figure 5.7, the outcomes indicate that the implementation of the fixed thruster is accurate, maintaining a control input magnitude of $330\ \mu N$. However, no oscillatory motion is evident in Figure 5.7, indicating that the controller did not achieve convergence towards the desired state. This assertion is substantiated by the observation of tracking errors in Figure 5.8. Once again, an along-track drift persists, preventing the controller from achieving convergence. In reflection of the initial expectations, the results exhibit similar behavior to those obtained with a ranging thruster, as illustrated in Figure 5.9. This similarity can be attributed to the tracking error remaining too high for the thruster to throttle down to a lower setting.

In summary, the existing implementation of the SMC did not yield a stable maneuver for large reconfiguration, whether employing a ranging or fixed thruster. Adjustments to different controller parameters failed to produce a maneuver that effectively reduced tracking errors. Furthermore, the advantages of employing a ranging thruster were not evident in the data due to the controller's inability to achieve convergence. The subsequent section will delve into the examination of the SMC's behavior during small maintenance maneuvers.

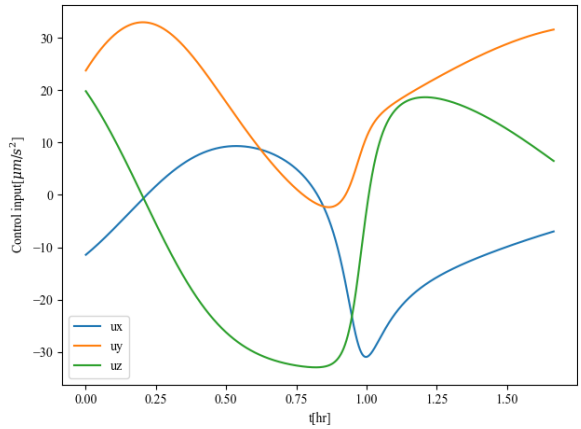

Figure 5.7: Control input acceleration for a large reconfiguration maneuver with constant thrust

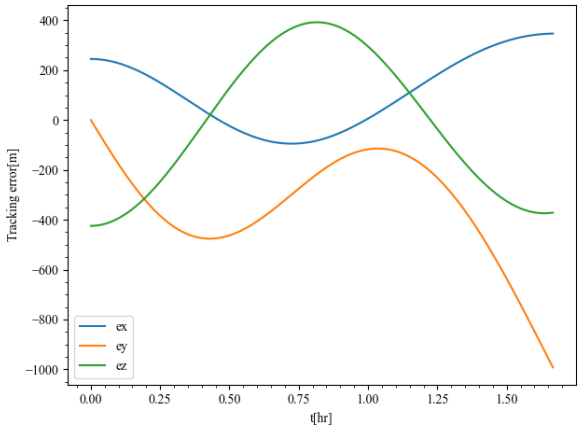

Figure 5.8: Tracking error for a large reconfiguration maneuver with constant thrust

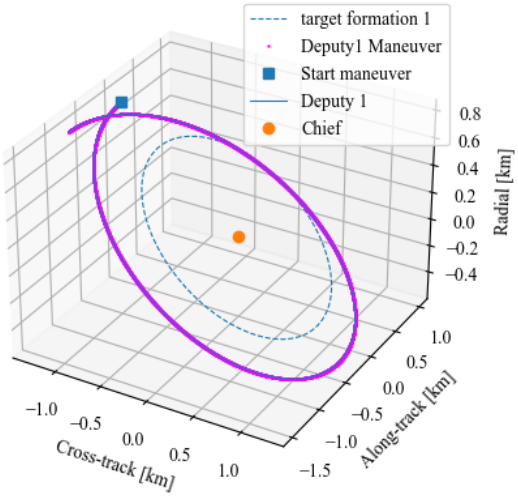

Figure 5.9: Deputy trajectory for a large reconfiguration maneuver with constant thrust

5.2. Corrective Maneuver for GCO Formation

As demonstrated in the previous section, it is evident that the SMC could not establish a stable solution when confronted with the actual engine implementation. In both cases, whether employing a ranging or fixed thrust, the tracking error remained unresolved. In this section, the aim is to explore the SMC's capacity for maintaining a formation by presenting the outcomes of small maintenance maneuvers. The forthcoming simulation is initialized with a deputy positioned 1 meter offset in all axes of the position vector. Currently, there is no inclusion of a mission planner or a first-level control law. Consequently, the controller is initiated from the offset and remains active throughout the maneuver. The primary objectives of this section are to showcase the controller's maintenance capabilities and provide insights into its convergence, which is crucial for defining the termination condition. Nonetheless, the termination condition will be addressed in the subsequent section.

Thruster with Thrust Range Implementation To start, the performance of the SMC using a ranging thruster is analyzed. The simulation matches the conditions in subsection 5.1.2, the only difference being the initial offset. By looking at the tracking error of the deputy, it is evident that the controller is able to reduce the error over time. The end condition displayed in Figure 5.11 converges around 0.1 meter and show no instability within the algorithm. By inspecting the controller acceleration, seen in Figure 5.10, two district phases can be identified. The initial smooth phase at the beginning is a result of the interplay between acceleration and velocity matching. The second phase illustrates input acceleration that is primarily related to position and velocity matching. These insights were derived from an analysis of the individual contributions of the SMC.

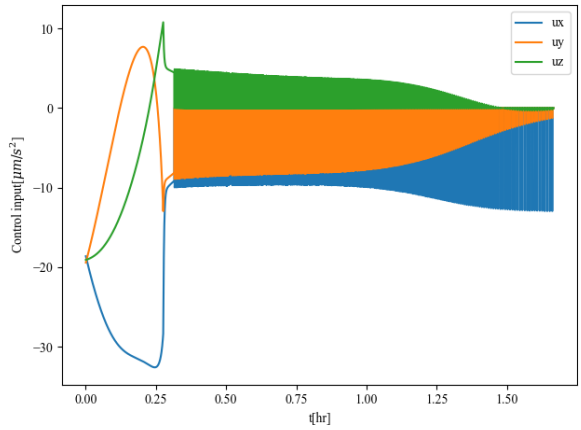

Figure 5.10: Control input accelerations for a corrective maneuver with ranging thrust

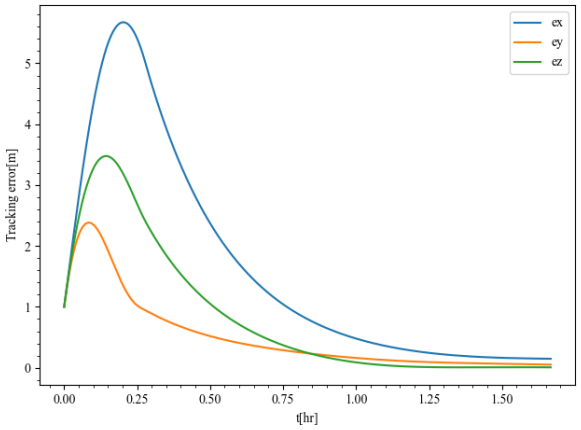

Figure 5.11: Tracking errors for a corrective maneuver with ranging thrust

Thruster with Constant Thrust To end controller analysis for different thrust implementation, the case with constant thrust is analyzed. By using an on and off switching condition, a fixed thrust of $330\mu N$ is applied. For further details on the implementation, read Equation 3.5. From Figure 5.12, it is evident that the transition of the directional flipping happens earlier than for the ranging thruster. It can be concluded that the flipping action starts at the point at which the thrust acceleration, seen in Figure 5.10, drops under the maximum thruster acceleration. Furthermore, the convergence of the tracking error does not reach the values reached by the ranging thruster. Here, a 0.3 meter radial error remains at the end of the simulation, as seen in Figure 5.13.

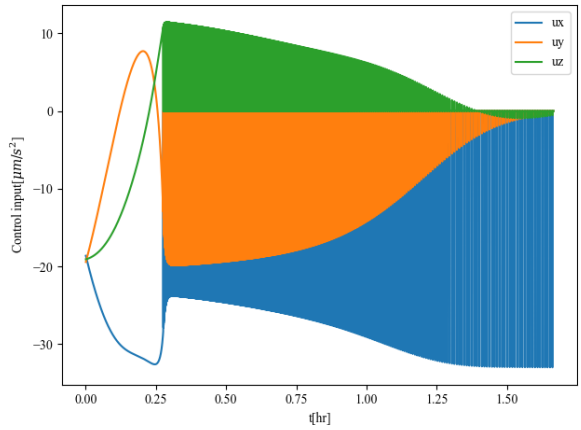

Figure 5.12: Control input acceleration for a corrective maneuver with constant thrust

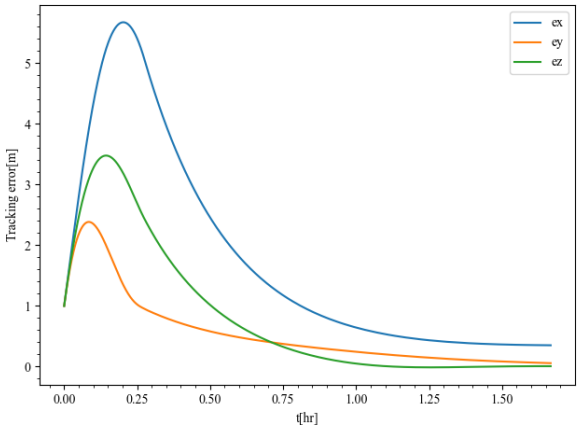

Figure 5.13: Tracking error for a corrective maneuver with constant thrust

The objective of this section was to showcase the performance of various thruster models. In summary, the variable thruster employed in the research by Liu and Hexi 2006 yielded the best results, although it is worth noting that such a thruster is not practical.. Consequently, two different thruster implementations were explored, among which the ranging thruster demonstrated the ability to achieve lower tracking errors. In the subsequent section, the simulation will be extended to encompass a more mission-like environment, incorporating the ranging thruster model.

5.3. Real Formation Mission Scenario

The reference case for the satellite formation follows a real formation mission. The chosen mission consists of two satellites that fly in formation with the aid of low-thrust propulsion. Following from the

general mission description, the satellite properties have been retrieved and are being as the reference for this simulation. It is assumed that the two satellites are identical and be tasked individually. In Chapter 4, the navigation system has been presented and discussed. For a real-mission scenario, the outcome of the navigation filter would be used as the input of the guidance and control software. This is however not the case for this part of the analysis. The goal of this simulation is to check the validity of using a SMC for a satellite formation consisting of two satellites. This will be achieved by analyzing the ability for the SMC to keep the deputy within the bounds of the guidance solutions. The reference satellites are constructed using the following variables:

Parameter	symbol	Value	Unit
Dry mass	M_0	10	kg
Fuel mass	M	500	g
Drag surface	A	0.04	m^2
Coefficient of drag	C_d	2.2	-
Minimum thrust	T_{min}	10	μN
Maximum thrust	T_{max}	330	μN
Specific impulse	I_{sp}	3000	s

Table 5.1: The satellite properties used for the simulation.

As seen in Table 5.1, the thruster has been implemented to allow for continuous variable in the thruster magnitude within the specified range. This assumption is made to reduce the controller adaptions and ease the convergence of the SMC. Without adaptations to the SMC controller, an unbounded variable thrust magnitude and direction is calculated. For avoid excessive thrust, the thrust magnitude is limited by using normalization.

Parameter	Chief
SMA	6895.45 km
ECC	0.0005 -
INC	97.48 deg
$RAAN$	271.06 deg
AOP	155.67 deg
TA	6.279 deg

Table 5.2: The initial conditions of the chief, expressed in classical orbital elements.

The initial conditions of the chief, seen in Table 5.2, have been calculated using the latest Two Line Element (TLE) to simulate the mission scenario. Additionally, the deputy is placed away from the chief by a custom offset. The desired and initial state of the deputy can be seen in Table 5.3.

Parameter	Desired LVLH state	Initial Error in LVLH state
x_j	10 km	400 m
y_j	20 km	1 m
z_j	0 km	1 m
$\dot{x}_j$	-3.782 km/s	0.01 m/s
$\dot{y}_j$	-0.318 km/s	0.01 m/s
$\dot{z}_j$	6.279 km/s	0.01 m/s

Table 5.3: The initial conditions of the Deputy 1, expressed in LVLH coordinates.

Formation The formation chosen for this simulation is the GCO which is discussed in Chapter 2. The GCO formation can be graphically visualized by an arbitrary relative orbit with a fixed radius. Both the formation radius and phase angle are design parameters. The phase angle of the deputy is measured counterclockwise from the cross-track direction, z, in the inclined plane of relative motion. A more

extensive explanation has been presented in section 3.3. The design parameters used during the simulation are given below:

Parameter	symbol	GCO specifics
radius	ρ_d	20.0 km
phase angle	ϕ	0.0°
offset reference x	x_{offset}	0.0 km
offset reference y	y_{offset}	0.0 km
offset reference z	z_{offset}	0.0 km

Table 5.4: The details of the GCO formation used by the guidance system.

The offset parameters allow the formation to be shifted away from the reference position, which is the position of the chief as can be seen in Figure 5.14. For now, the position of the reference point is kept at the chief's location.

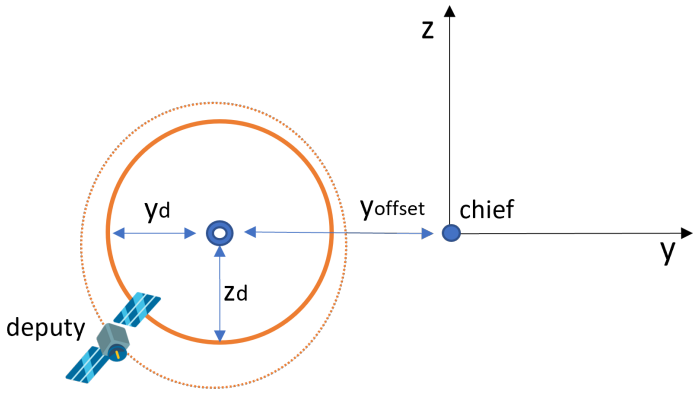

Figure 5.14: A 2D representation of the formation design parameters with a deputy in an arbitrary relative orbit.

Guidance The guidance system is responsible for providing the desired position and velocity to the controller. The current implementation of the guidance system is inspired by the set of equation provided by Clohessy and Wiltshire Clohessy and Wiltshire 1960. The CW equations have been derived by using linearized unperturbed relative motion. As a consequence of cancelling the drift in the y-axis, a set of initial conditions can be determined. Further details on the derivation can be reviewed in section 3.3. The result of this derivation can be seen below:

$$x_0 = (r_d/2)\cos\phi \tag{5.1}$$
$$y_0 = 2\dot{x}_0/n \tag{5.2}$$
$$z_0 = \pm\sqrt{3}x_0 \tag{5.3}$$
$$\dot{x}_0 = -(r_d n/2)\cdot\sin\phi \tag{5.4}$$
$$\dot{y}_0 = -2nx_0 \tag{5.5}$$
$$\dot{z}_0 = \pm\sqrt{3}\dot{x}_0 \tag{5.6}$$

The desired initial state can be retrieved from the above set of equations by selecting a desired radius and phase angle. Furthermore, these states are then propagated in time by using the state space model of the CW equation.

Termination condition To assess the controller convergence without incurring extra fuel consumption for maintaining the desired position, a termination condition is established. This condition aims to attain a highly accurate position while avoiding fuel usage due to minimal thrust settings. Although achieving a zero tracking error is desirable for formation stability, initial analyses indicate that this is

unattainable with the current thruster. As part of the result analysis, a graph illustrating the improvement in control accuracy relative to fuel expenditure is generated to determine the desired termination condition. Throughout the subsequent simulations, the termination condition remains fixed, and all simulation will be stopped according to the same criteria.

5.4. Results

Simulation Considerations The simulation set up for the real formation mission scenario uses the same settings used for the large reconfiguration and maintenance simulation. This includes the RK4 integrator with a step size of 1 second. Decreasing the time steps more did not lead to additional accuracy of the model or controller, as has been identified during the verification phase of the software. Furthermore, the guidance solution used by the controller is based on the CW equation and is linearized. The advancements in guidance dynamics will be the topic of the Chapter 5 but for now the linearized CW equation will be used to construct the guidance solution.

Nominal SMC for GCO Here, the results of a nominal SMC are presented, using the initial conditions presented in Table 5.2 and Table 5.3. The goal of the simulation is to get insight in the convergence of the tracking errors and associate thrusting angles. The controller is activated at the start epoch and is tasked to reduce the tracking errors to zero. Looking at the behavior of the SMC for a ranging thruster, it had become clear that the standard SMC with the selected ranging thruster was not capable of reconfiguring a large formation. Therefore, analyzing has been done in the cause of this inability, resulting in the following adaptations. For large formation reconfiguration maneuvers(>50 m), the control authority of the cross-track direction has been set to zero. During the analysis, it had been observed that the activation of the cross-track control authority led to an unstable control output. Thus, in order to get a stable control output, along-track drift correction has been separated from the 3D control maneuvers. In the end, the modification significantly increases the control stability.

Using the above described adaptations, the SFF software was used to propagate the dynamical system for four hours. During the full duration of the simulation, the control was active, and the deputy was tasked to maneuver itself to the desired state. The outcome of this simulation can be seen in Figure 5.15 and Figure 5.16.

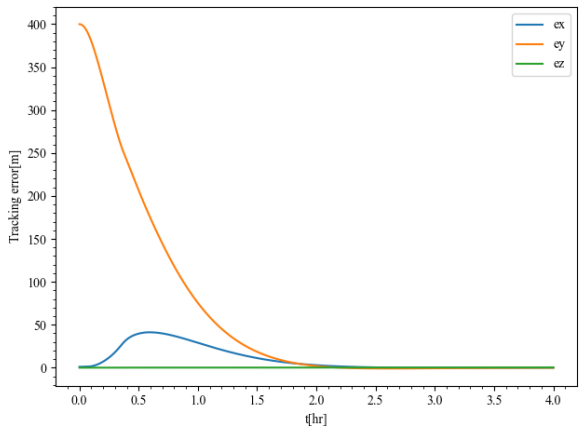

Figure 5.15: Tracking error for a reconfiguration maneuver with ranging thrust.

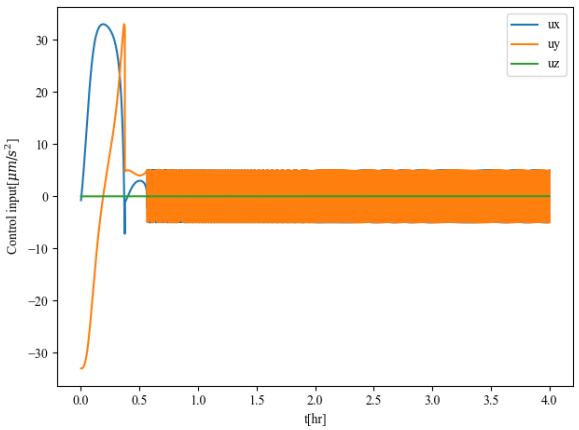

Figure 5.16: Control input for a reconfiguration maneuver with ranging thrust.

The ability to reduce the tracking errors under 1-meter is demonstrated in Figure 5.15. As a consequence of the coupling between the along-track and radial dynamics, it can be observed that the radial error increased first, after which it decreases to under the meter level. To avoid excessive fuel expenditure, it may be useful to look at the control input. From Figure 5.16, it is evident that the thrust direction become oscillatory to further reduce the errors. The data showed that by using 0.373 g of propellant, the final tracking error of 0.312 meter can be achieved. This would, however, come at the expense of a long-duration phase where the satellite has to continuously change its orientation. This is not desirable

as it would lead to reaction wheel saturation. To mitigate the reaction wheel saturation together with the excessive fuel expenditure, an additional analysis is set up that focuses on the fuel expenditure versus the added tracking performance, seen in Figure 5.17.

The capability to diminish tracking errors to less than 1 meter is aptly demonstrated in Figure 5.15. Due to the interplay between along-track and radial dynamics, it is noticeable that the radial error initially increases before subsequently decreasing to below the meter level. To prevent an excessive consumption of propellant, a closer look at the control input is warranted. Figure 5.16 reveals that the thrust direction becomes oscillatory as it endeavors to further reduce errors. The data elucidates that by expending 0.373 g of propellant, a final tracking error of 0.312 meters can be attained. However, this would entail an extended phase where the satellite continually adjusts its orientation, potentially leading to reaction wheel saturation. In light of the potential reaction wheel saturation and the associated excessive fuel consumption, an additional analysis is conducted, primarily focusing on the trade-off between fuel expenditure and the resultant enhancement in tracking performance, as depicted in Figure 5.17.

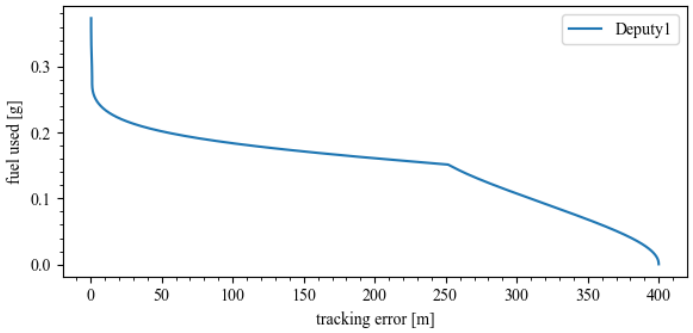

Figure 5.17: Fuel used as a function of the tracking error for a GCO reconfiguration maneuver.

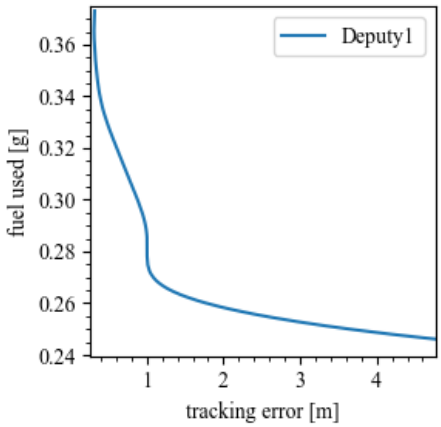

Figure 5.18: Fuel used as a function of the tracking error for a GCO reconfiguration maneuver, focussing on final tracking error regime.

Analyzing the data provided in Figure 5.17, it becomes evident that there is a point where the increase in accuracy plateaus while incurring additional fuel consumption. To determine the termination condition for the SMC, Figure 5.17 is zoomed in to focus specifically on the tracking error below 5 meters, as depicted in Figure 5.18. As indicated in Figure 5.18, diminishing the tracking error from 1 meter to the final 0.312 meter requires an additional 27% more fuel. Therefore, to reduce the demands on the Attitude Determination and Control System (ADCS) and mitigate excessive fuel consumption, the control action is terminated once a tracking error of 1 meter is achieved.

Mission Analysis By integrating the convergence criteria into the control methodology, a scenario more representative of an actual mission is constructed. Prior to conducting this simulation, an analysis was conducted to explore the controller's capability to correct along-track drift. The outcomes of this analysis demonstrated that the SMC, coupled with the selected thruster, effectively executed stable maintenance maneuvers for up to a 400-meter along-track error. To assess the controller's sensitivity in the vicinity of this point, a range of initial conditions was randomly chosen. These initial conditions were distributed within a 20-meter 3D error range, aligning with the minimum accuracy specified by the navigation filter, as detailed in Chapter 4. These accuracy requirements were derived from the BRIK2 GPS data. It is anticipated that the upcoming mission will yield a significantly enhanced navigation solution accuracy. While the 20-meter deviation may seem substantial, it contributes to the overall robustness of the system.

Over a 7-day duration, the tracking error was charted, as displayed in Figure 5.19. It becomes evident that the frequency of maneuvers is high, with the need for a maneuver arising every few hours. Two potential explanations can be proposed for this behavior. Firstly, it is possible that the GCO conditions

targeted by the SMC result in drift when propagated in a perturbed environment. Specifically, for a formation of this scale, previous research has shown that GCO formation guidance can introduce additional uncertainty, Alfriend et al. 2010. Secondly, as mentioned earlier, the SMC is terminated once a 1-meter tracking error is achieved. Consequently, a residual error remains, contributing to the overall state uncertainty.

From a mission perspective, minimizing the number of maneuvers is essential to maximize payload operation time. Figure 5.19 provides insight into the controller activation frequency during a week-long simulation, revealing that the controller is activated four times in a single day. It is important to note that the relatively high maneuvering frequency leads to the total fuel usage of 38.242 gr, meaning the formation can only be maintained for 13-weeks.

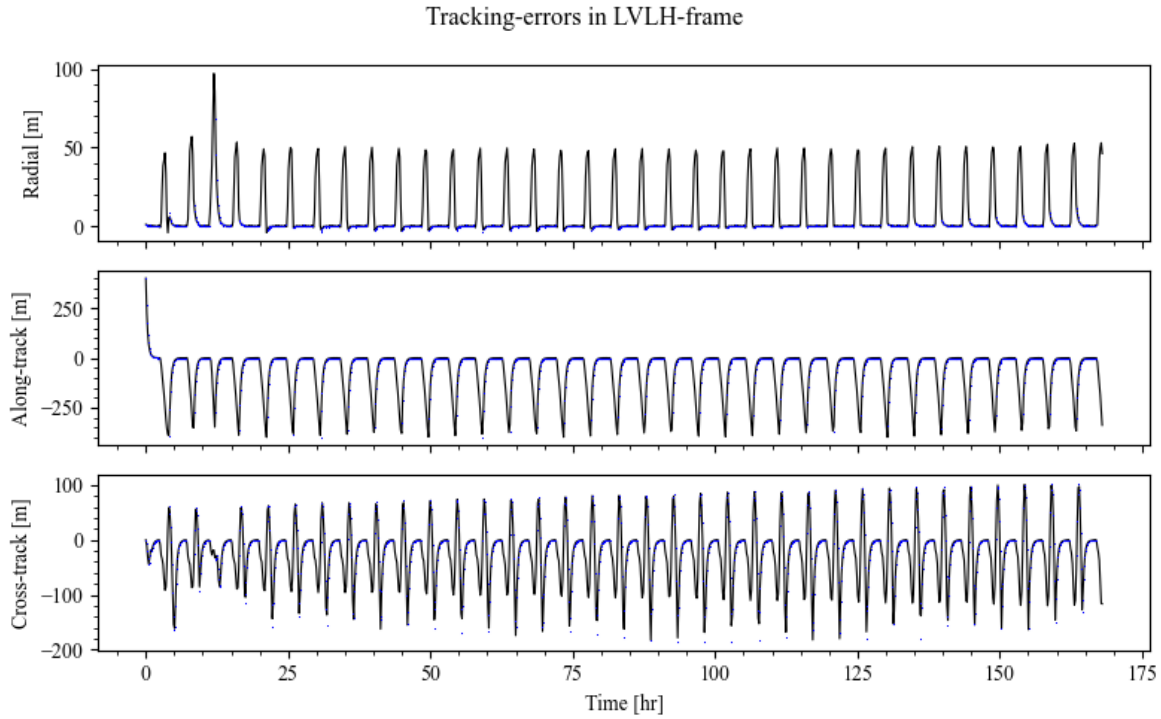

Figure 5.19: Mission analysis of a deputy in GCO with a ranging thruster. The guidance solution is generated by numerically integrating the CW equations.

To reduce the frequency of maneuvers, an alternative approach involves propagating the GCO guidance solution using perturbed nonlinear dynamics. In this scenario, the guidance solution moves along with the satellite's drift, and periodically, it is reinitialized at the center of the desired formation. This adjustment significantly reduces the number of required maneuvers. The outcomes of this simulation are presented in Figure 5.20.

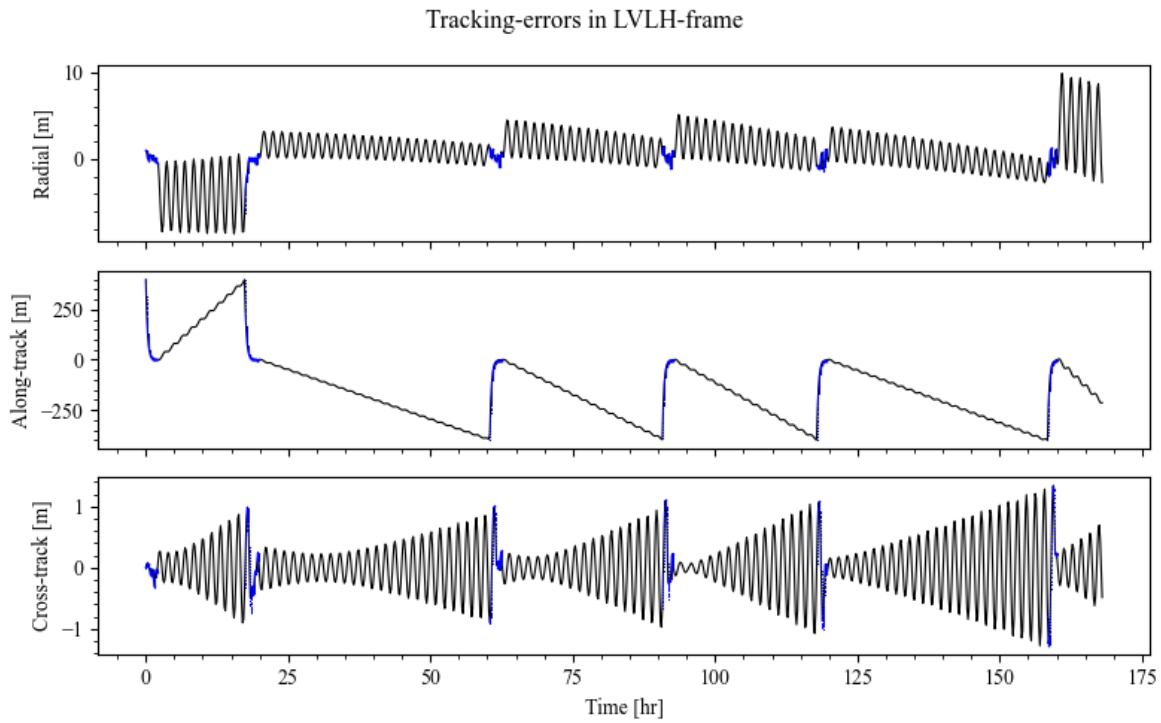

Figure 5.20: Mission analysis of a deputy in GCO with a ranging thruster. The guidance solution is generated by numerically integrating the nonlinear EOM.

This adaptation has resulted in a decrease in maneuvering frequency, but several critical notes have to be made. First, as a consequence of propagating the linearized guidance solution with a nonlinear perturbed model, the guidance solution will drift in the along-track direction and warp in the radial and cross-track direction. Additionally, the tracking errors presented in Figure 5.20 defined with respect to the perturbed guidance tracking, which results in significantly reduced error. In the end, this approach is generally unfavorable because the added guidance reconfiguration and maneuvering will eventually outreach the fuel consumption of the linearized guidance solution.

To better understand why the results from Figure 5.20 require fewer maneuvers, the guidance solution of the both simulation has been plotted in Figure 5.21 and Figure 5.22. In Figure 5.22, it becomes clear that the guidance solution is not showing drift. On the contrary, the guidance solution obtained by nonlinear perturbed dynamics does show significant drift. As has been previously said, the desired formation deviates from the actual initial desired conditions, and this has to be corrected by a larger maneuver every 2 weeks. This analysis is purely done to get insight in the problem and to get a better understanding why the GCO formation requires frequent maneuvering. In conclusion, the linearized GCO guidance solution requires frequent maneuvers when using perturbed nonlinear dynamics. To compensate for a drifting guidance solution, energy matching can be used, which is the topic of Chapter 6.

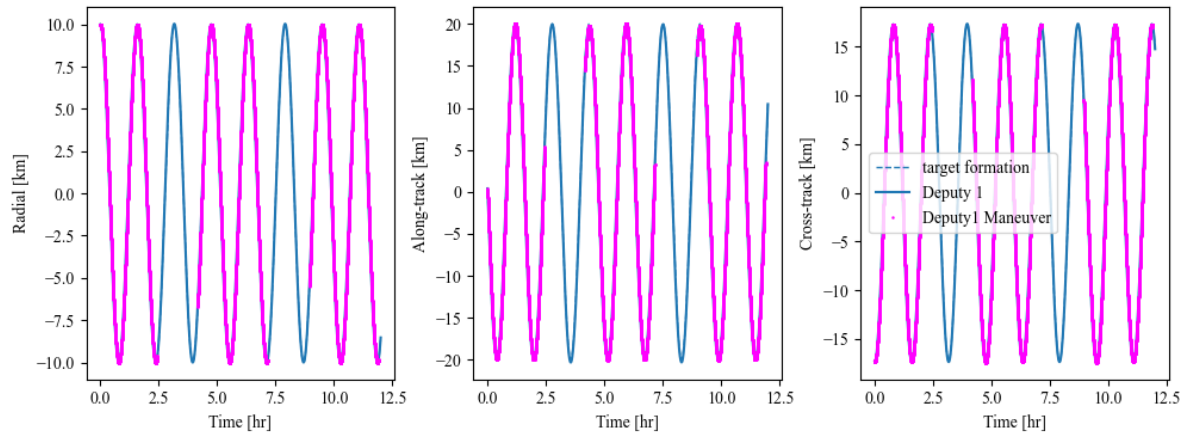

Figure 5.21: Overview of the deputy formation and guidance solution used in Figure 5.19.

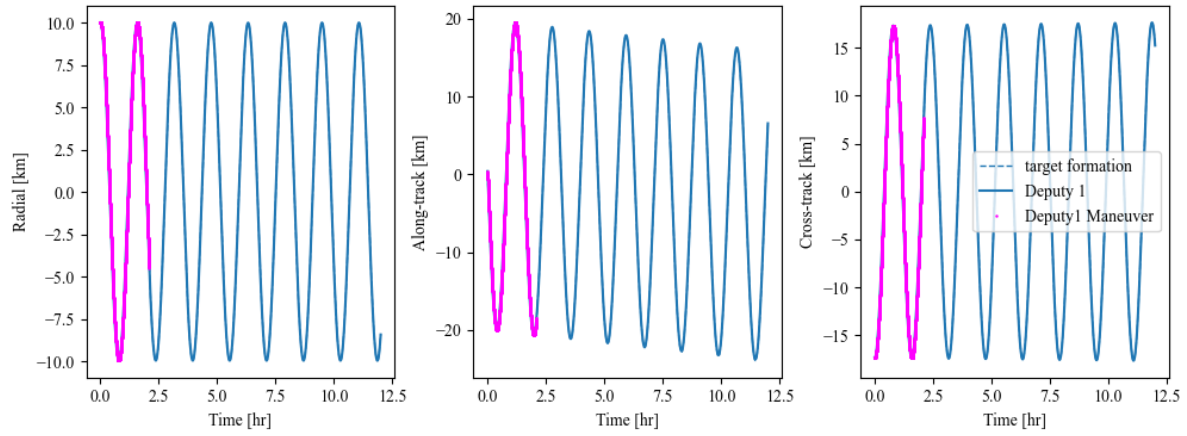

Figure 5.22: Overview of the deputy formation and guidance solution used in Figure 5.20.

In summary, the utility of a linearized guidance solution is primarily evident when utilizing linear Equations of Motion (EOM). Initially, the focus was on assessing the SMC's convergence to determine the termination condition. By combining this condition with the activation criteria, it was observed that a GCO formation could be established and maintained, while requiring maneuvers every few hours. Integrating the linearized CW approach with a nonlinear perturbed model led to a reduction in maneuvering frequency. However, it also introduced drift in the guidance solution concerning the initial GCO formation. Consequently, the conventional representation of a GCO leads to deputy drift as a consequence of linearization. Hence, new strategies need to be explored to mitigate this effect, which forms the subject of the next chapter.

6

Problem C: Guidance Exploration

Building upon the formation of two satellites discussed previously, this chapter aims to explore the guidance system within the same simulation context presented in Chapter 5. In an effort to enhance the guidance solution, energy matching is applied to the formation design, which is expected to minimize drift. This chapter will highlight the distinctions between a standard GCO and an energy-matched GCO. Subsequently, two distinct mission analyses are constructed to gain insights into the advantages of employing energy matching for various formations.

6.1. General Circular Orbit Formation

In literature, formation flying is often analyzed using GCO or PCO formations for ease of guidance implementation and constant radius, Liu and Hexi 2006 Xu and Wang 2008. The goal of this chapter is to explore a more optimal guidance strategy for formation flying. Before alternative guidance strategies can be analyzed, the GCO formation is first presented and discussed in this section. The simulation is set up using the first reference case, described in Chapter 5, which uses the initial conditions presented by Liu and Hexi 2006.

The guidance solution is derived by propagating the initial desired state vector. By configuring the formation's size and determining the desired state's position and velocity, you can obtain the specifics of the GCO formation. For a more comprehensive understanding of the implementation process, please refer to the guidance section in Chapter 3.

The GCO formation is derived from the well-established linearized CW equations, achieved by nullifying the drift in the along-track direction. However, it is worth noting that while the drift is canceled in the model, the linearization introduces errors in the desired state, ultimately causing its own form of drift. In essence, even if a satellite is initially perfectly positioned in a GCO formation, it will gradually start drifting in space due to these model-induced errors.

To illustrate this phenomenon, a simulation set-up featuring a deputy satellite positioned in a 1 km GCO formation within a perturbed environment that accounts for factors such as drag, J_2 perturbations, and nonlinearities. The simulation results can be found in Figure 6.1 and Figure 6.2.

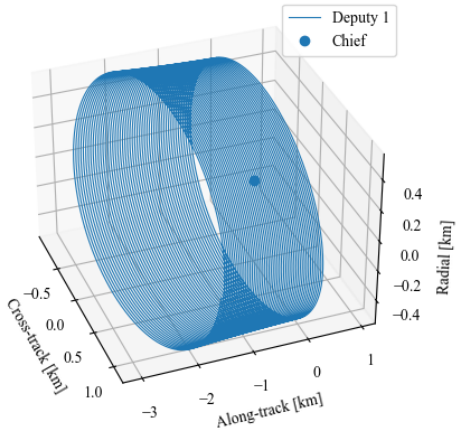

Figure 6.1: 3D trajectory of deputy deployed in a GCO formation with a 1 km radius.

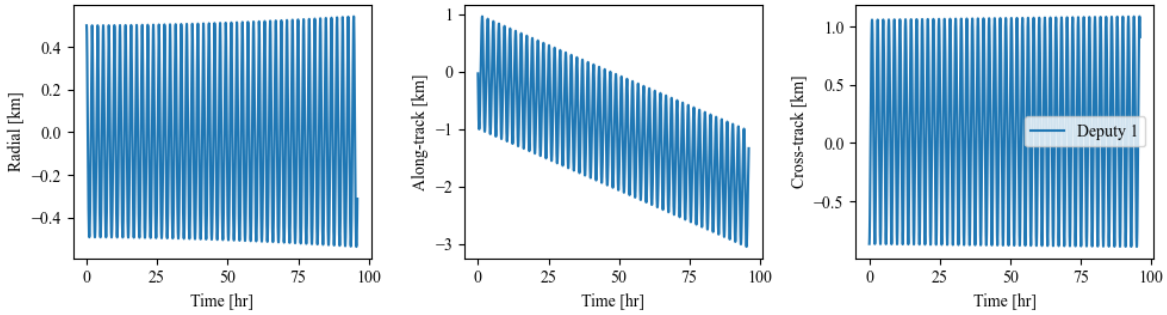

Figure 6.2: Formation as a function of time. The deployed formation is a GCO with a 1 km radius.

The deputy's 3D trajectory over time is depicted in Figure 6.1. In general, the formation remains stable in both the radial and cross-track directions. However, as previously noted, a notable drift is evident in the along-track direction. This drift becomes even more apparent when examining the formation's behavior along each of the three axes, as illustrated in Figure 6.2. It is observed that utilizing the GCO initial conditions results in a 2 km error after just 4 days of propagation. Additionally, correcting this drift would necessitate the expenditure of extra fuel resources. To minimize fuel consumption and mitigate drift, an alternative guidance strategy is explored in the following section, focusing on energy matching.

6.2. Energy Matched Formation

In an attempt to reduce fuel consumption and increase formations stability, the simulation performed in section 6.1 is repeated with the energy matching conditions. The methodology of employing an energy-matched guidance solution has been presented in subsection 3.3.2. In essence, this approach entails matching orbital momentum and energy, leading to an initial condition that encapsulates the influence of nonlinearities and J_2. The objective of this simulation is to underscore the advantages of aiming for an energy-matched GCO guidance trajectory.

From the 3D trajectory shown in Figure 6.3, it is immediately clear that the guidance solution does not show drift when propagated in a nonlinear perturbed environment. During the 4-day simulation, the formation showed stable behavior in all three axis, as seen in Figure 6.4. Whereas in Figure 6.2 showed significant 2 kilometer drift in the along-track direction and warping in the other two axes, the results in Figure 6.4 demonstrate the power of using energy matching. The use of energy matching

will be further analyzed in the following section. To conclude, the implementation of energy matching showed a stable guidance solution with minimal drift, targeting the energy-matched condition should decrease fuel consumption and control frequency.

Figure 6.3 provides a 3D trajectory that vividly illustrates the clear difference between the guidance solutions when propagated in a nonlinear perturbed environment. Notably, the guidance solution exhibits minimal drift during the 4-day simulation, contrasting with the significant 2-kilometer drift observed in Figure 6.2 for the GCO guidance solution. This stability becomes more evident when looking at Figure 6.4, which displays the formation's behavior in all three axes, showing no warping or erratic behavior, unlike the GCO solution.

The effectivity of energy matching will be explored in the subsequent section. In summary, the implementation of energy matching demonstrates a stable guidance solution with minimal drift. Targeting the energy-matched condition holds the promise of reducing fuel consumption and the frequency of control maneuvers.

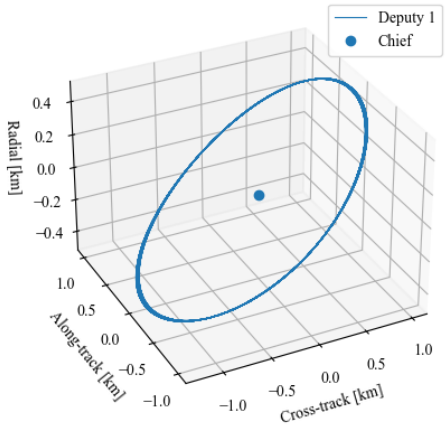

Figure 6.3: 3D trajectory of deputy deployed in a GCO formation with a 1 km radius.

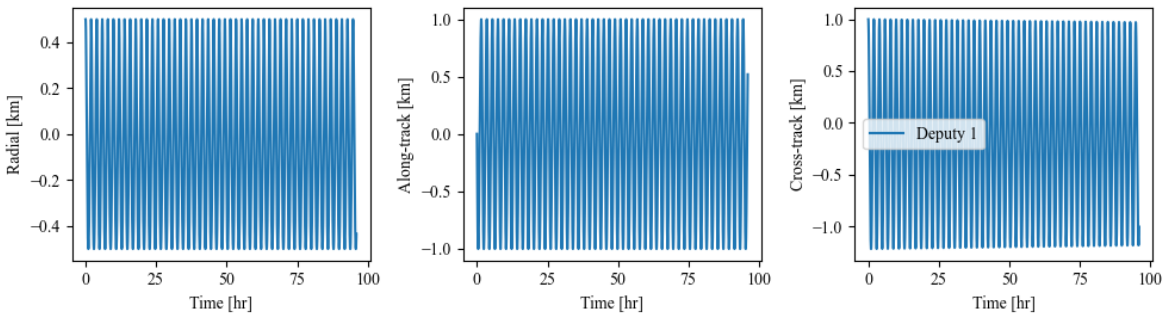

Figure 6.4: Formation as a function of time. The deployed formation is a GCO with a 1 km radius.

6.3. Mission Scenario using Energy Matching

Building upon the showcased advantages of energy matching, this section conducts a mission analysis to assess the formation's stability in a scenario that mimics an actual mission. The analysis adheres to the reference case outlined in Chapter 5. Specifically, it evaluates the performance of the guidance and control system when employing energy-matched guidance under mission-specific constraints. The

primary objective here is to gain insights into the maneuvering requirements for a system subject to mission constraints.

The findings from section 6.2 vividly illustrate the advantages of incorporating energy matching into the guidance system. These benefits become evident when using perfect initial conditions, where both the initial position is precisely known, and the thruster, along with the controller, can converge to a zero tracking error. However, it is crucial to acknowledge that the real-world scenario deviates from this assumption. As elucidated in Chapter 4, the initial position estimate at the commencement of the controller sequence is assumed to be within a 10-meter range, which is demonstrated in Chapter 8. While advancements in GPS accuracy might reduce this to 1 meter, even this marginal disparity from the true position will lead to deviations in the maneuver calculations.

Furthermore, after the simulation initiation, the controller is activated to bring down the tracking error below the 1-meter threshold. Consequently, the final state at the termination of the controller will contain a maximum error of 1 meter. Accordingly, the forthcoming simulation data is anticipated to exhibit significant drift when compared to the results portrayed in Figure 6.4.

In the forthcoming analysis, two energy-matched formations are examined: one based on GCO and the other on ATO. To begin, the results of a one-week simulation involving a deputy satellite positioned within an energy-matched GCO are presented. Similar to the simulation conducted in Chapter 5, the deputy was initially offset and controlled using a higher-order control law, as elaborated in section 5.4. Further details of these results can be found in section 5.4. The outcomes of this one-week propagation are visually represented in Figure 6.5.

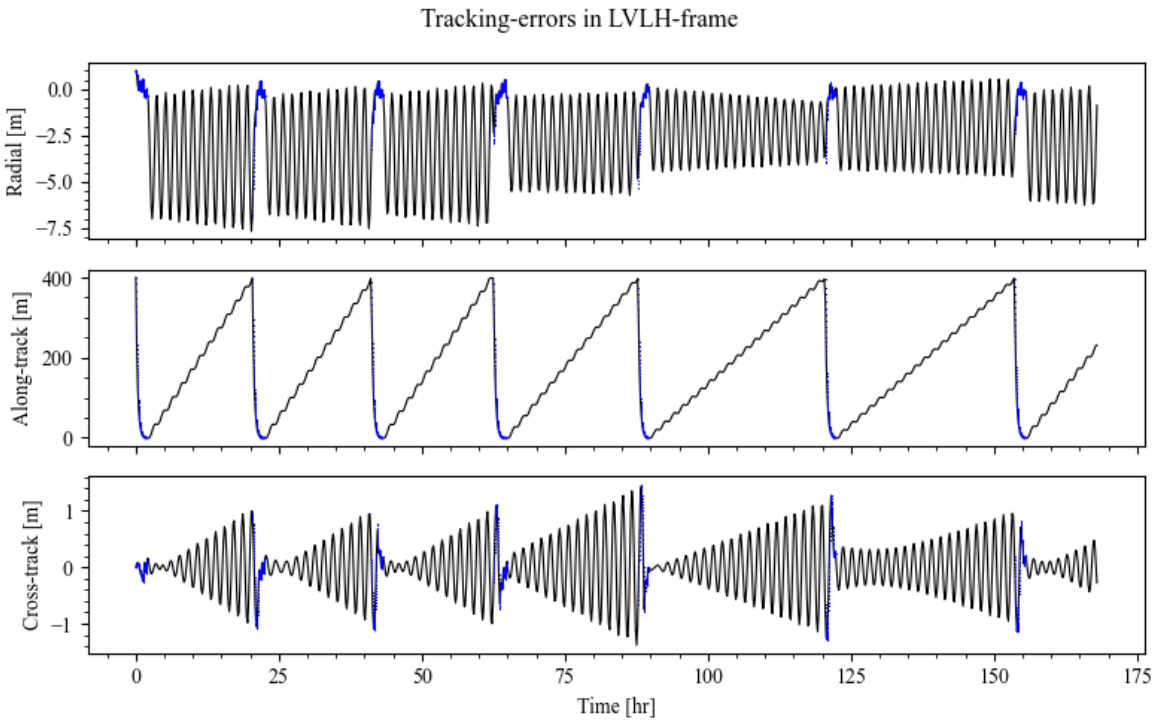

Figure 6.5: Tracking errors of an GCO formation using energy matching.

By examining the tracking error, the controller's performance in achieving an energy-matched GCO formation can be evaluated. As seen in Figure 6.5, it is evident that the state at the end of the control sequence is not zero, indicated by the noticeable drift. The blue lines in Figure 6.5 represent the sequences of maneuvers. In total, a series of 7 maneuvers were required to sustain the energy-matched GCO formation. The majority of these maneuvers were initiated due to errors in the along-track direction.

It is important to note that the controller's ability to reduce tracking errors to zero is closely tied to the

choice of the controller and thruster. However, altering the thruster is beyond the scope of this thesis, and complex optimization is not within its purview. Over the course of one week, a total of 3.184 gr propellant was consumed to achieve a delta-V of 9.369 m/s and maintain the GCO formation. This is significantly lower than the 38.242 gr used for the CW guided GCO, from Chapter 5.

Next, the maneuvering sequence is analyzed for an ATO formation, highlighting the behavior of the tracking error after the corrective maneuvers. In Figure 6.6, the tracking errors of the controller for a mission-like scenario are presented. When compared to the GCO it becomes clear that the number of maneuvers is similar to the GCO formation.

Reducing the frequency of maneuvers is advantageous in terms of payload operation and satellite control. When inspecting Figure 6.6, it is clear that the radial and cross-track drift are negligible in comparison to the along-track drift. This observation aligns with what is observed in Figure 6.5, where most maneuvers were triggered by exceeding the along-track constraint of 400 meters. The total delta-V needed during the 7-day simulation was 12.058 m/s while using 4.098 gram of propellant. Despite the higher fuel expenditure for the ATO compared to the GCO, it is still significantly less than the fuel required to maintain a CW-guided GCO, which uses 38.242 grams.

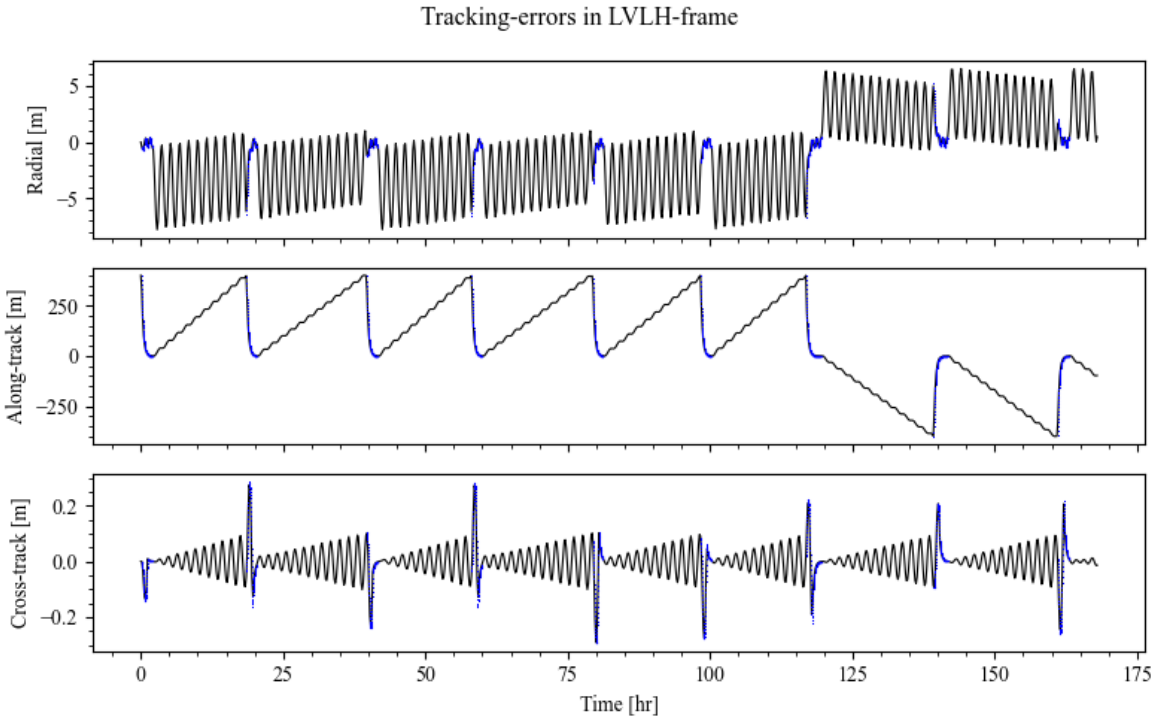

Figure 6.6: Tracking errors of an ATO formation using energy matching.

In conclusion, the energy matching condition has proven effective in reducing the number of maneuvers required for formation maintenance. Additionally, upon analyzing the behavior of the energy matching condition applied to both a GCO-inspired formation and an ATO formation, it becomes evident that the current implementation of the SMC favors the GCO formation in terms of maneuvering frequency and overall delta-V. The choice between a GCO and an ATO formation depends on the mission concept. If the specific geometric characteristics are a necessity, opting for an GCO formation with energy matching may be the best choice.

7

Problem D: Formation with Four Satellites

To address the final research question, the simulation is expanded to include four satellites, all of which will utilize energy-matched states as the foundation for their guidance solutions. To provide clarity, this chapter begins with a description of the simulation setup, followed by an exploration of the various results obtained. The primary objective of this chapter is to demonstrate the software's capability to manage a formation of four satellites and to present the maneuvering schedule for such a configuration. This chapter will end the simulation phase and is followed by the verification chapter.

7.1. Reference Case

To configure the simulation for a multi-satellite formation, the reference case outlined in section 5.3 was adopted. This reference case aligns with the real formation mission, which serves as the basis for the coming simulations [1]. Specifically, the simulation scenario involves four satellites operating in formation, propelled by the same low-thrust propulsion system.

Based on the comprehensive mission description, satellite properties have been derived, forming the fundamental basis for this simulation. It is assumed that all four satellites are identical and can each perform individual tasks. It is important to note that in a real mission scenario, the output of the navigation filter would typically be used as input for the guidance and control software. However, for the purposes of this analysis, this standard procedure has not been followed.

The primary objective of this simulation is to assess the performance of a multi-satellite formation under the control of a SMC. This evaluation will involve an analysis of the SMC to maintain the specified guidance constraints. The reference satellites are characterized by the following variables:

Parameter	symbol	Value	Unit
Dry mass	M_0	10	kg
Fuel mass	M	500	g
Drag surface	A	0.04	m^2
Coefficient of drag	C_d	2.2	-
Minimum thrust	T_{min}	10	μN
Maximum thrust	T_{max}	330	μN
Specific impulse	I_{sp}	3000	s

Table 7.1: The satellite properties used for the simulation.

As illustrated in Table 7.1, the thruster system has been incorporated to enable continuous variation in

[1] https://www.defensie.nl/actueel/nieuws/2021/01/25/nederland-lanceert-1e-militaire-nanosatelliet

thruster magnitude within the defined range. This decision has been made to minimize adjustments to the SMC controller and facilitate its convergence. Without modifications to the SMC controller, conciliatory variations in thrust magnitude and direction without gain in control accuracy would be observed.

The chief satellite is placed in a polar orbit described in Table 7.2. The initial conditions of the chief have been calculated using the latest TLE to simulate the mission scenario. It is important to note that maneuvering is limited to the deputy only.

Parameter	Chief
SMA	6895.45 km
ECC	0.0005 -
INC	97.48 deg
$RAAN$	271.06 deg
AOP	155.67 deg
TA	6.279 deg

Table 7.2: The initial conditions of the chief, expressed in classical orbital elements.

Depending on the formation under analysis, the deputies are positioned with varying initial conditions. These initial conditions are determined by applying an offset relative to the desired state, which is provided by the guidance system. It is worth noting that the offset, denoted as $\Delta\epsilon$, remains consistent for all deputies, as illustrated in Table 7.3.

Parameter	$\Delta\epsilon_{0,1}$	$\Delta\epsilon_{0,2}$	$\Delta\epsilon_{0,3}$
x_j	400 m	400 m	400 m
y_j	1 m	1 m	1 m
z_j	1 m	1 m	1 m
$\dot{x}_j$	0.01 m/s	0.01 m/s	0.01 m/s
$\dot{y}_j$	0.01 m/s	0.01 m/s	0.01 m/s
$\dot{z}_j$	0.01 m/s	0.01 m/s	0.01 m/s

Table 7.3: The initial conditions expressed in LVLH coordinates of the deputy 1,2 and 3.

Formation This chapter delves into the performance and implementation of the SMC for controlling three deputies. The formations subjected to analysis are the GCO and ATO formations, with adaptations to create energy-matched solutions. These formations are chosen for their distinct relative motion characteristics. The methodology for these formations has been previously outlined in Chapter 3, and single deputy simulations have been covered in Chapter 5. Additional details about the formation layout will be provided in the upcoming sections.

Constraints Apart from the constraints outlined in the methodology chapter, the addition of two satellites introduces several other safety considerations for smooth operations. Depending on the guided formation, it is imperative to maintain an inter-satellite separation of at least 5 kilometers. The maneuvering scheduler is designed to ensure that multiple satellites can operate simultaneously without encroaching into each other's safety zones. To guarantee safety, the guided paths are planned to keep a minimum 1-kilometer buffer between the predicted paths of a guided satellite and other satellites.

In the current setup, the system holds off on activating a maneuver unless it is entirely safe to do so. The simulation results demonstrate that the satellites were appropriately activated and guided throughout the mission, with no instances of collision risk. It is important to note that the constraint box is limited to a 400-meter along-track separation, which is notably small for an along-track formation. Consequently, this necessitates frequent maintenance maneuvers, but it effectively eliminates any collision risks in the process.

7.2. Results

The aim of this section is to showcase the proficiency of the guidance and control system when handling a multi-satellite formation. The chosen formation involves four satellites, with each satellite retaining its role throughout the simulation without alterations. The simulation settings remain consistent with those employed in the previous simulations conducted in section 5.3. The aim is to assess the software's capabilities by analyzing two distinct formation strategies. Please note that this section will focus on a first-order mission analysis, intended to sufficiently highlight the software's effectiveness and reliability.

7.2.1. Energy-Matched GCO - Multi-Satellite Formation

To facilitate a clear understanding of the selected formation, refer to Figure 7.1, which illustrates the layout of an energy-matched GCO consisting of four satellites. These satellites are divided into two groups: one satellite occupies the central position and acts as the chief, while the remaining satellites function as deputies. Starting with the satellite located farthest from the chief, which is designated as deputy 1, and the satellite with the smallest radius is set to be deputy 3. The initial radius for the deputy 1,2 and 3 are 20, 10 and 5 km, respectively. Due to the energy-matching condition, it is important to note that the relative orbit does not form a perfect circle. As revealed in the analysis conducted in Chapter 6, it is anticipated that the controller will maintain the multi-satellite formation in its predefined geometry through frequent maneuvers.

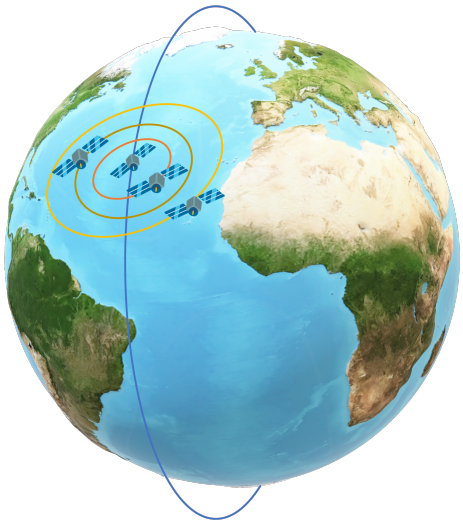

Figure 7.1: Graphical layout of the desired GCO formation. This formation has been set up using energy matching. It is important to note that the actual size of the relative trajectory is not to scale.

The simulation results are presented in Figure 7.2, and by analyzing the maneuvering frequency and tracking error, the major trends were observed. Firstly, it was expected that the maneuvering frequency would be dependent on the formation size and initial offset. While this holds true from a modeling accuracy perspective, the data depicted in Figure 7.2 reveals an interesting observation. Specifically, the middle formation, represented by deputy 2, can be maintained with the lowest amount of maneuvers. This could potentially be attributed to the manner in which the SMC is terminated, as elucidated in Chapter 5. The controller terminates when the tracking error falls below 1 meter due to the smallest thruster bit, resulting in a residual state after termination. The subsequent drift is determined by this final state. Additionally, it is evident that the largest formation, embodied by deputy 1, necessitates the highest number of maintenance maneuvers. In conclusion, the multi-satellite GCO with energy-matched conditions was successfully maintained using the nonlinear SMC.

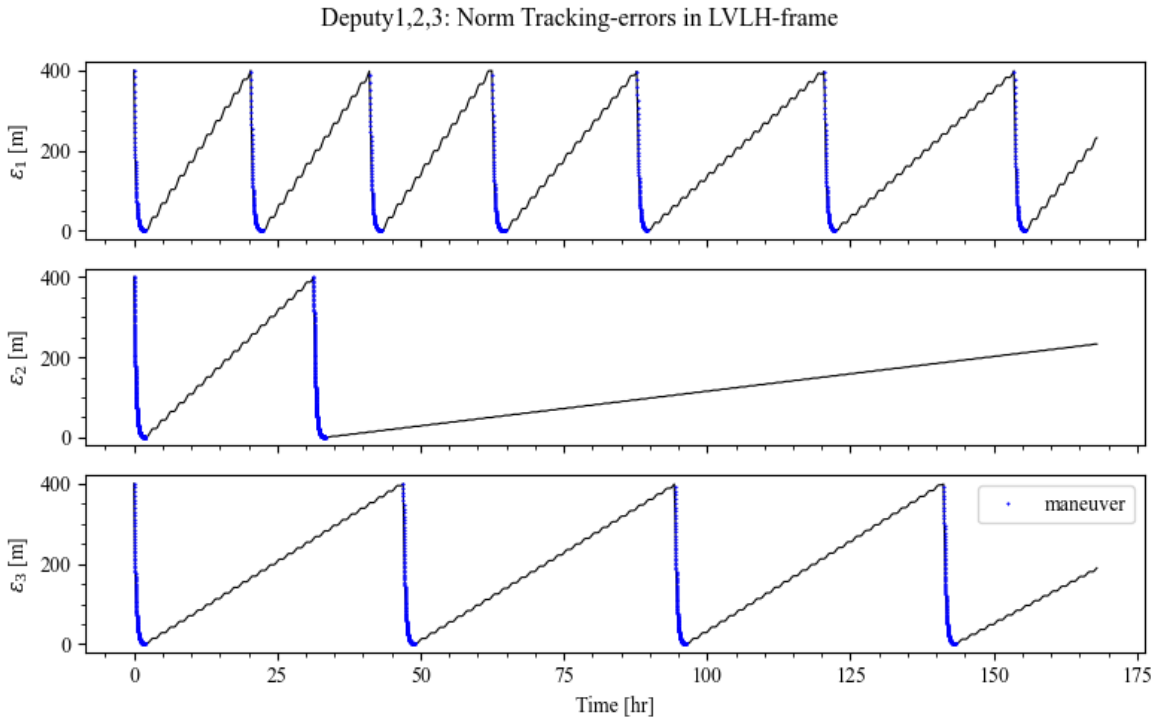

Figure 7.2: Maneuvering sequence of for a multi-satellite GCO formation that has been adopted with energy matching.

An overview of the data provided by the maneuvering scheduler are presented in Table 7.4. To summarize, the software was able to maintain an energy-matched GCO by frequent maneuvers and the tracking error did not exceed the previously mentioned constraint.

Parameter	Deputy 1	Deputy 2	Deputy 3
No. maneuvers LVLH	7	2	4
Fuel used [gr]	3.177	0.898	1.789
Delta-V needed [m/s]	9.349	2.641	5.265

Table 7.4: Maneuvering scheduler results for multi-satellite GCO formation.

7.2.2. Energy-Matched ATO - Multi-Satellite Formation

Following the analysis on the GCO, here the last simulation will be discussed. The formation used for the simulation is an ATO formation with four satellites, for which the guidance system has been adapted with energy matching. The four satellite are placed behind each other in an along track formation. Simulation performed by Alfriend et al. 2010 showed that increasing the along-track separation often leads to increased model error. As a consequence of increased differential disturbance and modelling inaccuracies, the overall numerical and modelling error grows. Therefore, it was chosen to place the deputies at an along-track distance of 20, 10, -10 km from the chief. A visual representation of the ATO can be seen obtained in Figure 7.3.

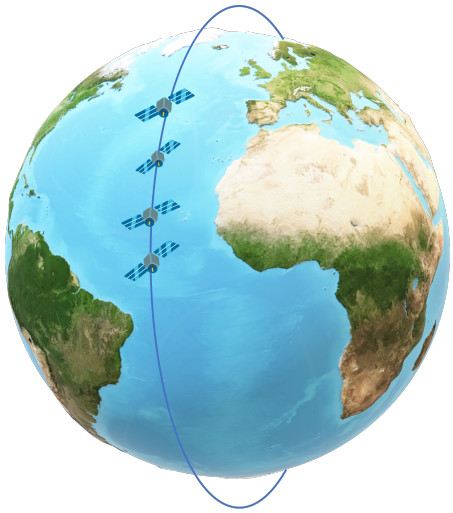

Figure 7.3: Graphical layout of the desired ATO formation. This formation has been set up using energy matching. It is important to note that the actual size of the relative trajectory is not to scale

The results of the 7-day simulation can be seen in Figure 7.4. For clarity, only the tracking error have been plotted for the individual deputies. From a first glance, it is evident that the SMC was able to maintain the formation using frequent corrections. Depending on the desired along-track separation, a difference in the number of maneuvers can be observed. For deputy 2, only 3 maneuvers were required during the 7-day simulation. Moreover, the current initial condition result towards the desired condition, which is the reason the first maneuver of deputy 2 is only needed after 78 hours from the start of the simulation. Additionally, the maintenance maneuvers take up to 3 hours and are mostly initiated due to the along-track constraint.

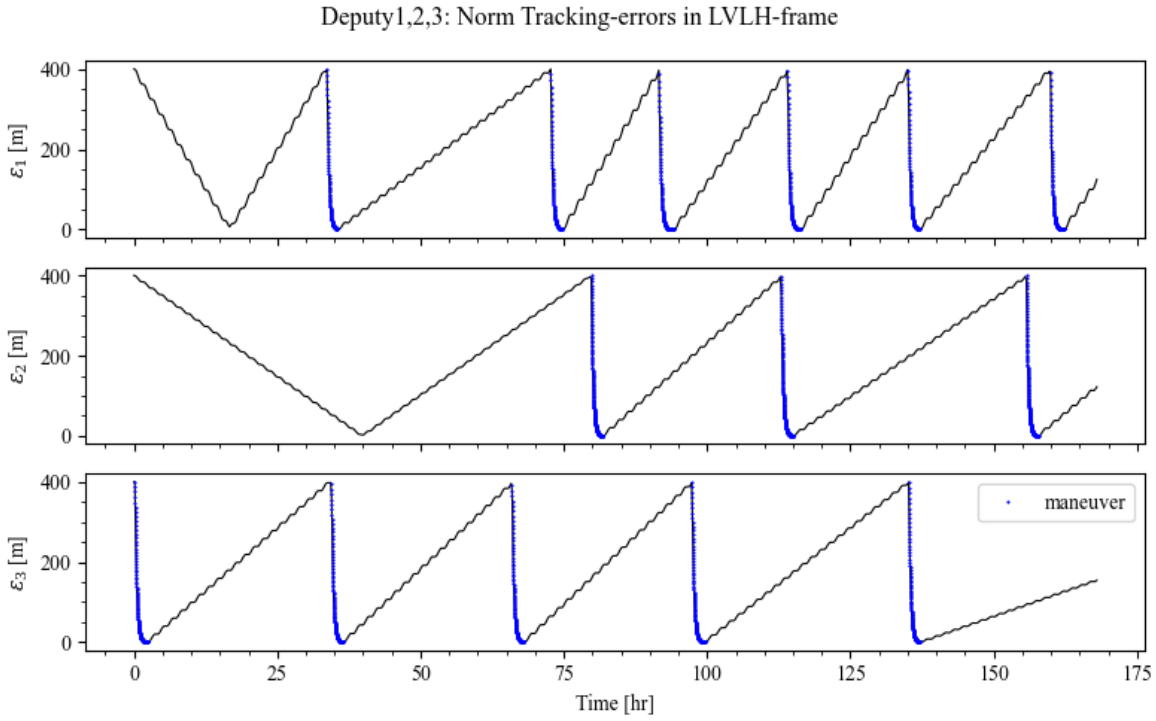

Figure 7.4: Maneuvering sequence of for a multi-satellite ATO formation that has been adopted with energy matching.

The simulation results show that the SMC was successful and was capable of maintaining the ATO formation within the mission constraint. Furthermore, the details of the maneuvering sequence can be obtained in the following table:

Parameter	Deputy 1	Deputy 2	Deputy 3
No. maneuvers LVLH	6	3	5
Fuel used [gr]	2.74	1.35	2.22
Delta-V needed [m/s]	8.053	3.965	6.626

Table 7.5: Maneuvering scheduler results for multi-satellite ATO formation.

7.2.3. Final Remarks

In this chapter, two formations have undergone analysis regarding their capability to sustain a multi-satellite configuration. It can be observed that the frequency of maintenance maneuvers varies depending on the formation type and initial conditions. However, establishing a direct correlation between formation design and maneuver frequency has proven elusive. Future research endeavors could delve into further analysis and optimization to reduce maneuver frequency and minimize fuel consumption.

Ultimately, the total required delta-V was 17.255 grams for the GCO formation and 18.644 grams for the ATO formation. The time needed to generate the 7-day simulation of 24.87 and 28.42 minutes for the GCO and ATO respectively, which is well under the calculation requirement. It is worth noting that making a definitive judgment on whether the GCO formation is more fuel-efficient than the ATO formation is contingent on several variables, including the initial offset, thruster model, and controller termination conditions. Nevertheless, it can be concluded that the current implementation of the SMC has performed commendably for both GCO and ATO formations.

For the sake of comparison, a similar formation employing different dynamics and a distinct controller resulted in a delta-V of 78 m/s, Alfriend et al. 2010. It is important to highlight that this study employed a smaller error box of only 40 meters, which necessitated more frequent maneuvers. While a direct comparison may pose challenges, this serves to underscore the potential of our current software.

In summary, while several adaptations and enhancements may be untouched, the present implementation has demonstrated itself as a reliable and versatile software solution for formation flying.

8

Verification

In the pursuit of precision and dependability within propagation of dynamics, the verification of propagators stands as an essential undertaking. Within this framework, a verification procedure is initiated, specifically focusing on a propagator operating under the influence of point mass acceleration, J_2 and drag. This thorough examination is undertaken with the primary objective of confirming the reliability and precision of the implemented dynamics. Through this rigorous verification process, the aim is to establish the solid foundation upon which accurate and dependable orbital predictions can be made.

8.1. Navigation System Verification

This verification process is a test of the filter strength. The verification of a space navigation filter involves subjecting it to rigorous examination and testing under various conditions and scenarios. The aim is to ascertain its ability to consistently produce accurate navigation solutions, regardless of the challenges posed by external factors such as gravitational perturbations, sensor noise, or atmospheric density variations. This section focuses on the verification of the one reference case. For more details on the sensitivity analysis, in Chapter 4 the effect of changing the filter variables is presented.

Through this systematic evaluation, the aim is to highlight the stability and long term accuracy of the navigation solution by using a large set of GPS measurement. This involves utilizing a substantial dataset of GPS measurements, which is then divided into two distinct sets: the first part serves as input or fitting data, while the second functions as verification data. The subsequent step involves the propagation of the final estimated state employing a high-fidelity model. This not only quantifies the accuracy of the solution but also confirms the system's robustness. The analysis of residuals between the propagated data and the raw GPS measurements plays a vital role in assessing the enduring validity of the filtered solution over an extended timeframe. This ultimate phase holds great significance as it outlines the boundaries of the navigation filter's capabilities, providing insights into achievable control accuracy and ensuring the long-term reliability of the system.

The reference case utilized for verification is detailed in Chapter 4. From a mathematical perspective, it proves more convenient to represent the residuals within the VNB frame. This conversion facilitates the separation of errors into radial, along-track, and cross-track directions. Figure 8.1 illustrates the results obtained from the reference case discussed in Chapter 4.

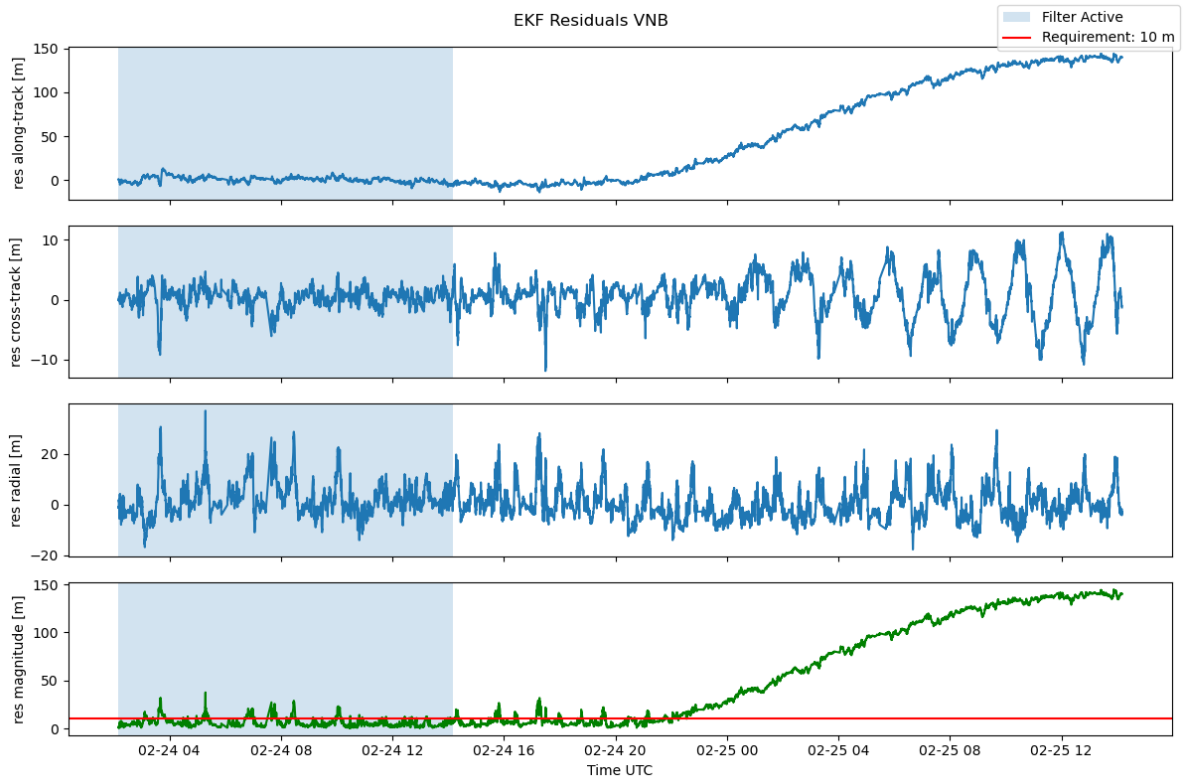

Figure 8.1: Outcome of the verification analysis for 12 hr fitting of raw GPS data, using an EKF. The first parts present the residuals obtained from fitting, whereas the residuals of the second parts are calculated by comparing the raw GPS measurement with the propagated state.

To provide context, a 10-meter requirement is displayed, is a consequence of the first-order data analysis. By observing different datasets, it was observed that the practical accuracy of the navigation filter was limited by the lack of model realness and sensor accuracy. Therefore, a custom requirement was set to be 10 meters, which is conservative. In the end, the navigation solution must be improved to further reduce the position error, but for now, the 10-meter requirement is used.

Upon examining Figure 8.1, it becomes evident that, at times during the fitting process, the residuals exceed the 10-meter threshold, indicating the presence of outliers in the GPS measurements. These outliers are also observable when inspecting the propagated data, where several peaks emerge.

However, focusing on the results presented in Figure 8.1, the 3D residuals demonstrate a stable solution within six hours following the final state estimate. This suggests that the position estimation and subsequent propagation remain valid for the required duration of 1-3 orbits. Nevertheless, it is important to acknowledge that the mean residual could not be reduced beyond 10 meters. This limitation arises from both the model itself and the characteristics of the input data, rather than any shortcomings in the EKF implementation. In summary, the navigation system is confirmed to be functional, though with a significant limitation: the attainable accuracy is restricted by factors like atmospheric modeling and GPS precision.

8.2. Software Testing

In the dynamic domain of software development, where complexity and innovation often converge, the topmost priority is to ensure the unwavering reliability and flawless functionality of a program. This is precisely where the indispensable practice of unit testing takes center stage. Unit testing is a critical methodology that involves the meticulous scrutiny of individual code components or units in isolation. It entails a methodical assessment of their accuracy and the verification of their intended functionality. The rationale behind the imperative need for unit testing is rooted in the inherent intricacies of software development, driven by the unwavering commitment to deliver robust, error-free applications.

During the development phase, a variety of unit tests were incorporated to address multiple aspects, including data input formats, coordinate transformations, and general output observations. Additionally, three verification test files were generated to rigorously validate the software's correctness under reference conditions. This meticulous testing significantly reduces the likelihood of encountering unexpected glitches, crashes, or malfunctions, thereby enhancing user satisfaction and fostering trust in the software product.

These three reference scenarios were meticulously established for testing purposes. Firstly, a scenario involving two satellites was designed to assess the propagation's performance across various existing models, such as GMAT and Tudat. This reference case allowed us to analyze the dynamics transition from a point mass gravity model to a spherical Earth.

Subsequently, a distinct scenario was formulated to validate the implementation of drag. Furthermore, we scrutinized the stability of relative dynamics and guidance by observing the formation's drift over a 96-hour period.

Lastly, the controller underwent testing in a different test case, closely resembling the original implementation. This allowed for the validation of the control strategy's effectiveness and reliability.

8.3. Propagation Test

This purpose of this section is to verify the implementation of the coordinate transformation of the initial states, propagation of the chief dynamics, transformation of the relative state, and propagation of the relative dynamics. In order to verify the chief initial state transformation and propagation, simulation data from GMAT and Tudat have been used. In order to verify the implementation of the methodology, the settings (force model and propagator) have been matched. To verify the dynamics and transformation of the deputy, only GMAT was used because the relative coordinates can be easily extracted when setting up a local frame. Note, however, the numerical accuracy between model is tested and verified and not the model accuracy as a whole. A next step in the verification can be to use a high fidelity model to quantify the effect of using a reduced force model, but this has not been analyzed within the thesis.

For the verification processing of the absolute and relative dynamics, the initial conditions presented by Xu et al. 2009 are used. Using these parameters ensures that small-scaled verification test can be performed, such as the coordinate transformation needed to get the initial state for the guidance and control system. Additionally, the energy matched conditions have been derived using this reference orbit, allowing direct comparison of the validity and stability of the energy matching implementation. The initial simulation involved utilizing the reference orbit as outlined by Xu et al. 2009. In this simulation, a deputy orbit was employed, featuring minor deviations in both Inclination (INC) and True Anomaly (TA) seen in Table 8.1 and Table 8.2.

Parameter	Symbol	Orbit
SMA	a	8000 km
ECC	e	0.1
INC	i	63.4349°
RAAN	Ω	1.0°
AOP	ω	45°
TA	ν	1.0°

Table 8.1: The reference case used for verification of the relative dynamics. The parameters have been matched with the simulation performed by Xu et al. 2009

Parameter	Symbol	Orbit
SMA	a	8000 km
ECC	e	0.1
INC	i	63.4345°
RAAN	Ω	1.0°
AOP	ω	45°
TA	ν	1.01°

Table 8.2: The deputy's orbit used for verification of the relative dynamics. The parameters have been set by adapting the chief's orbital parameters given by Xu et al. 2009

The subsequent propagation verification is employed to validate the accuracy of the dynamics implementation. By using this strategy, the implementation of the equation, integrator settings, and propagation set up can be verified. To achieve a fully verified system, the following steps are taken. First, the dynamics are reduced to represent a two-body problem. With the error of chief and deputy dynamics within the selected margin, the dynamics are upgraded to included J_2. Following up, the drag is introduced in the simulation to increase its fidelity. In the end, the goal of this section is to identify mistakes

in the model implementation and quantify the final deviation with respect to high-fidelity software such as GMAT and Tudat.

8.3.1. SFF Software with Point Mass Acceleration

Simplifying the model into a two-body problem with point mass offers enhanced opportunities to identify implementation errors and verify various facets of the integrator and propagation implementation. To achieve this, a comparative analysis is conducted using the same reference case, as presented in Table 8.1 and Table 8.1. This analysis encompassed the use of GMAT, Tudat, and our custom SFF software. The results of the relative dynamics analysis are depicted in Figure 8.2.

Upon initial observations, it becomes evident that the overall motion and trends closely align across the platforms. The plot distinctly illustrates the absence of any noticeable drift, as expected, given the absence of perturbations beyond point mass acceleration. It is worth noting that the differences are barely discernible in Figure 8.2, primarily due to the orbital elements' scale being considerably larger than the level of accuracy required.

To better visualize the deviations across the selected models, the differences have been calculated and plotted in Figure 8.3. Overall, the deviation between GMAT and the SFF software are small. For example, the max radial deviation is around $9 \cdot 10^{-}7$ meter, which is accepted since the navigation solution is required to be accurate to 10-meter. From Figure 8.3, the deviation between Tudat and the SFF software is significantly smaller than the deviation with GMAT. This can be the cause of coordinates transformation and since the error are of this order of magnitude this is not analyzed further. In the end, it can be concluded that the deviation across the different models are not showing any problems or significant error in the model implementation and propagation.

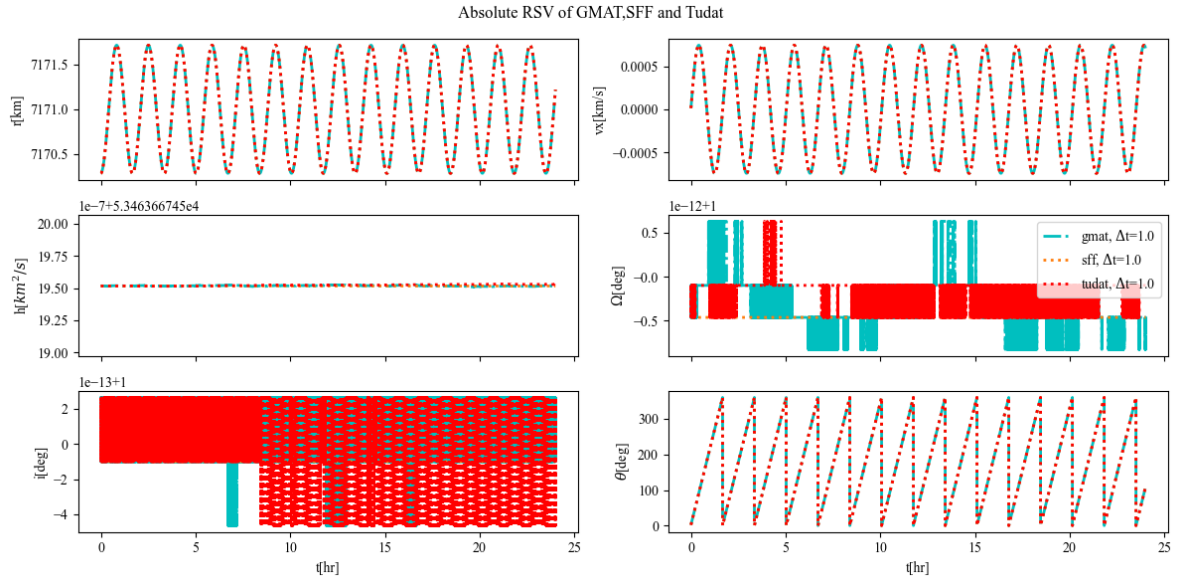

Figure 8.2: Results verification process for the absolute dynamics expressed in RSV, using the results from GMAT, Satellite Formation Flying (SFF) software, and Tudat. All simulations have been performed for a two-body problem with a fixed 1 second RK4 integrator.

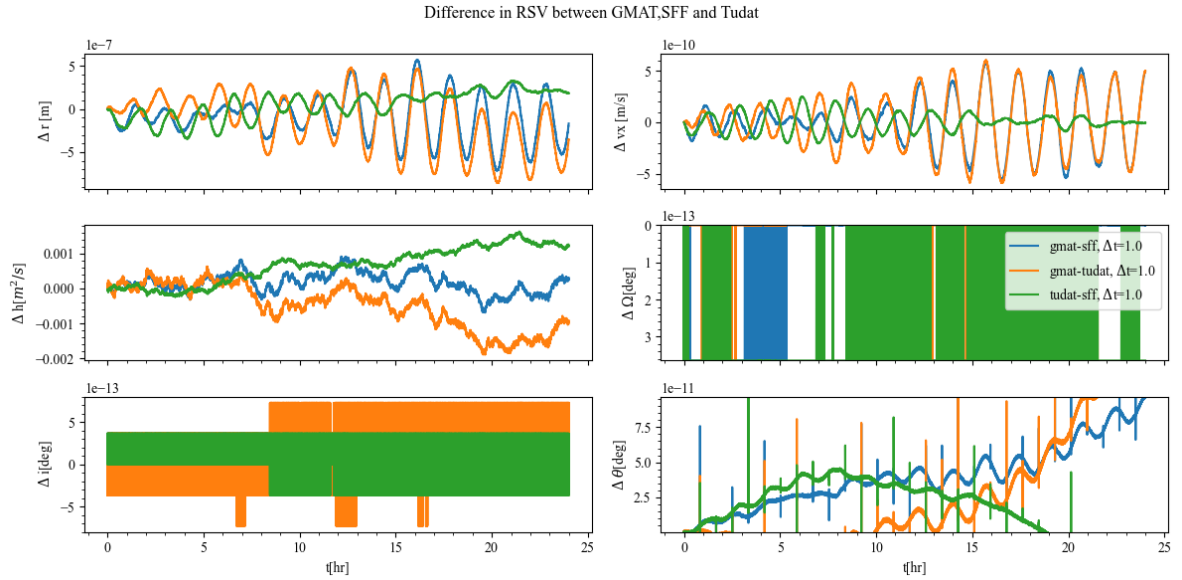

Figure 8.3: Results verification process for the absolute dynamics expressed as the difference between simulation, using the results from GMAT, Satellite Formation Flying (SFF) software, and Tudat. All simulations have been performed for a two-body problem with a fixed 1 second RK4 integrator.

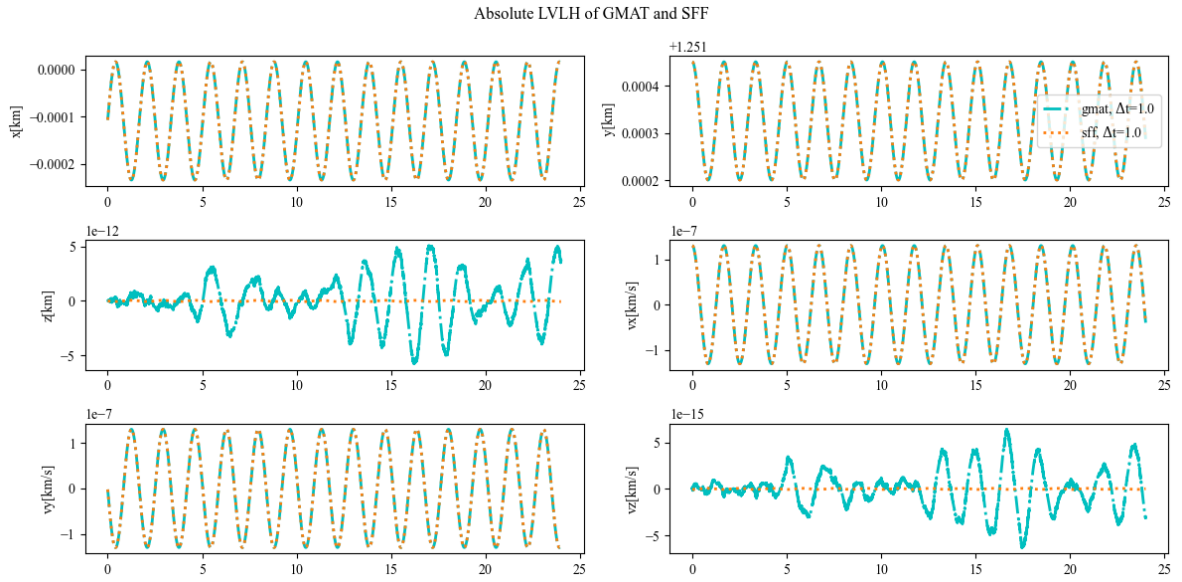

Figure 8.4: Results verification process for the relative dynamics expressed in the LVLH frame, using the results from GMAT and Satellite Formation Flying (SFF) software. All simulations have been performed for a two-body problem with a fixed 1 second RK4 integrator.

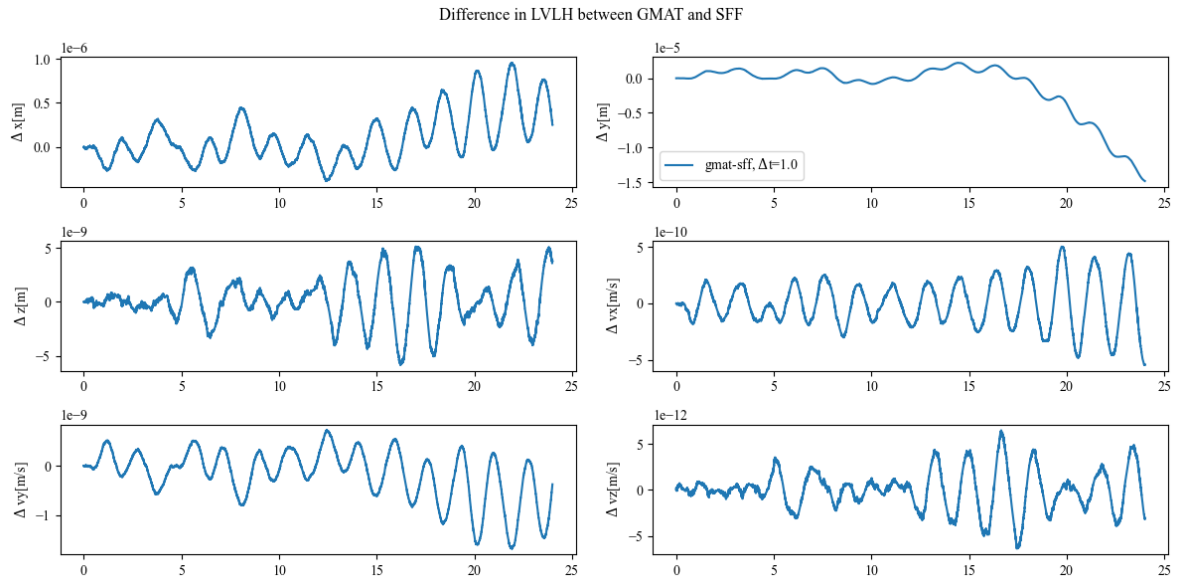

Figure 8.5: Results verification process for the absolute dynamics expressed as the difference between simulation, using the results from GMAT and Satellite Formation Flying (SFF) software. All simulations have been performed for a two-body problem with a fixed 1 second RK4 integrator.

8.3.2. SFF Software with J2

The subsequent phase involves introducing an oblate Earth instead of a spherical Earth. It is anticipated that this adjustment will result in more noticeable deviations between the models. It is crucial to emphasize that the primary objective of this verification process is not to inspect every discrepancy between the models, but rather to affirm the proper implementation of the model, ensuring that any deviations fall within the specified requirements.

Similar to the two-body verification, this verification case is set up using the formation presented in Table 8.1 and Table 8.1. In order to better match and compare the implementation of the model, the

SFF software was tasked to use the following GMAT constants: $\mu, R_e, \omega_e, C_{20}, J_2$. The extracted RSV elements from GMAT, Tudat and the SFF software can be depicted in Figure 8.6.

Analyzing the behavior of the elements in Figure 8.6 reveals several noteworthy observations. Firstly, all results exhibit identical movements and trends. It is essential to highlight that the observed deviation in inclination remains within a narrow range. Specifically, the disparity between GMAT and SFF amounts to a mere 0.015 degrees. To gain a more tangible perspective of this discrepancy, a Cartesian coordinates deviation is calculated using the orbit radius. Using this approach, the calculated Cartesian discrepancy is found to be 1.8 km. While quantifying these deviations is imperative for subsequent control verification, it is crucial to emphasize that this deviation do not stem from errors within the implementation. Conversely, the propagation conducted in Tudat appears to align more closely with the solution derived from the SFF software. Additionally, the introduction of J_2 perturbation is anticipated to introduce a secular drift in the RAAN, a phenomenon evident in Figure 8.6. A more precise quantification can be achieved by examining the differences between the models, as illustrated in Figure 8.7.

The outcome of different software can become clear by looking at Figure 8.7. For all RSV elements, it is observed that the deviation between Tudat and the SFF is significantly smaller than the deviation between GMAT and SFF. The major difference between GMAT, Tudat and the SFF software is the propagation scheme. While GMAT and Tudat propagate Cartesian element, the SFF software uses the presented RSV variables for the integration. Moreover, to convert the Cartesian element to the RSV, coordinate transformations are used. It is expected that GMAT and Tudat use a different set of coordinate transformations. Following the same methodology previously used for the inclination, the maximum Cartesian deviation can be calculated for the RSV state with respect GMAT and Tudat, respectively. For GMAT, the maximum Cartesian deviation is calculated to be 4.8 km and for Tudat this values reduces to 0.19 m. GMAT and Tudat, with the coordinate transformations utilized in the SFF software closely resembling the Tudat implementation. It is noteworthy that the utilization of GMAT constants within the SFF software rules out the possibility of the discrepancies originating from the constants themselves.

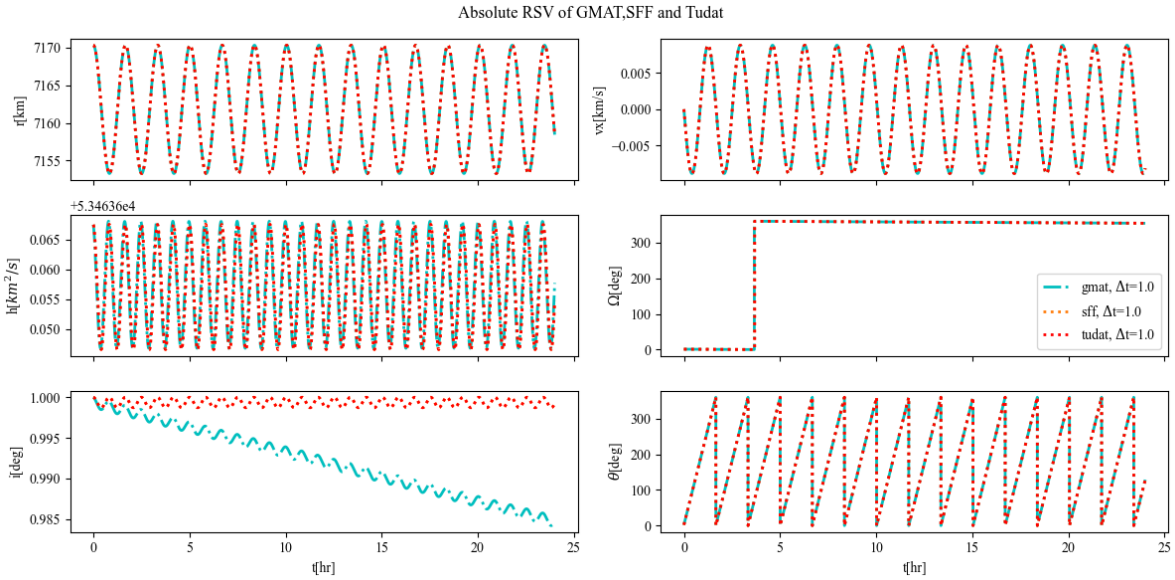

Figure 8.6: Results verification process for the absolute dynamics expressed in RSV, using the results from GMAT, Satellite Formation Flying (SFF) software, and Tudat. All simulations have been performed for a spherical Earth with a fixed 1 second RK4 integrator.

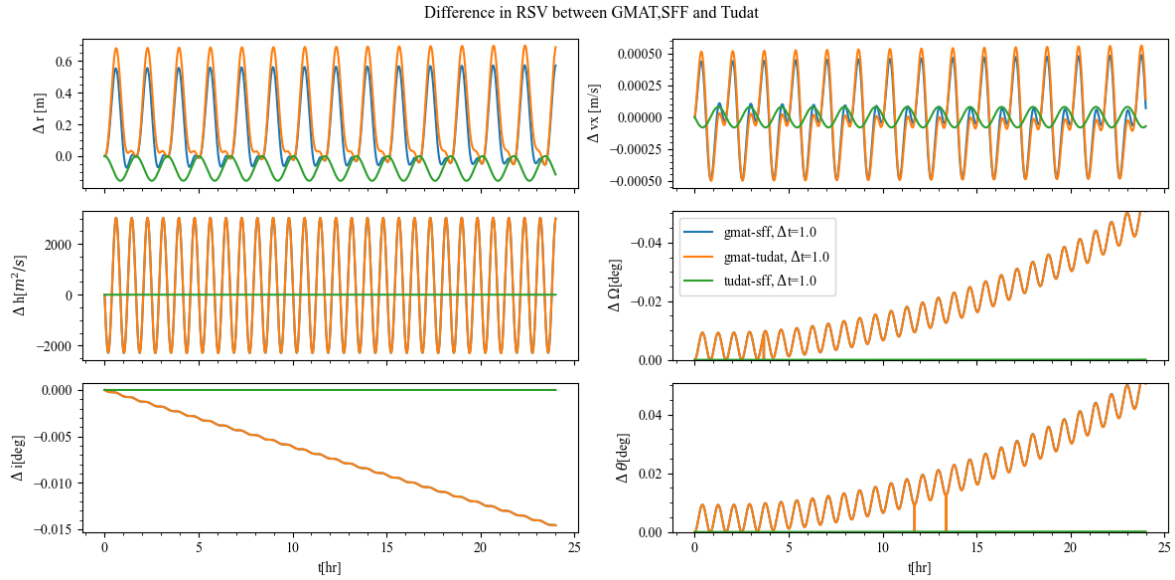

Figure 8.7: Results verification process for the absolute dynamics expressed as the difference between simulation, using the results from GMAT, Satellite Formation Flying (SFF) software, and Tudat. All simulations have been performed for a spherical Earth with a fixed 1 second RK4 integrator.

Moreover, the analysis can be expanded by mapping the relative coordinates between GMAT and the SFF software in the LVLH frame. The results depicted in Figure 8.8 are derived from the identical simulation employed for the absolute dynamics assessment. With the exception of the position and velocity in the z-direction, the data closely aligns with the simulation conducted in GMAT. The observed divergence in the z-direction may potentially be attributed to the exceedingly minute oscillations in the formation (on the order of micrometers), which could potentially magnify rounding errors or coordinate transformations. However, for the purposes of model verification, the scale of this deviation is such that further analysis of this discrepancy is deemed unnecessary.

Next, the differences have been calculated and can be seen in Figure 8.9. What becomes immediately clear from Figure 8.9 is that the along-track (y) position is shown a steady drift. The observed drift is anticipated to stem from the initial conditions set in GMAT. GMAT permits the import of initial states in the form of orbital elements, but it undergoes a conversion process to transform these elements into Cartesian elements as part of its propagation scheme. During this conversion, deviations in the initial state may arise, potentially serving as the source of the observed drift. Nonetheless, it is crucial to note that an overall deviation of 0.03 meters after 24 hours of propagation remains minor when contrasted with the model's accuracy in relation to actual dynamics.

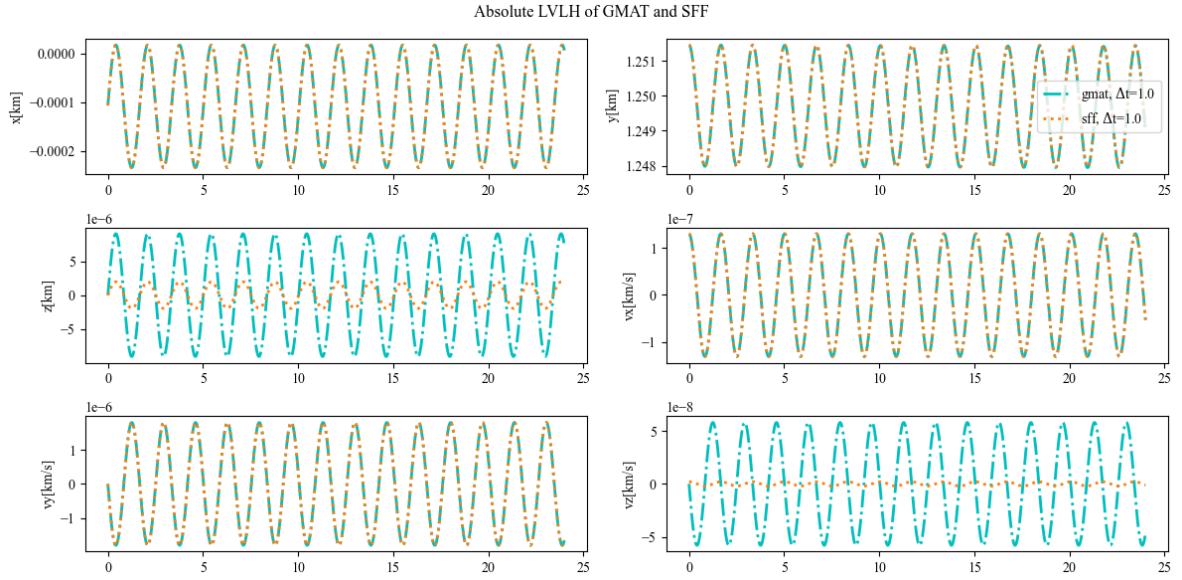

Figure 8.8: Results verification process for the relative dynamics expressed in the LVLH frame, using the results from GMAT and Satellite Formation Flying (SFF) software. All simulations have been performed for a spherical Earth with a fixed 1 second RK4 integrator.

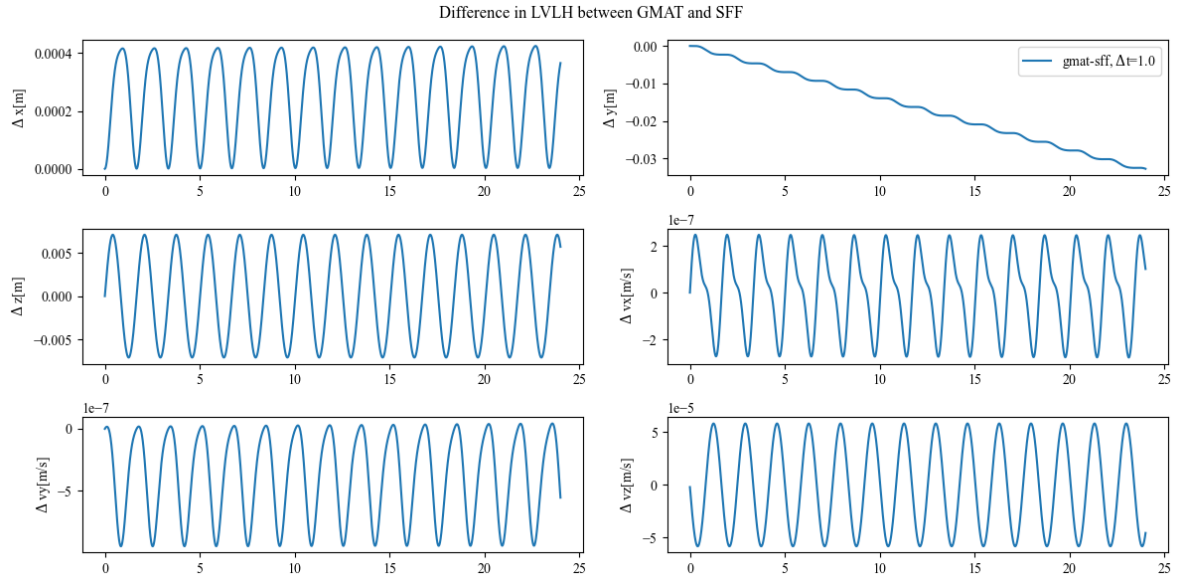

Figure 8.9: Results verification process for the relative dynamics expressed as the difference between simulation, using the results from GMAT and Satellite Formation Flying (SFF) software. All simulations have been performed for a spherical Earth with a fixed 1 second RK4 integrator.

8.3.3. SFF Software with J2 and Drag (MSISE90)

Finally, a test case has been set up to verify the implementation of drag into the SFF software. For this simulation, GMAT is equipped with the MSISE90 atmosphere model and the density provided by GMAT is used as an input for the SFF software. The outcome of this part of the verification can be obtained in Figure 8.10. As expected, a reduction is the along track direction can be observed because the y-axis is most effected by drag acceleration. In general, the both GMAT and SFF show similar results. For better inspection, the difference is calculated and shown in Figure 8.11. Here, a position deviation around 0.15 meter is seen, which denotes the correct implementation of the drag acceleration. Again, the effect of the initial state transformation by GMAT can be observed. The initial velocity in y and z-direction contain an offset with respect to the expected velocity. For the scale of accuracy needed for this simulation, these deviations are accepted.

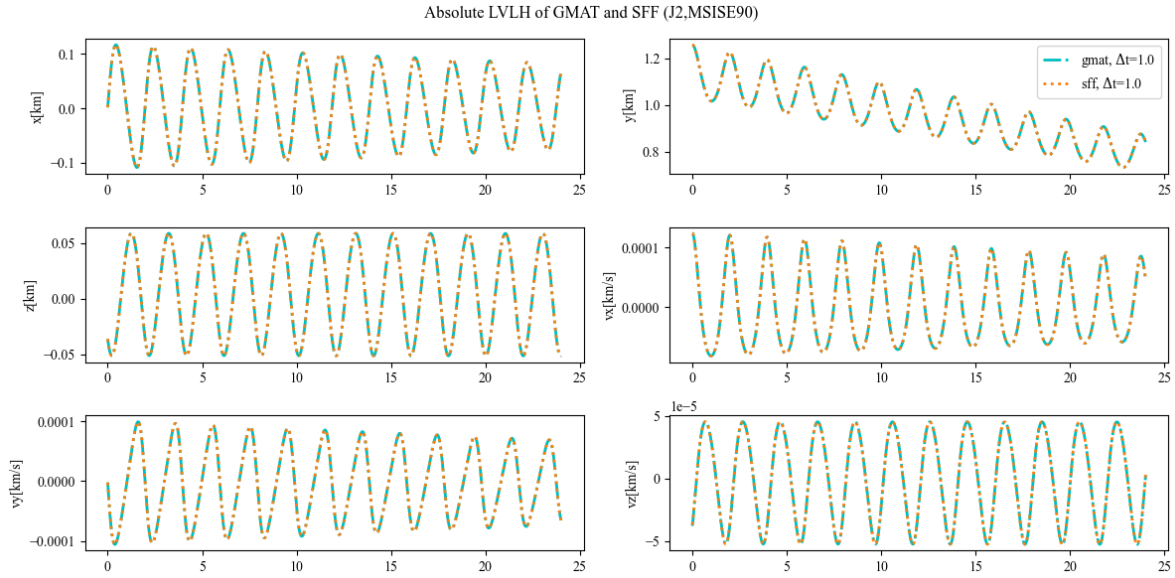

Figure 8.10: Results verification process for the relative dynamics expressed in the LVLH frame, using the results from GMAT and Satellite Formation Flying (SFF) software. All simulations have been performed for a spherical Earth including drag (MSISE90) with a fixed 1 second RK4 integrator.

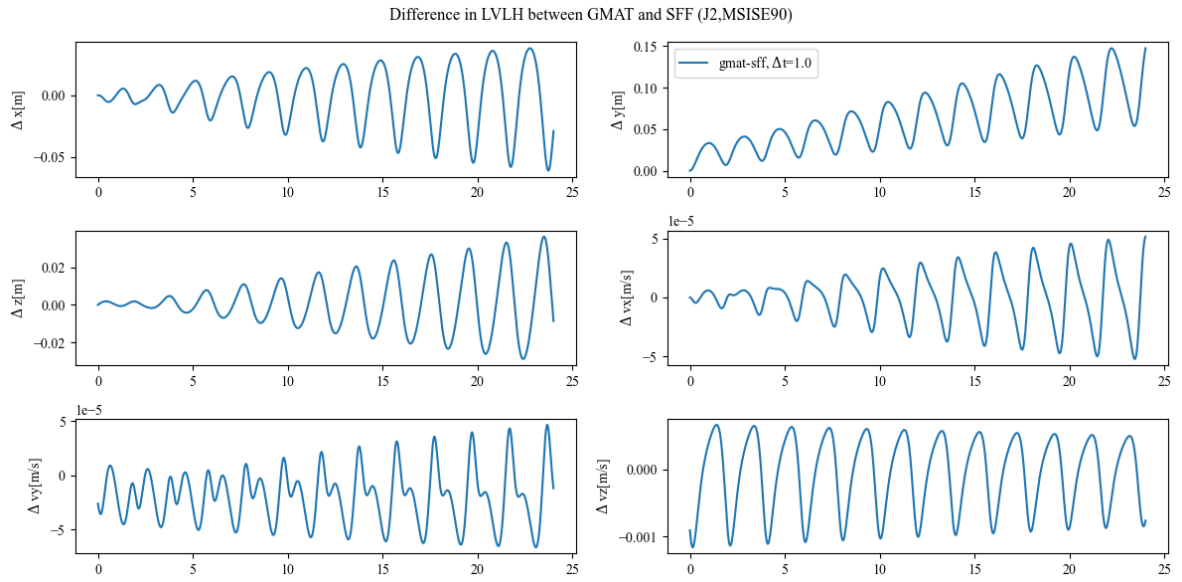

Figure 8.11: Results verification process for the relative dynamics expressed as the difference between simulation, using the results from GMAT and Satellite Formation Flying (SFF) software. All simulations have been performed for a spherical Earth including drag (MSISE90) with a fixed 1 second RK4 integrator.

In conclusion, the objective of this section was to illustrate the verification process for the dynamical model. To ensure accuracy and avoid erroneous statements, additional software called Tudat was employed. By comparing the discrepancies between different software, it was determined that the deviations within the SFF software were of a similar order of magnitude as those between GMAT and Tudat. Ultimately, the implementation of both absolute and relative dynamics was considered successful. For more comprehensive information on the verification process, please refer to Appendix A.

8.4. Formation Stability Analysis

One of the formation being analyzed is the energy-matched formation presented by Xu et al. 2009. The paper demonstrated that guidance formations derived from the standard CW equations lack to account for nonlinearity or J2. Xu et al. 2009 executed a simulation to demonstrate the long term drifts while using a GCO formation for guidance. The goal of their research was to show the effect of using GCO or PCO initial condition for guidance and derive a guidance solution that reduces formation drift.

The simulation performed by Xu et al. 2009 have been used to partially verify the relative dynamics. This section will touch upon the verification overall relative dynamics, by comparing the formation drift observed by Xu et al. 2009. and the SFF software. For this simulation, the satellite parameters used by Xu et al. 2009 have been inserted into the SFF software to closely match the initial conditions. The parameters used for this simulation are:

Parameter	Symbol	Orbit
SMA	a	8000 km
ECC	e	0.1
INC	i	63.43°
RAAN	Ω	0.0°
AOP	ω	45°
TA	ν	0.0°

Table 8.3: The reference case used for verification of the relative dynamics. The parameters have been matched with the simulation performed by Xu et al. 2009

Parameter	Symbol	Formation
x LVLH	x	0.5 km
y LVLH	y	0.0 km
z LVLH	z	1.0 km
$\dot{x}$ LVLH	$\dot{x}$	0.0 km/s
$\dot{y}$ LVLH	$\dot{y}$	-1.03415 km/s
$\dot{z}$ LVLH	$\dot{z}$	0.0 km/s

Table 8.4: The formation used for verification of the relative dynamics. The parameters have been matched with the simulation performed by Xu et al. 2009

The formation described in Table 8.3 is design around a radius of 1 km with $\dot{x}$ and $\dot{y}$ being calculated by using the energy-matching condition described in subsection 3.3.2. The purpose of this section is to verify the implementation of the guidance of the GCO and the GCO with energy matching. Whilst demonstrating the effectiveness of using energy matching, Xu et al. 2009 showed that the drift as a consequence of using the GCO formation resulted to be 2 km in 96 hr as seen in Figure 8.12. The custom implementation of the GCO formation is depicted in Figure 8.13. Notably, the radial and cross-track components exhibit slight variations, whereas the along-track drift aligns with the previously presented 2 km measurement. This simulation demonstrates that the implementation and propagation of the closely resembles the reference case, however, since exact details of the reference spacecraft were not presented, it can not be analyzed further.

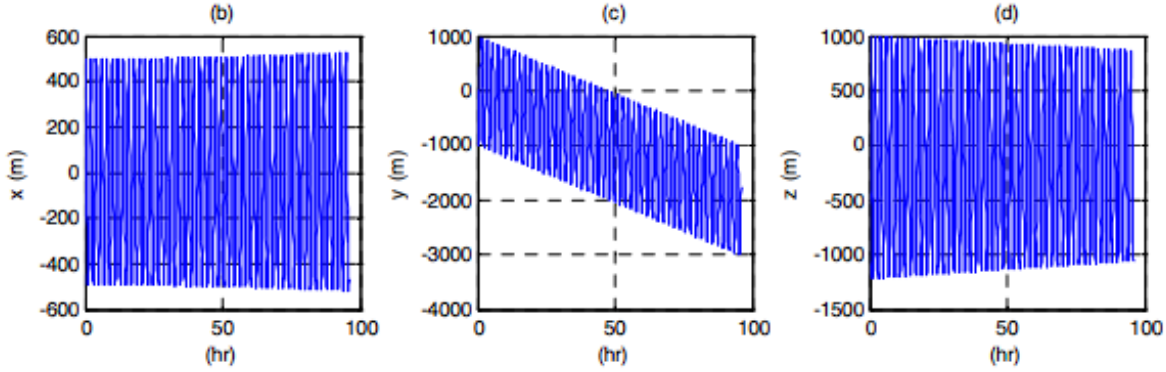

Figure 8.12: Formation as a function of time using linearly derived GCO initial conditions. Note this figure is taken from simulation performed by Xu et al. 2009

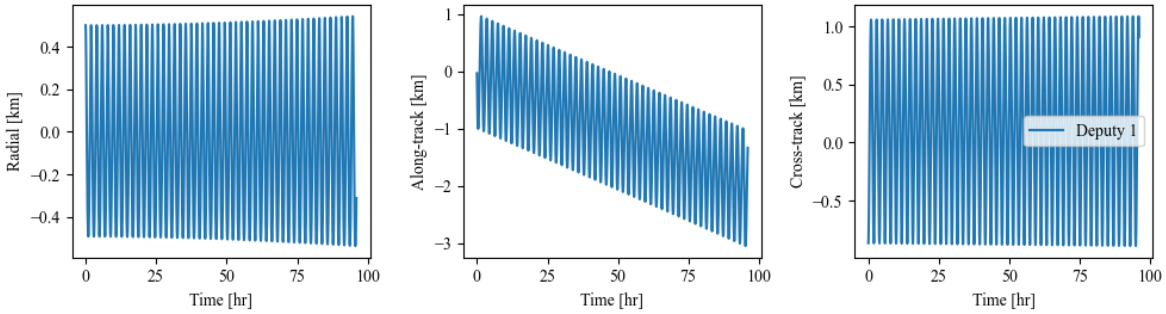

Figure 8.13: Formation as a function of time using linearly derived GCO initial conditions. These results have been acquired from the SFF software.

Another case that has been analyzed in the paper from Xu et al. 2009, is the stability of the energy-matched PCO formation. Energy matching can provide an initial condition that does not show significant drift over a short time (up to 8 days), Xu et al. 2009. For more detail on the guidance implementation, read subsection 3.3.2. Furthermore, the benefits of using an energy matched condition for formation flying is discussed in Chapter 6. So, by looking at the simulation performed by Xu et al. 2009 shown in Figure 8.14, it can be clear that the formation does not suffer from a constant drift in the along-track direction. Again, the simulation settings have been replicated to visualize the stability of the energy-matched GCO. The results of the SFF software can be seen in Figure 8.15. For all axis, it can be concluded that the energy-matched GCO is stable for the 96hr time frame and that the outcome of the SFF software closely resembles the simulation performed by Xu et al. 2009. While the figures provided may not achieve meter-level accuracy, it does serve as evidence to support the conclusion that the guidance algorithm implementation yields a stable formation propagation.

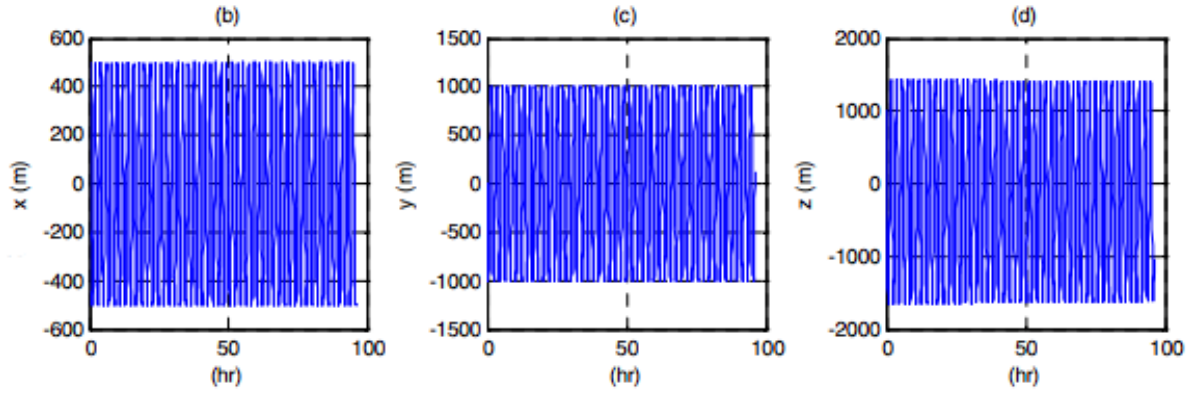

Figure 8.14: Formation as a function of time using energy-matched GCO initial conditions. Note, this figure is taken from simulation performed by Xu et al. 2009

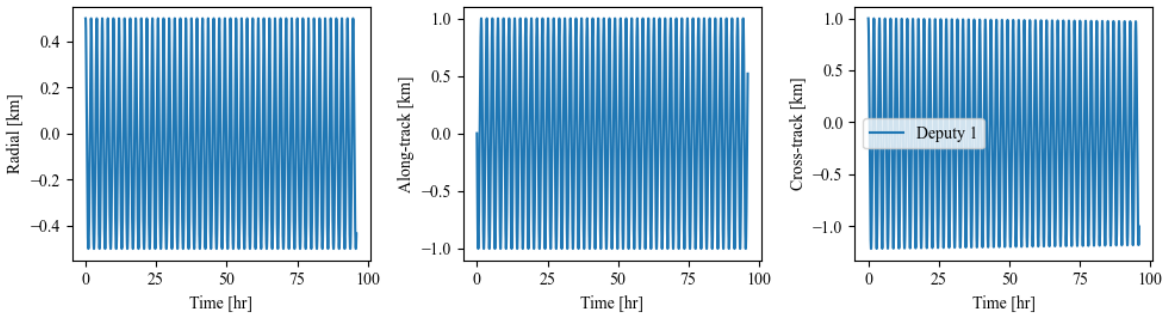

Figure 8.15: Formation as a function of time using energy-matched GCO initial conditions. These results have been acquired from the SFF software.

8.5. Controller Verification

The objective of this section is to conduct a preliminary assessment of the controller based on the findings presented in the research conducted by Liu and Hexi 2006. While specific details about the satellites are not provided, valuable insights into the characteristics of the SMC implementation can be gathered by examining the results produced by the SFF software in comparison to the figures presented by Liu and Hexi 2006. The reference orbit and initial conditions of the formation have been matched and are presented below:

Parameter	Symbol	Orbit
SMA	a	7171 km
ECC	e	0.0001
INC	i	0°
RAAN	Ω	0°
AOP	ω	0°
TA	ν	0°

Table 8.5: The reference case used for verification of the relative dynamics. The parameters have been matched with the simulation performed by Xu et al. 2009

Parameter	Value	Parameter	Value
r_0	1.49 km	r_d	1.0 km
x_0	0.745 km	x_d	0.5 km
y_0	0.0 km	x_d	0.0 km
z_0	-1.2904 km	x_d	-0.86603 km
$\dot{x_0}$	0.0 km/s	x_d	0.0 km/s
$\dot{y_0}$	-0.0015 km/s	y_d	-0.0010 km/s
$\dot{z_0}$	0.0 km/s	z_d	0.0 km/s

Table 8.6: The formation used for verification of the relative dynamics. The parameters have been matched with the simulation performed by Xu et al. 2009

The initial and desired condition, presented in Table 8.6, have been calculated using the GCO guidance methodology presented in Chapter 3. The controller is tasked to reduce the formation size from a radius of 1.49 km to 1 km by applying thrust is all axis. Before, the results of the SFF software are presented,

it is import to note that the dynamics model used in the reference case does not represent the model used in the SFF software. To be specific, the model used in the reference case simulated the external disturbance by a sin function with a certain noise added, whereas the SFF software included the effect of J_2 and drag. Having said that, the results are expected to be different, however, the differences in force model are not expected to result in the SMC to be instable. Therefore, this verification step is taken and used to get insight in the performance and stability of the SMC to an extended force model. Another deviation between the two simulation lays in the implementation of the dynamics, Both simulations use different equation of motion to describe the nonlinear relative dynamics. And here again, although different in fuel consumption and controller accuracy are expected, the effect over 1 orbit propagation should be minimal.

Liu and Hexi 2006 presented results indicating that a reconfirmation maneuver has the capability to achieve convergence after 70 percent of the orbital period. The resulting trajectory is illustrated in Figure 8.16. Furthermore, their simulation demonstrated a substantial reduction in tracking error, decreasing it from 500 meters to less than 15 meters after one orbit. The time-dependent tracking error is depicted in Figure 8.17. When comparing the reference case to the results obtained from the SFF software, several notable observations can be drawn. The deputy trajectory and tracking error from the SFF software can be seen in Figure 8.18 and Figure 8.19. overall, the chosen guidance trajectory is similar across the models, and not abnormality is observed. With respect to the tracking error, it seems like the slower with its converge to zero. In the end, these figures are useful to get an impression of the SMC for a different dynamical system, but note that this is purely based on overall pattern recognition. To get in more detail, the delta-V expenditure after one orbit for the reference case is given to be 2.39 m/s, while achieving a tracking error of 12.0 meter, Liu and Hexi 2006. This closely resembles the controller output of the SFF software, with only 1.85 m/s and 1.31 m error. So, the controller is able to converge for the reference case with a similar satellite and different dynamics model. It is too early to conclude that the new implementation results in a more fuel-optimum solution, because a lot is still unknown of the reference case's simulation settings and satellite properties. However, it can be concluded that the implementation has shown stable result for an unbounded thruster in a perturbed environment.

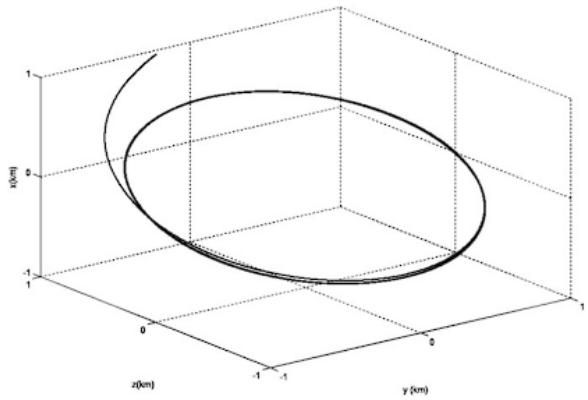

Figure 8.16: 3D trajectory of large reconfiguration maneuver taken from the research performed by Liu and Hexi 2006.

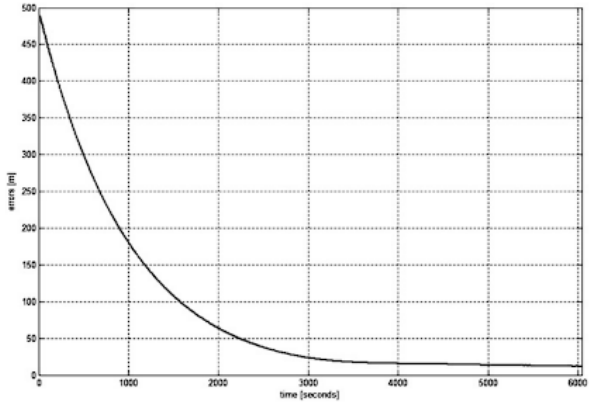

Figure 8.17: tracking error of large reconfiguration maneuver taken from the research performed by Liu and Hexi 2006.

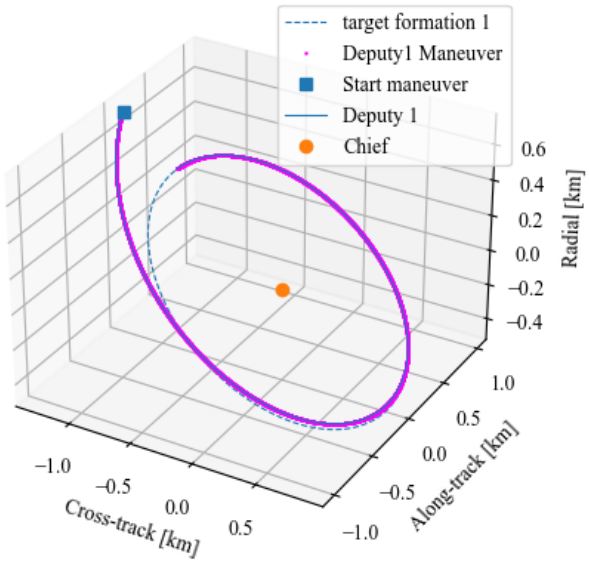

Figure 8.18: 3D trajectory of large reconfiguration maneuver obtained by using the SFF software.

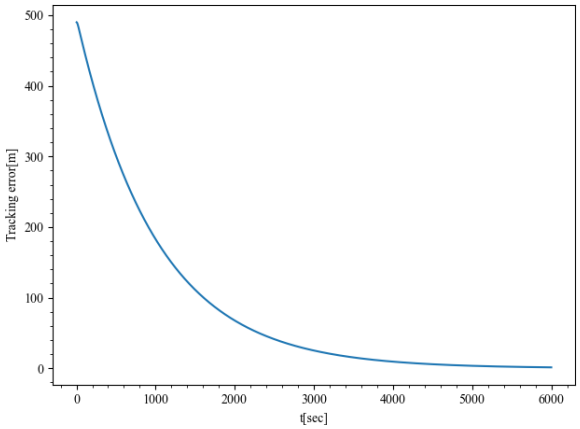

Figure 8.19: tracking error of large reconfiguration maneuver obtained by using the SFF software.

9

Conclusion

In this thesis, we embarked on a journey to explore the intricate world of satellite formation flying and develop a comprehensive end-to-end Guidance, Navigation and Control (GNC) solution. Through a systematic and rigorous approach, we have addressed key research questions and made significant contributions to the field of formation flying.

Firstly, we delved into the fundamental concepts of satellite formation flying, elucidating the various formation types and their applicability to a real-world mission. This foundational knowledge laid the groundwork for our subsequent endeavors. We developed a robust navigation system, utilizing Extended Kalman Filter (EKF) techniques to process real GPS data. This system allowed us to accurately estimate the initial state of our satellite formation, a critical component for precise control. Our investigations into the modification of the Sliding Mode Controller (SMC) to accommodate realistic low-thrust engines and nonlinear dynamics expanded the applicability of this control method. We demonstrated its effectiveness in maintaining formation integrity, even in the presence of major disturbances like Earth's oblateness and atmospheric drag. Furthermore, we explored various multi-satellite guidance strategies, highlighting the software's adaptability for diverse formation types. The consequences of different guidance approaches on fuel consumption were meticulously analyzed, providing valuable insights for mission planning.

The research questions have been thoroughly addressed and answered in a dedicated chapter of the report. Here, concise answers with corresponding references are provided.

Problem A: *Which methodology and software are required to enable the development of a complete GNC system suitable for satellite formation flying?* Developing the guidance and control system as a separate task is essential to avoid making misleading and overly optimistic decisions about the accuracy of input data. Furthermore, establishing a clear operational workflow to obtain an accurate navigation solution is crucial for achieving a realistic guidance and control system. Due to the lack of an accurate navigation system for the current missions, the navigation system was developed. This required solution was obtained using a combination of Python and the GMAT. For a comprehensive assessment of the algorithm's performance, please refer to Chapter 4. The system's verification was conducted using a large set of GPS measurements, and the detailed analysis can be found in section 8.1.

Problem B: *How can the optimal control problem be formulated and solved for formation flying of a reduced formation consisting of a chief and one deputy whilst including the major disturbances such as Earth's oblateness, drag effect and non-linearity?* The dynamics for both the chief and deputy were based on the model presented by Morgan and Chung 2012. This model extended the work of Xu and Wang 2008 by incorporating the effects of drag. It was noted that the update by Morgan and Chung 2012 contained a typo, which is discussed in detail in Equation 3.4.2. The deputy's guidance was determined using the CW equations within a GCO formation. To solve the optimal control problem, a SMC was employed. Notably, the implementation of a real thruster revealed challenges related to convergence, which are extensively discussed in section 5.1 and section 5.2. In summary, the

simulations demonstrated that frequent maneuvers (every few hours) were necessary, with significant drift primarily attributed to the linearized guidance solution.

Problem C: *What is the impact on fuel cost by defining a target formation based on the orbital momentum and energy-matched conditions, instead of using well-known CW condition?* In a study by Xu et al. 2009, it was demonstrated that employing energy matching could greatly enhance formation stability and reduce fuel consumption. The investigation into different formations utilizing the energy matching method is presented in Chapter 6. The findings revealed that in a nonlinear environment, there was no observable drift in the guidance solution. Consequently, the number of maneuvers required over a 7-day period was reduced from 36 to just 7. For a comprehensive understanding of the simulation setup and outcomes, please refer to Chapter 6. Ultimately, both the energy-matched GCO and ATO formations consume significantly less fuel than the CW-guided formation. For more details on fuel expenditure, please refer to section 6.3 in the document.

Problem D: *How can the optimal control problem be extended to include up to four satellites, and which adaptations are necessary to guarantee safe operations?* The final step was to extend the software to four satellite. The current implementation of the SFF software allowed for a straight forward extension of the number of satellites. Following the same algorithm and control law, no difficulties were encountered. Nevertheless, the control and operation of four satellite did require several save zones, to ensure safe operations. The simulation for a GCO formation revealed that fuel usage among satellites significantly depends on the controller's ability to achieve convergence to the final state. Furthermore, safe operations were maintained through the 400-meter constraint, which kept the satellites within proximity of their intended formation. From the results of the ATO formation, it was seen that the capability of the SMC influenced the drift rate of the satellite more than the formation size. Overall, the software was able to control three deputies whilst meeting the constraints.

In practical terms, our software framework was rigorously tested and verified through extensive simulations, whose results can be obtained in Chapter 8. We successfully handled formations ranging from two to four satellites, showcasing the versatility and reliability of our end-to-end GNC system.

As we reflect on our journey, it becomes evident that the pursuit of excellence in satellite formation flying demands a multidisciplinary approach. Our work bridges the gap between theoretical research and real-world mission execution, offering a practical tool set for future endeavors in this domain.

While this thesis marks the culmination of our current efforts, it also opens the door to further exploration. The challenges of satellite formation flying are dynamic, and new missions will continually demand innovative solutions. As such, this work is not an endpoint, but a stepping stone for future research and development in the exciting realm of satellite formation flying.

In conclusion, we have strived to provide a holistic understanding of the processes, methodologies, and tools required to achieve successful satellite formation flying missions. Our journey has been one of learning, discovery, and innovation, and we hope that the knowledge and insights gained will inspire and empower future generations of researchers and engineers in this captivating field.

9.1. Contributions

The research discussed in this thesis contains four main contributions.

- Processing of actual satellite data for the development and verification of the navigation system.
- Development of a navigation Solution utilizing an EKF with authentic GPS data.
- Modification of the SMC incorporating a realistic low-thrust engine.
- Modification of the SMC incorporating a nonlinear dynamics model accounting for J_2 and drag.
- Implementation of diverse multi-satellite guidance strategies to demonstrate software adaptability for various formations.

9.2. Future Work

- **Advanced Navigation System Exploration:** The comprehensive mission scenario encompasses four satellites, necessitating the generation of a navigation solution. Throughout this thesis, we have discussed the suitability of both Batch Least Squares (BLS) and Uncended Kalman Filter (UKF) as viable options for this task. Looking ahead, future satellites may possess inter-satellite communication capabilities, enabling direct data exchange between satellites. Consequently, an exciting avenue for future research lies in the development of multi-satellite navigation systems.
- **Enhancing GNC System Validation:** In the verification section, we successfully highlighted variations between models within different software platforms. To deepen our understanding, it is imperative to quantify the impact of these model inaccuracies in relation to real-world scenarios. This involves a meticulous analysis of errors inherent in the dynamical model, ultimately shedding light on the attainable control accuracy. Such insights are of paramount importance, as they enhance our grasp of the system's precision in addressing real-world challenges.
- **Enhancing Efficiency through Burn/Coast/Burn Optimization:** Currently, the control methodology relies on activation and deactivation conditions, circumventing the need for extensive optimization. However, it is essential to note that this approach, due to the inherent coupling of radial and along-track motion, might not yield the most fuel-efficient maneuvers. In pursuit of minimizing fuel consumption, an optimization problem has been devised, employing a burn/coast/burn strategy. The advantages of this strategy have been aptly demonstrated by Wang et al. 2017 and can be viewed as a prospective advancement in the evolution of the SFF software.
- **Differential drag control for along-track drift compensation** From the results presented in the thesis, it is clear the majority of the formation maintenance maneuvers are initiated by exceeding the along-track constraint. The along-track drift is around 2 orders of magnitude higher than the cross-track drift. In an attempt to reduce fuel operations, differential drag can be implemented. By altering the satellite orientation, a drift can be initiated or cancelled. To correct out-of-plane drift, the current implementation of the SFF software would be used.
- **Mitigating Along-Track Drift with Differential Drag Control:** The thesis findings highlight that a significant portion of formation maintenance maneuvers are prompted by surpassing along-track constraints, with along-track drift being approximately two orders of magnitude greater than cross-track drift. To optimize fuel consumption, the application of differential drag control emerges as a potential solution. This entails adjusting satellite orientation to either induce or counteract drift. Out-of-plane drift would still be corrected by the existing SFF software implementation.
- **Addition of attitude to drag calculation** The current drag model employs a fixed drag area, which is unrealistic when dealing with maneuvering satellites using a single thruster as the satellite needs to slew and alter its attitude during maneuvers. However, since the required slew is known, implementing dynamic drag area adjustment should not be excessively complex.

Bibliography

Alfriend, K. et al. (2010). *Spacecraft Formation Flying: Dynamics, control and navigation*. Elsevier Astrodynamics Series.

Biswas, S. and A. Dempster (2023). *Navigation and Tracking in Space: Analysis and Algorithms*.

Chao, C. and H. Bernstein (1994). *Onboard station keeping of geosynchronous satellites using a global positioning system receiver*. Journal Guidance Control & Dynamics Vol.17 , pp. 778-786.

Clohessy, W. H. and R. S. Wiltshire (1960). *Terminal Guidance System for Satellite Rendezvous*. Journal of the Aerospace Sciences, Vol. 27, No. 9. pp. 653-658.

Degnan, J. (2019). *An Introduction to Satellite Laser Ranging Technology and its Applications: Part 1: Technology*. SLR School.

Huang, H. and Y. Zhuang (2015). *Optimal Satellite Formation Reconfiguration Using Co-Evolutionary Particle Swarm Optimization in Deep Space*. Acta Astronautica, Vol. 113 , pp. 149-162.

Huang, H. et al. (2012). *Optimal Spacecraft Formation Re-configuration with Collision Avoidance Using Particle Swarm Optimization pp. 143-150.* Information Technology And Control, Vol. 41, No.2, pp. 143-150.

Huntington, G. and A. Rao (2005). *Optimal configuration of spacecraft formations via a Gauss pseudospectral method*. Adv Astronaut Sci Vol. 120, pp. 33–50.

Jin, X. and H. Lifu (2011). *Formation keeping of micro-satellites LQR control algorithms analysis*. Proceedings of 2011 International Coneference on Electronics.

Kechichian, J. (1998). *Motion in general elliptic orbit with respect to a dragging and precessing coordinate frame*. The Journal of the Astronautical Sciences, vol. 46, No. 1.

Koenig, W., T. Fugganti, and S. D'Amico (2017). *New state transition matrices for spacecraft relative motion in perturbed orbits*. Journal of Guidance, Control, and Dynamics, Vol. 40, No. 7. pp. 1749-1786.

Liu, H. and B. Hexi (2006). *Sliding mode control for low-thrust Earth-orbiting spacecraft formation maneuvering*. Aerospace Science and Technology, Vol.10.

M. Pontani, B. A. Conway (2010). *Particle Swarm Optimization Applied to Space Trajectories*. Journal of Guidance, Control, and Dynamics, Vol. 33, No. 5. pp. 1429-1441.

Morgan, D. and S. Chung (2012). "Swarm-Keeping Strategies for Spacecraft under J2 and Atmospheric Drag Perturbations". In: *American Institute of Aeronautics and Astronautics*.

Park, J. et al. (2008). *Comparison between the KOMPSAT-1 drag derived density and the MSISE model density during strong solar and/or geomagnetic activities*. Earth Planets Space, Vol.60, pp. 601–606.

Picone, J. M., A. E. Hedin, and D. P. Drob (2002). *NRLMSISE-00 empirical model of the atmosphere:Statistical comparisons and scientific issues*. Journal of Geophysical Research, Vol. 107, No. A12.

Reid, T., T Walter, and P. Enge (2013). *L1/L5 SBAS MOPS Ephemeris Message toSupport Multiple Orbit Classes*. International Technical Meeting of The Institute of Navigation.

Richards, A. et al. (2002). *Spacecraft trajectory planning with avoidance constraints using mixed-integer linear programming.* J Guid Control Dyn Vol. 25, No. 4, pp. 755–764.

Sabol, C., R. Burns, and CA McLaughlin (2001). *Satellite formation flying design and evolution*. J Spacecraft Rock, Vol 38, No 2, pp. 270–278.

Starin, S., R. Yedavalli, and A. Sparks (2001a). *Spacecraft formation flying maneuvers using linear-quadratic regulation with no radial axis inputs*. AIAA Guidance Navigation & Control Conference pp. 2001-6504.

Starin, S., R. Yedavilli, and A. Sparks (2001b). *Design of a LQR controller of reduced inputs for multiple spacecraft formation flying*. American Contr. Conf.

The GMAT Development Team (2022). *General Mission Analysis Tool (GMAT) User Guide*. National Aeronautics and Space Administration.

Vallado, D. A. (2010). *Fundamentals of Astrodynamics and Applications: Tutorial Lectures*. 4th ICATT, Madrid, Spain.

— (2013). *Fundamentals of Astrodynamics and Applications*. Microcosm Press.

Wang, D., B. Wu, and E. K. Poh (2017). *Satellite Formation Flying: Relative Dynamics, Formation Design Fuel Optimal Maneuvers and Formation Maintenance*. Intelligent Systems, Control and Automation: Science and Engineering.

Wu, B., G. Xu, and X. Cao (2016). *Relative dynamics and control for satellite formation: accommodating J2 perturbation*. Journal of Aerospace Engineering, Vol. 29, No. 4.

Xu, G. and D. Wang (2008). *Nonlinear Dynamic Equations of Satellite Relative Motion Around an Oblate Earth*.

Xu, G. et al. (2009). *Periodic and Quasi-Periodic Satellite Relative Orbits at Critical Inclination*. IEEE Aerospace conference,pp. 1–11.

Yeh, H, E. Nelson, and A. Sparks (2002). *Nonlinear tracking control for satellite formations*. Journal of Guidance, Control, and Dynamics, Vol. 25, No. 2, pp. 376-386.

A

Verification Data Absolute and Relative Dynamics

A.1. Deviation of Initial States

RSV	SFF vs GMAT	SFF vs Tudat	GMAT vs Tudat
$r[km]$	0.00000000e+00	3.63797881e-12	3.63797881e-12
$v_x[km/s]$	1.24242793e-17	-5.54569411e-17	-6.78812204e-17
$h[km^2/s]$	0.00000000e+00	2.91038305e-11	2.91038305e-11
$\Omega[deg]$	3.64486219e-13	-3.64571080e-13	0.00000000e+00
$i[deg]$	0.00000000e+00	-3.64372296e-13	-3.64486219e-13
$\theta[deg]$	3.65041330e-13	3.64173511e-13	7.29416527e-13

Table A.1: The RSV deviations at the initial epoch with respect to GMAT and Tudat.

LVLH	SFF vs GMAT
$x[km]$	-2.66984785e-18
$y[km]$]	-2.22044605e-16
$z[km]$	3.46944695e-18
$\dot{x}[km/s]$	-2.64697796e-23
$\dot{y}[km/s]$	5.05030160e-19
$\dot{z}[km/s]$	2.77516051e-17

Table A.2: The LVLH deviations at the initial epoch with respect to GMAT and Tudat.

A.2. Maximum Model Deviation under the Influence of PM, J2 and J2+MSISE90

RSV	SFF vs GMAT	SFF vs Tudat	GMAT vs Tudat
$r[km]$	0.00000000e+00	3.46517481e-10	4.83851181e-10
$v_x[km/s]$	1.24242793e-17	7.34844256e-12	6.99059636e-10
$h[km^2/s]$	0.00000000e+00	2.40106601e-10	6.33008312e-10
$\Omega[deg]$	3.64486219e-13	-3.64571080e-13	-3.64486219e-13
$i[deg]$	0.00000000e+00	0.06571080e-13	7.29194483e-13
$\theta[deg]$	3.65041330e-13	2.87247576e-11	1.39922222e-12

Table A.3: The maximum RSV deviations with respect to GMAT and Tudat. This simulation has been conducted using only the point mass acceleration of the Earth.

RSV	SFF vs GMAT	SFF vs Tudat	GMAT vs Tudat
$r[km]$	5.72296433e-04	1.55240636e-04	6.96449385e-04
$v_x[km/s]$	1.05831087e-05	-8.70969147e-06	-1.74487122e-05
$h[km^2/s]$	3.03074795e-03	4.72595275e-07	3.03082994e-03
$\Omega[deg]$	-5.08129611e-02	5.94855316e-05	-5.07534807e-02
$i[deg]$	0.00000000e+00	8.79545309e-07	-0.08486219e-13
$\theta[deg]$	3.95720718e-04	-7.57559927e-05	3.94393578e-04

Table A.4: The maximum RSV deviations with respect to GMAT and Tudat. This simulation has been conducted using an oblate Earth.

RSV	SFF vs GMAT
$r[km]$	5.51590777e-01
$v_x[km/s]$	4.41640825e-04
$h[km^2/s]$	2.49803629e-01
$\Omega[deg]$	-4.07108029e-05
$i[deg]$	1.42108547e-14
$\theta[deg]$	-0.03552321e+00

Table A.5: The maximum RSV deviations with respect to GMAT and Tudat. This simulation has been conducted using an oblate Earth and MSISE90 atmosphere model.

LVLH	SFF vs GMAT (PM)	SFF vs GMAT (J2)	SFF vs GMAT (J2+MSISE90)
$x[km]$	9.54694670e-10	4.25028540e-07	3.83858254e-05
$y[km]$	2.23115371e-09	7.98326294e-09	1.47559345e-04
$z[km]$	5.14941619e-12	7.10532423e-06	3.63210460e-05
$\dot{x}[km/s]$	-5.42574568e-13	1.02385530e-10	5.15647821e-08
$\dot{y}[km/s]$	-3.73009523e-13	-5.48011122e-10	-1.15609616e-08
$\dot{z}[km/s]$	-3.12504540e-15	-4.55153735e-08	-7.64795006e-07

Table A.6: The maximum LVLH deviations with respect to GMAT. This simulation has been conducted using different dynamical models.